



## Aerosol remote sensing in polar regions



Claudio Tomasi <sup>a,\*</sup>, Alexander A. Kokhanovsky <sup>b,c</sup>, Angelo Lupi <sup>a</sup>, Christoph Ritter <sup>d</sup>, Alexander Smirnov <sup>e,f</sup>, Norman T. O'Neill <sup>g</sup>, Robert S. Stone <sup>h,i</sup>, Brent N. Holben <sup>f</sup>, Stephan Nyeki <sup>j</sup>, Christoph Wehrli <sup>j</sup>, Andreas Stohl <sup>k</sup>, Mauro Mazzola <sup>a</sup>, Christian Lanconelli <sup>a</sup>, Vito Vitale <sup>a</sup>, Kerstin Stebel <sup>k</sup>, Veijo Aaltonen <sup>l</sup>, Gerrit de Leeuw <sup>l,m</sup>, Edith Rodriguez <sup>l</sup>, Andreas B. Herber <sup>n</sup>, Vladimir F. Radionov <sup>o</sup>, Tymon Zielinski <sup>p</sup>, Tomasz Petelski <sup>p</sup>, Sergey M. Sakerin <sup>q</sup>, Dmitry M. Kabanov <sup>q</sup>, Yong Xue <sup>r,s</sup>, Linlu Mei <sup>s</sup>, Larysa Istomina <sup>b</sup>, Richard Wagener <sup>t</sup>, Bruce McArthur <sup>u,1</sup>, Piotr S. Sobolewski <sup>v</sup>, Rigel Kivi <sup>w</sup>, Yann Courcoux <sup>x</sup>, Pierre Larouche <sup>y</sup>, Stephen Broccardo <sup>z</sup>, Stuart J. Piketh <sup>aa</sup>

<sup>a</sup> Climate Change Division, Institute of Atmospheric Sciences and Climate (ISAC), Italian National Research Council (CNR), Bologna, Italy

<sup>b</sup> Institute of Environmental Physics (IUP), University of Bremen, Bremen, Germany

<sup>c</sup> EUMETSAT, Eumetsat Allee 1, D-64295 Darmstadt, Germany

<sup>d</sup> Climate System Division, Alfred Wegener Institute for Polar and Marine Research, Potsdam, Germany

<sup>e</sup> Sigma Space Corporation, Lanham, MD, USA

<sup>f</sup> Biospheric Sciences Branch, NASA/Goddard Space Flight Center (GSFC), Greenbelt, MD, USA

<sup>g</sup> Canadian Network for the Detection of Atmospheric Change (CANDAC) and CARTEL, Dept. of Applied Geomatics, University of Sherbrooke, Sherbrooke, Québec, Canada

<sup>h</sup> Global Monitoring Division (GMD), National Oceanic and Atmospheric Administration (NOAA), Boulder, CO, USA

<sup>i</sup> Cooperative Institute for Research in Environmental Sciences (CIRES), University of Colorado, Boulder, CO, USA

<sup>j</sup> Physikalisch-Meteorologisches Observatorium (PMOD)/World Radiation Centre (WRC), Davos, Switzerland

<sup>k</sup> Norwegian Institute for Air Research (NILU), Kjeller, Norway

<sup>l</sup> Climate and Global Change Division, Finnish Meteorological Institute (FMI), Helsinki, Finland

<sup>m</sup> Department of Physics, University of Helsinki, Finland

<sup>n</sup> Climate System Division, Alfred Wegener Institute for Polar and Marine Research, Bremerhaven, Germany

<sup>o</sup> Arctic and Antarctic Research Institute (AARI), St. Petersburg, Russia

<sup>p</sup> Institute of Oceanology (IO), Polish Academy of Sciences (PAS), Sopot, Poland

<sup>q</sup> V. E. Zuev Institute of Atmospheric Optics (IAO), Siberian Branch (SB), Russian Academy of Sciences (RAS), Tomsk, Russia

<sup>r</sup> Faculty of Life Sciences and Computing, London Metropolitan University, London, United Kingdom

<sup>s</sup> Key Laboratory of Digital Earth Science, Institute of Remote Sensing and Digital Earth, Chinese Academy of Sciences, Beijing 100094, China

<sup>t</sup> Brookhaven National Laboratory, Environmental and Climate Sciences Dept Upton, NY, USA

<sup>u</sup> Environment Canada, Downsview, North York, Ontario, Canada

<sup>v</sup> Institute of Geophysics, Polish Academy of Sciences (PAS), Warsaw, Poland

<sup>w</sup> Arctic Research Center, Finnish Meteorological Institute (FMI), Sodankylä, Finland

<sup>x</sup> Institut de l'Atmosphère de la Réunion (OPAR), Univ. de la Réunion, CNRS, Saint Denis de la Réunion, France

<sup>y</sup> Institut Maurice-Lamontagne, Mont-Joli, Quebec, Canada

<sup>z</sup> Geography, Archeology and Environmental Science, University of the Witwatersrand, Johannesburg, South Africa

<sup>aa</sup> Climatology Research Group, Unit for Environmental Sciences and Management, North-West University, Potchefstroom, South Africa

### ARTICLE INFO

#### Article history:

Received 15 April 2014

Accepted 1 November 2014

Available online 10 November 2014

#### Keywords:

Sun-photometer measurements

Aerosol optical thickness

Polar aerosol optical characteristics

Lidar backscattering coefficient profiles

Satellite aerosol remote sensing

Multimodal aerosol extinction models

### ABSTRACT

Multi-year sets of ground-based sun-photometer measurements conducted at 12 Arctic sites and 9 Antarctic sites were examined to determine daily mean values of aerosol optical thickness  $\tau(\lambda)$  at visible and near-infrared wavelengths, from which best-fit values of Ångström's exponent  $\alpha$  were calculated. Analysing these data, the monthly mean values of  $\tau(0.50 \mu\text{m})$  and  $\alpha$  and the relative frequency histograms of the daily mean values of both parameters were determined for winter–spring and summer–autumn in the Arctic and for austral summer in Antarctica. The Arctic and Antarctic covariance plots of the seasonal median values of  $\alpha$  versus  $\tau(0.50 \mu\text{m})$  showed: (i) a considerable increase in  $\tau(0.50 \mu\text{m})$  for the Arctic aerosol from summer to winter–spring, without marked changes in  $\alpha$ ; and (ii) a marked increase in  $\tau(0.50 \mu\text{m})$  passing from the Antarctic Plateau to coastal sites, whereas  $\alpha$  decreased considerably due to the larger fraction of sea-salt aerosol. Good agreement was found when comparing ground-based sun-photometer measurements of  $\tau(\lambda)$  and  $\alpha$  at Arctic and Antarctic coastal sites with Microtops measurements conducted during numerous AERONET/MAN cruises from 2006 to 2013 in three Arctic

\* Corresponding author. Tel.: +39 051 639 9594; fax: +39 051 639 9652.

E-mail address: [c.tomasi@isac.cnr.it](mailto:c.tomasi@isac.cnr.it) (C. Tomasi).

<sup>1</sup> Now with Agriculture and Agri-food Canada.

Ocean sectors and in coastal and off-shore regions of the Southern Atlantic, Pacific, and Indian Oceans, and the Antarctic Peninsula.

Lidar measurements were also examined to characterise vertical profiles of the aerosol backscattering coefficient measured throughout the year at Ny-Ålesund. Satellite-based MODIS, MISR, and AATSR retrievals of  $\tau(\lambda)$  over large parts of the oceanic polar regions during spring and summer were in close agreement with ship-borne and coastal ground-based sun-photometer measurements. An overview of the chemical composition of mode particles is also presented, based on in-situ measurements at Arctic and Antarctic sites. Fourteen log-normal aerosol number size-distributions were defined to represent the average features of nuclei, accumulation and coarse mode particles for Arctic haze, summer background aerosol, Asian dust and boreal forest fire smoke, and for various background austral summer aerosol types at coastal and high-altitude Antarctic sites. The main columnar aerosol optical characteristics were determined for all 14 particle modes, based on in-situ measurements of the scattering and absorption coefficients. Diurnally averaged direct aerosol-induced radiative forcing and efficiency were calculated for a set of multimodal aerosol extinction models, using various Bidirectional Reflectance Distribution Function models over vegetation-covered, oceanic and snow-covered surfaces. These gave a reliable measure of the pronounced effects of aerosols on the radiation balance of the surface–atmosphere system over polar regions.

© 2014 Elsevier B.V. All rights reserved.

## Contents

1. Introduction . . . . .	109
2. Ground-based remote sensing measurements . . . . .	111
2.1. Spectral measurements of aerosol optical thickness . . . . .	111
2.1.1. Measurements in the Arctic . . . . .	114
2.1.2. Measurements in Antarctica . . . . .	123
3. Ship-borne measurements . . . . .	126
3.1. Aerosol measurements in the Arctic Ocean . . . . .	127
3.1.1. Northern Greenland Sea and Norwegian Sea . . . . .	128
3.1.2. Barents Sea and West Siberian Sea . . . . .	128
3.1.3. North American Arctic Ocean . . . . .	128
3.2. Aerosol measurements in the Antarctic Ocean . . . . .	129
3.2.1. Southern Indian Ocean . . . . .	129
3.2.2. Southern Pacific Ocean . . . . .	131
3.2.3. Southern Atlantic Ocean . . . . .	131
3.2.4. Around the Antarctic Peninsula . . . . .	132
4. Aerosol backscattering coefficient profiles from lidar measurements . . . . .	133
5. Airborne and satellite measurements . . . . .	136
5.1. Basic remarks . . . . .	136
5.2. Aerosol optical thickness retrievals over snow and ice using backscattered solar light . . . . .	140
6. Optical characteristics of Arctic and Antarctic aerosols . . . . .	144
6.1. Arctic aerosol particle size-distributions and optical characteristics . . . . .	144
6.2. Antarctic aerosol particle size-distributions and optical properties . . . . .	146
6.3. Evaluations of direct aerosol-induced radiative forcing effects in polar regions . . . . .	148
7. Conclusions . . . . .	151
Acknowledgements . . . . .	152
References . . . . .	152

## 1. Introduction

Aerosols are one of the greatest sources of uncertainty in climate modelling, as their microphysical, chemical and optical characteristics as well as their concentration vary in time and in space, inducing significant direct radiative forcing effects on the surface–atmosphere system. In addition, they can alter cloud optical features and indirectly impact climate. The aim of this paper is to present an overview of the optical characteristics of atmospheric aerosol observed in polar regions during the past two decades, including recent measurements conducted with ground-based and ship-borne sun-photometers, or retrieved from remote sensing data recorded with visible and infrared sensors mounted onboard various satellite platforms. Optical instruments (e.g., lidars, sun-photometers) measure the characteristics of the atmospheric light field (internal, reflected, or transmitted). Specific procedures therefore need to be applied to convert optical signals to aerosol characteristics, such as particle size and shape distributions, or chemical composition. Similar procedures are also needed to derive the vertical concentration distribution from columnar measurements. They are based on the

solution of the inverse problem of radiative transfer theory accounting for multiple light scattering, molecular and aerosol scattering and absorption, and surface reflectance effects.

The presence of a visibility-reducing haze in the Arctic was already noted by early explorers in the 19th century (see [Garrett and Verzella, 2008](#), for a historical overview). The explorers also documented that haze particles were deposited on snow in remote parts of the Arctic (e.g., [Nordenskiöld, 1883](#)) and haze layers were also observed later by pilots in the 1950s ([Mitchell, 1957](#)). The source of the haze was debated for almost a century but poorly understood until the 1970s when it was suggested that this “Arctic Haze” originated from emissions in northern mid-latitudes and was transported into the Arctic over thousands of kilometres ([Rahn et al., 1977](#); [Barrie et al., 1981](#)). The seasonality of the haze, which peaks in winter and early spring, was explained by the fact that removal processes are inefficient in the Arctic during that time of the year ([Shaw, 1995](#)).

Polar aerosols originate from both natural and anthropogenic sources ([Shaw, 1988, 1995](#)). In the Arctic regions, natural aerosols have been found to contain an oceanic sea-salt mass fraction that frequently

exceeds 50% on summer days, and a mass fraction of 30–35% due to mineral dust, with lower percentages of non-sea-salt (nss) sulphate, methane sulphonic acid (MSA), and biomass burning combustion products. In contrast, anthropogenic particles have higher concentrations of sulphates, organic matter (OM) and black carbon (BC) with respect to natural aerosol (Quinn et al., 2002, 2007; Sharma et al., 2006). In fact, boreal forest fire (hereinafter referred to as BFF) smoke transported from North America and Siberia often contributes to enhance soot concentration in summer (Damoah et al., 2004; Stohl et al., 2006). Rather high aerosol mass concentrations of anthropogenic origin are frequently transported from North America and especially Eurasia in the winter and spring months, leading to intense Arctic haze episodes (Shaw, 1995). For instance, Polissar et al. (2001) conducted studies on the BC source regions in Alaska from 1991 to 1999 finding that predominant contributions have been given by large-scale mining and industrial activities in South and Eastern Siberia. In the North European sector of the Arctic, the dominant sources of sulphates and nitrates (and to a lesser extent of water-soluble OM and BC) are located in Europe and Siberia, due to both urban pollution and industrial activities (Hirdman et al., 2010). Episodes of Asian dust transport have also been observed over the past years in the North American sector of the Arctic, especially in spring (Stone et al., 2007), together with local transport of soil particles mobilised by strong winds, which provisionally enhance the mass concentrations of elemental components, such as Al, Si, Mg and Ca (Polissar et al., 1998). The Arctic atmosphere's stratification is highly stable, with frequent and strong inversions near the surface, which limit turbulence and reduce the dry deposition of aerosols to the surface (Strunin et al., 1997). They also decouple the sea ice inversion layer from the Arctic free troposphere, leading to very different chemical and physical properties of aerosols in the sea ice inversion layer where aerosols are depleted, and higher up where a sulphate-rich background aerosol typically of anthropogenic origin is often found (Brock et al., 2011). In addition, organic-rich biomass burning layers occur in the free troposphere but rarely reach the surface (Warneke et al., 2010; Brock et al., 2011). The low-altitude high-latitude atmosphere in the southern hemisphere is similarly stably stratified as in the Arctic's but is also influenced strongly by katabatic winds bringing down air from the high altitudes of interior Antarctica (Stohl and Sodemann, 2010).

On larger scales, the stable Arctic stratification leads to the so-called polar dome, where isentropes form shells above the Arctic. As atmospheric transport tends to follow the isentropes, direct transport of air masses from mid-latitude pollution source regions into the Arctic lower troposphere is very inefficient. According to Stohl (2006), polluted air masses from lower latitudes typically follow one of five major transport pathways (see Fig. 1): (1) lifting at the Arctic front, where wet scavenging is efficient; (2) lifting at lower latitudes (at the polar front or convection), where wet scavenging is even more efficient;

(3) most importantly for Arctic surface aerosol concentrations, low-level transport over land in winter where strong radiative cooling allows air masses to enter the polar dome; (4) slow descent by radiative cooling of upper-tropospheric air masses into the polar dome; (5) slow mixing across the lateral boundaries of the dome. Forest or agricultural fires are important, as they produce strong aerosol plumes in the mid-to high-latitude free troposphere, which can subsequently enter the Arctic by one of the previously mentioned processes.

In addition to long-range pollution transport, local emission sources can be important. For instance, emissions from cruise ships can lead to measurable enhancements of BC and other aerosols in the Svalbard archipelago (Eckhardt et al., 2013). Diesel generators can also locally pollute the environment (Hagler et al., 2008). Aircraft emissions north of the Arctic circle are primarily injected into the stratosphere where removal is inefficient and these emissions can slowly descend (Whitt et al., 2011). All these local sources can also enhance the Arctic aerosol background; however, quantification of their contribution relative to long-range transport of pollution from sources outside the Arctic remains uncertain. In addition, sulphate and volcanic ash from high-latitude eruptions can occasionally influence the Arctic troposphere (e.g., Hoffmann et al., 2010). The stratospheric background aerosol in the Arctic as elsewhere can be perturbed by explosive volcanic eruptions (especially in the tropics) for several years. Some volcanic aerosol emission episodes have been observed by Bourassa et al. (2010) and O'Neill et al. (2012) over the last few years, involving the low stratosphere over short periods of a few months.

Transport processes in the high-latitude southern hemisphere are similar to those sketched for the Arctic in Fig. 1. As in the northern hemisphere, polluted air masses from the lower-latitude continents are quasi-isentropically lifted to higher altitudes and, furthermore, there is no low-altitude transport pathway over land in winter (i.e., the analogue to transport pathway number 3 in Fig. 1 is missing in the southern hemisphere). Consequently, as in the Arctic, the lowermost troposphere in the Antarctic is very isolated and, thus, contains little anthropogenic pollution transported from lower-latitude continents (Stohl and Sodemann, 2010). A major difference to the Arctic, however, is the high topography of the Antarctic continent. This means that the most isolated air masses (as measured by the time since last exposure to pollution sources at lower-latitude continents) are not found close to the pole, as in the Arctic, but in the coastal areas surrounding Antarctica (Stohl and Sodemann, 2010). Descent over the Antarctic continent is stronger than over the Arctic and can also bring down air from the stratosphere, and air from the Antarctic interior is transported down to coastal areas by strong katabatic winds.

In Antarctica, aerosols sampled at coastal sites originate almost totally from natural processes, with a prevailing oceanic sea-salt mass content of 55–60%, and lower percentages of nss sulphate (20–30%)

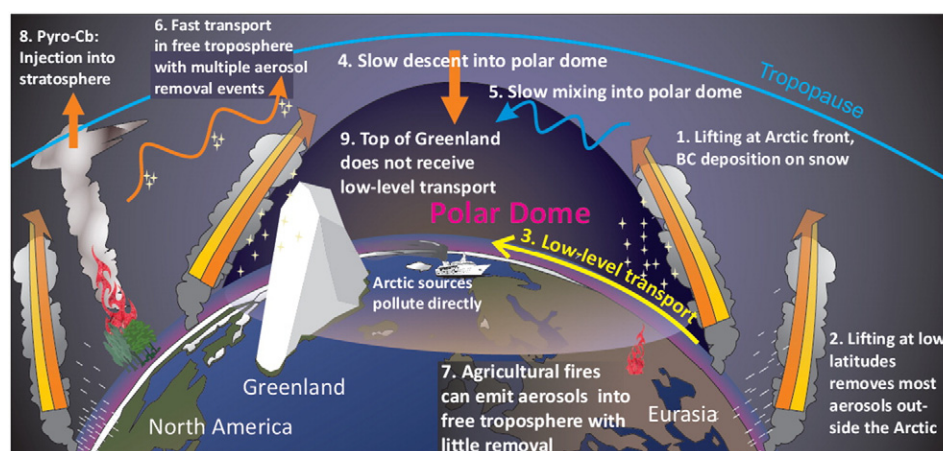


Fig. 1. Schematic of the main transport pathways of aerosols into the Arctic, as described by Law et al. (in press) [used with permission of the American Meteorological Society].



and mineral dust (10–20%) (Tomasi et al., 2012). Only very low mass fractions of nitrates, water-soluble OM and BC have been monitored in Antarctica, mainly associated with transport from remote anthropogenic sources (Wolff and Cachier, 1998) or biomass burning (Fiebig et al., 2009) in mid-latitude areas. More than 60–80% of particulate matter suspended over the Antarctic Plateau has been estimated to consist of nss sulphates formed from biogenic sulphur compounds and/or MSA, due to long-range transport in the free troposphere and subsequent subsidence processes. Therefore, aerosols sampled at these high-altitude sites contain only moderate mass fractions of nitrates, and minor or totally negligible mass percentages of mineral dust, water-soluble OM and BC (Tomasi et al., 2007, 2012).

The paper is organised as follows. In the next section the ground-based remote sensing measurements of atmospheric aerosol are reviewed (sun-photometers, lidars). Section 3 gives a description of ship-borne aerosol remote sensing instruments. Section 4 discusses aerosol backscattering coefficient profiles from lidar measurements, while Section 5 is dedicated to airborne and satellite observations of polar aerosols. The last section presents the most important optical characteristics and size-distribution features of polar aerosols, which are appropriate for calculations of direct radiative forcing effects induced by aerosols on the climate system.

## 2. Ground-based remote sensing measurements

### 2.1. Spectral measurements of aerosol optical thickness

Ground-based remote sensing of the optical characteristics of aerosols in the atmospheric column is usually conducted with multi-wavelength sun-photometers. A sun-photometer is oriented towards the Sun to detect the solar radiation attenuated along the slant path from the top-of-atmosphere (TOA) to the ground. The atmospheric aerosol load leads to a decrease in the solar radiation transmitted through the atmosphere. This decrease depends on the aerosol optical thickness (hereinafter referred to as AOT and/or using symbol  $\tau(\lambda)$ ), which is given by the integral of the volume aerosol extinction coefficient along the vertical path of the atmosphere.

The networks, sites and sun-photometers whose data were employed in this paper are defined and characterised in Tables 1 and 2 for the Arctic and Antarctic regions, respectively. The largest networks of sun-photometers in the world are AERONET and SKYNET. Spectral measurements of  $\tau(\lambda)$  are performed with AERONET sun-photometers (Holben et al., 1998) at 8 wavelengths ranging from 0.340 to 1.600  $\mu\text{m}$ , and with SKYNET instruments (Nakajima et al., 2007) at 10 wavelengths from 0.315 to 2.200  $\mu\text{m}$ . The Cimel CE-318 sun-photometers of the AERONET network are currently used at several Arctic sites: Barrow (since March 2002), Thule (since March 2007), Hornsund (since April 2005), Sodankylä (since February 2007), Tiksi (since June 2010), Resolute Bay (since July 2004), Eureka-OPAL (since April 2007) and Eureka-PEARL (since May 2007). The last three sites, located in the Nunavut region of Canada, are part of the AEROCAN/AERONET network. In addition, an AERONET sun-photometer has been intermittently used since 2002 by the Atmospheric Optics Group (GOA) (University of Valladolid, Spain) at the Arctic Lidar Observatory for Middle Atmosphere Research (ALOMAR), located on the Andøya Rocket Range, near Andenes (Northern Norway) (Toledano et al., 2012). AERONET sun-photometers have been used to obtain Level 2.0  $\tau(\lambda)$  measurements at the South Pole (since November 2007), and occasionally at Dome Concordia (in January and December 2003) in Antarctica. AERONET Level 1.5 measurements of  $\tau(\lambda)$  are available for McMurdo on the Ross Sea (from February to December 1997, in the austral summer 2001/2002, and in January–February 2011), at Marambio (Antarctic Peninsula) since October 2007, at Vechernaya Hill (Thala Hills, Enderby Land) since December 2008, and at Utsteinen (Dronning Maud Land) since February 2009. However, because these data were not promoted to Level 2.0, they were not considered in the present

study. A PREDE POM-01L sun/sky radiometer was used in Antarctica during the 2001–2002 austral summer by Di Carmine et al. (2005) at the Mario Zucchelli station. PREDE instruments have been used since 2001 in Antarctica at Syowa (East Ongul Island, Lützow-Holm Bay) by the National Institute of Polar Research (NIPR, Tokyo, Japan) since 2001, at Rothera by the British Antarctic Survey (BAS) since January 2008, and at Halley by BAS since February 2009. In addition, Precision Filter Radiometer (PFR) sun-photometers (Wehrli, 2000; Nyeki et al., 2012) from the Global Atmosphere Watch (GAW) PFR network are currently used in the Arctic at Summit by PMOD/WRC (Switzerland), at Ny-Ålesund by NILU (Norway), and at Sodankylä by FMI (Finland), and in Antarctica at Marambio by FMI and at Troll by NILU. The instrumental and geometrical characteristics of the PFR sun-photometer are described by Wehrli (2000).

The monochromatic total optical thickness  $\tau_{TOT}(\lambda)$  of the atmosphere is commonly calculated in terms of the well known Lambert–Beer law for a certain sun-photometer output voltage  $J(\lambda)$  taken within a spectral channel centred at wavelength  $\lambda$  and for a certain apparent solar zenith angle  $\theta_0$ . The monochromatic value of  $\tau_{TOT}(\lambda)$  is given by (Shaw, 1976):

$$\tau_{TOT}(\lambda) = (1/m) \ln[RJ_0(\lambda)/J(\lambda)], \quad (1)$$

where: (i)  $m$  is the relative optical air mass calculated as a function of  $\theta_0$  using a realistic model of the atmosphere, in which wet-air refraction and Earth/atmosphere curvature effects on the direct solar radiation passing through the atmosphere are properly taken into account (Thomason et al., 1983; Tomasi and Petkov, 2014); (ii)  $J(\lambda)$  is the output signal (proportional to solar irradiance) measured by the ground-based solar pointing sun-photometer; (iii)  $J_0(\lambda)$  is the output signal that would be measured by the sun-photometer outside the terrestrial atmosphere, at the mean Earth–Sun distance; and (iv)  $R$  accounts for  $J_0(\lambda)$  variations as a function of the daily Earth–Sun distance (Iqbal, 1983).

The solar radiation reaching the surface for cloud-free sky conditions is attenuated not only by aerosol extinction but also by Rayleigh scattering (Tomasi et al., 2010) as well as absorption by minor gases (mainly water vapour ( $\text{H}_2\text{O}$ ), ozone ( $\text{O}_3$ ), nitrogen dioxide ( $\text{NO}_2$ ) and its dimer ( $\text{N}_2\text{O}_4$ ), and oxygen dimer ( $\text{O}_4$ )). The spectral values of  $\tau(\lambda)$  within the main windows of the atmospheric transmission spectrum are accordingly calculated by subtracting the Rayleigh scattering and absorption optical thicknesses from  $\tau_{TOT}(\lambda)$ .

AOT is usually a smooth function of wavelength  $\lambda$  (measured in  $\mu\text{m}$ ), which can be approximated by the following simple formula:

$$\tau(\lambda) = \tau(\lambda_0)(\lambda/\lambda_0)^{-\alpha}, \quad (2)$$

where  $\alpha$  is the so-called Ångström (1964) wavelength exponent, and  $\lambda_0$  is usually assumed to be equal to 1  $\mu\text{m}$ . In reality, the analytical form defined in Eq. (2) can be convex or concave depending on the relative contents of fine and coarse particles in the atmospheric column. O'Neill et al. (2001a) demonstrated that the variation in  $\tau(\lambda)$  and its first and second spectral derivatives (named here  $\alpha$  and  $\alpha'$ , respectively) can be realistically described in terms of the spectral interaction between the individual optical components of a bimodal size-distribution. O'Neill et al. (2001a) then showed that one can exploit the spectral curvature information in the measured  $\tau(\lambda)$  to permit a direct estimate of a fine mode Ångström exponent ( $\alpha_f$ ) as well as the optical fraction of fine mode particles. However, an analysis of  $\alpha$  and  $\alpha'$  determined in real cases and taking into account that both  $\alpha(0.44\text{--}0.87 \mu\text{m})$  and  $\alpha'$  are closely related to the spectral features of  $\tau(\lambda)$  showed that propagation of errors leads to an error  $\Delta\alpha/\alpha \sim 2 \Delta\tau(\lambda)/\tau(\lambda)$  and an error  $\Delta\alpha'/\alpha' \sim 5\Delta\tau(\lambda)/\tau(\lambda)$ , respectively (Gobbi et al., 2007). These estimates yield values of  $\Delta\alpha/\alpha$  and  $\Delta\alpha'/\alpha'$  that are  $\sim 20\%$  and  $\sim 50\%$ , respectively, for  $\tau(\lambda) \leq 0.10$  and a typical sun-photometry error equal to  $\sim 0.01$ . To avoid relative errors  $> 30\%$  in



**Table 1**  
List of the Arctic stations, where regular ground-based sun-photometer measurements have been conducted over the past decades, using different instrument models equipped with a variable number of narrow-band interference filters to determine the spectral values of aerosol optical thickness  $\tau(\lambda)$  and Ångström wavelength exponent  $\alpha$  in the visible and near-infrared wavelength range.

Sun-photometer stations	Managing institutions	Geographical coordinates and altitude	Overall number of measurement days	Measurement period	Sun-photometer model	Peak wavelengths (nm) of the spectral channels	Spectral interval (nm) of $\alpha$	References
Barrow, Alaska (USA)	GMD/NOAA, Boulder, Colorado, USA	71° 19' N, 156° 36' W, 8 m a.m.s.l.	832 (cloud-screened by GMD/NOAA)	March 2000–September 2012	Carter Scott SP02 Carter Scott SP01-A Carter Scott SP022	412, 500, 675, 862 367, 610, 778, 1050 368, 610, 778, 1050	412–862 367–778 368–778	Stone (2002)
Barrow, Alaska (USA)	AERONET, NASA/GSFC, (Greenbelt, Maryland, USA); U.S. DoE Atmospheric Radiation Measurement Program, USA	71° 19' N, 156° 40' W, 0 m a.m.s.l.	579 (Level 2.0)	March 2002–September 2013	Cimel CE-318	340, 380, 440, 500, 675, 870, 1020, 1640	440–870	Holben et al. (1998)
Resolute Bay, Nunavut (Canada)	AERONET/AEROCAN, Environment Canada, Downsview, Ontario, Canada	74° 44' N, 94° 54' W, 40 m a.m.s.l.	361 (Level 2.0)	July 2004–October 2012	Cimel CE-318	340, 380, 440, 500, 675, 870, 1020, 1640	440–870	
Eureka-OPAL, Nunavut (Canada)	AERONET/AEROCAN, CARTEL, University of Sherbrooke, Canada	79° 59' N, 85° 56' W, 0 m a.m.s.l.	360 (Level 2.0)	April 2007–September 2011	Cimel CE-318	340, 380, 440, 500, 675, 870, 1020, 1640	440–870	
Alert, Ellesmere Island, Nunavut (Canada)	GMD/NOAA, Boulder, Colorado, USA	82° 28' N, 62° 30' W, 210 m a.m.s.l.	810 (cloud-screened by GMD/NOAA)	August 2004–September 2012	Carter Scott SP02	412, 500, 675, 862, or 368, 610, 778, 1050	412–862 or 368–778	Stone (2002)
Thule, NW Greenland	AERONET, NASA/GSFC, Greenbelt, Maryland, USA	76° 31' N, 68° 46' W, 225 m a.m.s.l.	605 (Level 2.0)	March 2007–September 2012	Cimel CE-318	380, 440, 500, 675, 870, 1020	440–870	Holben et al. (1998)
Summit, Central Greenland	PMOD/WRC, Davos, Switzerland	72° 35' N, 38° 28' W, 3250 m a.m.s.l.	391 (cloud-screened by PMOD/WRC)	January 2001–October 2011	PFR#34	368, 412, 500, 862	412–862	Wehrli (2000)
Ittoqqortoormiit, Eastern Greenland	AERONET, NASA/GSFC, Greenbelt, Maryland, USA	70° 29' N, 21° 57' W, 68 m a.m.s.l.	307 (Level 2.0)	May 2010–October 2013	Cimel CE-318	340, 380, 440, 500, 675, 870, 1020	440–870	Holben et al. (1998)
Ny-Ålesund, Spitsbergen (Svalbard, Norway)	AWI, Bremerhaven, Germany	78° 54' N, 11° 53' E, 5 m a.m.s.l.	749 (cloud-screened by AWI)	April 2000–September 2013	SP1A SP2H STAR01	371, 380, 416, 443, 500, 532, 609, 675, 778, 864, 1025, 1046, 1062 367, 380, 413, 441, 501, 531, 605, 673, 776, 862, 1023, 1045 390, 441, 501, 531, 605, 673, 776, 862	443–864 441–862 441–862	Herber et al. (2002)
Ny-Ålesund, Spitsbergen (Svalbard, Norway)	NILU, Kjeller, Norway	78° 54' N, 11° 53' E, 5 m a.m.s.l.	693 (cloud-screened by NILU)	March 2002–September 2004, and March 2006–September 2013	PFR#18	367.7, 411.9, 500.6, 862.5	411.9–862.5	Wehrli (2000)
Barentsburg, Spitsbergen (Svalbard, Norway)	IAO-SB-RAS, Tomsk, Russia	78° 04' N, 14° 13' E, 20 m a.m.s.l.	56 (cloud-screened by IAO)	April–August of 2011 and 2012	New portable SPM	339, 380, 442, 500, 547, 675, 871, 1020, 1240, 1553, 2134	442–871	Sakerin et al. (2009, 2012, 2014)
Hornsund, Spitsbergen (Svalbard, Norway)	AERONET, NASA/GSFC, Greenbelt, Maryland, USA; Institute of Geophysics, PAS, Warsaw, Poland	77° 00' N, 15° 34' E, 10 m a.m.s.l.	514 (Level 2.0)	April 2005–August 2013	Cimel CE-318	380, 440, 500, 675, 870, 1020	440–870	Holben et al. (1998)
Sodankylä, Northern Finland	FMI, Helsinki, Finland	67° 22' N, 26° 38' E, 184 m a.m.s.l.	312 (cloud-screened by FMI)	May 2004–September 2013	PFR#32	367.6, 411.4, 500.5, 861.6	411.4–861.6	Wehrli (2000)
Sodankylä, Northern Finland	AERONET, NASA/GSFC, Greenbelt, Maryland, USA; FMI, Helsinki, Finland	67° 22' N, 26° 38' E, 184 m a.m.s.l.	119 (Level 2.0)	February 2007–November 2013	Cimel CE-318	340, 380, 440, 500, 675, 870, 1020, 1640	440–870	Holben et al. (1998)
Tiksi, Northern-Central Siberia (Russia)	AERONET, NASA/GSFC, Greenbelt, Maryland, USA	71° 35' N, 128° 55' E, 0 m a.m.s.l.	162 (Level 2.0)	June–October of 2010, 2011 and 2012	Cimel CE-318	340, 380, 440, 500, 675, 870, 1020	440–870	Holben et al. (1998)

**Table 2**  
List of the coastal and high-altitude Antarctic stations, where regular ground-based sun-photometer measurements have been conducted over the two past decades, using different instrument models equipped with a variable number of narrow-band interference filters to determine the spectral values of background aerosol optical thickness  $\tau(\lambda)$  and Ångström wavelength exponent  $\alpha$  in the visible and near-infrared wavelength range.

Sun-photometer stations	Managing institutions	Geographical coordinates and altitude	Overall number of measurement days	Measurement period	Sun-photometer model	Peak wavelengths (nm) of the aerosol spectral channels	Spectral interval (nm) of $\alpha$	References
Marambio, Seymour-Marambio Island Neumayer, Weddell Sea coast	FMI, Heksinki, Finland	64° 14' S, 56° 37' W, 205 m a.m.s.l.	139 (cloud-screened by FMI)	August 2011–March 2013	PFR #29	367.6, 411.4, 500.5, 861.6	367.6–861.6	Wehrli (2000)
	AWI, Bremerhaven, Germany	70° 39' S, 8° 15' W, 40 m a.m.s.l.	234 (cloud-screened by AWI)	September 2000–April 2007	SP1A	371, 380, 416, 443, 500, 532, 609, 675, 778, 864, 1025, 1046, 1062	443–864	Herber et al. (2002)
					SP2H	367, 380, 413, 441, 501, 531, 605, 673, 776, 862, 1023, 1045	441–862	
					STAR01	390, 441, 501, 531, 605, 673, 776, 862	441–862	
Troll, Queen Maud Land	NILU, Kjeller, Norway	72° 01' S, 2° 32' E, 1309 m a.m.s.l.	547 (cloud-screened by NILU)	January 2007–April 2013	PFR#40 PFR#42	368.7, 411.9, 500.6, 862.5 368.9, 412.1, 499.7, 862.2	411.9–862.5 412.1–862.2	Wehrli (2000)
Novolazarevskaya, Queen Maud Land	AARI, San Petersburg, Russia; AERONET, NASA/GSFC, Greenbelt, Maryland, USA.	70° 46' S, 11° 50' E, 119 m a.m.s.l.	83 (Level 1.5, cloud-screened by NASA/GSFC)	December 2008–February 2009; November 2009–February 2010	Hand-held Microtops, calibrated at GSFC	440, 500, 675, 870	440–870	Smirnov et al. (2009)
Mirny, Davis Sea coast	AARI, St. Petersburg, Russia	66° 33' S, 93° 01' E, 40 m a.m.s.l.	725 (ABAS and SPM data cloud-screened by AARI; Microtops data cloud-screened using the Smirnov et al. (2009) procedure)	March 2000–October 2013	ABAS	395, 408, 479, 581, 651, 789, 873, 1041	408–873	Radionov et al. (2002), Radionov (2005) Sakerin et al. (2009, 2012), Tomasi et al. (2012) Smirnov et al. (2009) Ohno (2005)
					SPM	340, 379, 443, 499, 548, 676, 871, 1019, 1244, 1555, 2134	443–871	
					Microtops EKO MS-110 model (with 2.5° field-of-view diameter)	440, 500, 675, 870 368, 500, 675, 778, 862	440–870 368–862	
Syowa, East Ongul Island, Lützow-Holm Bay	Japan Meteorological Agency (JMA), Tokyo, Japan	69° 00' S, 39° 35' E, 21 m a.m.s.l.	987 (cloud-screened by JMA)	January 2000–December 2011	Prede POM-01L	400, 500, 675, 870, 1020	400–870	Di Carmine et al. (2005)
Mario Zucchelli, Terra Nova Bay, Ross Sea coast, Victoria Land	ISAC-CNR, Bologna, Italy	74° 42' S, 164° 07' E, 15 m a.m.s.l.	87 (cloud-screened by ISAC-CNR)	November 2001–February 2002	ASP-15WL	381, 412, 451, 500, 551, 610, 673, 775, 861, 1026	412–861	Tomasi et al. (2007)
Dome Concordia, East Antarctic Plateau	AERONET, NASA/GSFC, Greenbelt, Maryland, USA	75° 05' S, 123° 18' E, 3260 m a.m.s.l.	44 (Level 1.5 data, cloud-screened by NASA/GSFC)	January and December 2003; January 2004	Cimel CE-318	440, 675, 870, 1020	440–870	Holben et al. (1998), Six et al. (2005)
	GMD/NOAA, Boulder, Colorado, USA	75° 06' S, 123° 21' E, 3233 m a.m.s.l.	65 (cloud-screened by GMD/NOAA)	January 2006–November 2010	Carter Scott SP02	412, 500, 675, 862	412–862	Stone (2002)
	OPAR Institute, (Univ. de la Réunion - CNRS, Saint Denis de la Réunion, France), and NASA/GSFC, (Greenbelt, Maryland, USA)	75° 05' E, 123° 18' E, 3260 m a.m.s.l.	39 (Level 1.5 data, cloud-screened by NASA/GSFC)	January, 2010, 2011, and 2012	Hand-held Microtops calibrated at the NASA/GSFC Facility	379, 441, 674, 868	441–868	Smirnov et al. (2011)
South Pole, Antarctic Plateau	GMD/NOAA, Boulder, Colorado, USA	90° 00' S, 00° 00' E, 2835 m a.m.s.l.	1279 (cloud-screened by GMD/NOAA)	November 2001–March 2012	Carter Scott SP02	412, 500, 675, 862	412–862	Stone (2002)
	AERONET, NASA/GSFC, Greenbelt, Maryland, USA; GMD/NOAA, Boulder, Colorado, USA	89° 59' S, 70° 18' E, 2850 m a.m.s.l.	147 (Level 2.0 data, cloud-screened by NASA/GSFC)	November 2007–December 2012	Cimel CE-318	340, 380, 440, 500, 675, 870, 1020	440–870	Holben et al. (1998)

$\Delta\alpha'/\alpha'$ , Gobbi et al. (2007) suggested using only observations of  $\tau(\lambda) > 0.15$ . We applied the same criterion as a threshold for accepting outputs from the Spectral Deconvolution Algorithm (SDA) of O'Neill et al. (2003) (notably the fine mode Ångström exponent, which offers an alternative refinement to the calculation of  $\alpha$ ): our logic being that  $\alpha$  and  $\alpha'$  are input parameters to SDA and we did not want to introduce unacceptable processing errors to the extraction of a spectral exponent indicator. These limitations to the use of spectral values of  $\alpha$  and  $\alpha'$  were also applied by Yoon et al. (2012), who only considered observations with  $\tau(0.44 \mu\text{m}) > 0.15$  in order to avoid relative errors  $> 30\%$  in  $\alpha'$ . Tomasi et al. (2007) showed that for the period 1977–2006,  $\tau(0.50 \mu\text{m})$  did not exceed 0.15 for background summer aerosol conditions at Barrow, Alert, Summit, Ny-Ålesund, Hornsund, Sodankylä and Andenes/ALOMAR in the Arctic, and was greater than 0.15 only during very strong episodes of Arctic haze in late winter and spring, and BFF smoke transport in summer. Similarly, Tomasi et al. (2012) found that (i) the measurements of  $\tau(0.50 \mu\text{m})$  recorded from 2000 to 2012 at Ny-Ålesund were estimated to exceed 0.15 in summer (June to September) in only a few cases of strong transport of BFF smoke from lower latitudes; even in winter (December to March), they were higher than 0.15 only for 10% of the cases, typically associated with Arctic haze transport episodes; (ii) measurements of  $\tau(0.50 \mu\text{m}) > 0.15$  recorded at Barrow over the same period were observed only in a few percent of cases, as a result of Arctic haze; and (iii) daily mean background summer values of  $\tau(0.50 \mu\text{m})$  measured at Tiksi in Siberia were always lower than 0.08 during the summer 2010. With regard to Antarctic aerosol, Tomasi et al. (2007) estimated that the daily mean values of  $\tau(0.50 \mu\text{m})$  were lower than 0.10 during the austral summer months at Marambio, Neumayer, Aboa, Mirny, Molodezhnaya, Syowa, Mario Zucchelli, Kohnen, Dome Concordia and South Pole. In particular, examining the sun-photometer measurements carried out from 2005 to 2010, Tomasi et al. (2012) reported that the austral summer values of  $\tau(0.50 \mu\text{m})$  measured at Neumayer and Mirny were  $< 0.10$  during the whole season, while those measured at South Pole never exceeded 0.06.

Therefore, since the values of  $\tau(0.44 \mu\text{m})$  determined from the sun-photometer measurements conducted in polar regions are mostly lower than 0.15 and thus below the value recommended by Gobbi et al. (2007), we have decided not to determine the exponent  $\alpha_f$  using the O'Neill et al. (2001b) algorithm, but to calculate the best-fit value of the Ångström exponent  $\alpha$  over the spectral range  $0.40 \leq \lambda \leq 0.87 \mu\text{m}$  using Eq. (2). In real cases, the exponent  $\alpha$  provides by itself a first rough estimate of the optical influence of the fine particle component on  $\tau(\lambda)$ , since it gradually decreases on average from cases where fine particle extinction predominates to cases where coarse particles are optically predominant.

In all cases with relatively high values of  $\tau(0.50 \mu\text{m})$ , the AERONET and SKYNET sun/sky radiometers can also be used to provide regular measurements of sky-brightness along the solar almucantar (an azimuthal circle around the local normal whose zenith angle equals the solar zenith angle  $\theta_0$ ) and also in the principal plane containing the direction to the Sun and the local normal. The analysis of these measurements enables better constraints for solving the inverse problem (while accounting for multiple scattering and surface reflectance effects) and allowing the following parameters to be derived: (i) the aerosol single scattering albedo  $\omega(\lambda)$ , (ii) the phase function  $P(\theta)$ , (iii) the particle number density size-distribution  $N(r) = dN(r)/d(\ln r)$  given as a function of particle radius  $r$ , and (iv) the complex refractive index  $n(\lambda) - ik(\lambda)$  (King and Dubovik, 2013).

The data analysis performed in this paper was subject to certain data processing constraints across networks of instruments. In the first instance, all network protocols differ in many (typically) minor details such as the means of estimating molecular optical thicknesses and solar air masses, the nominal time interval between measurements and calibration protocols. In general, all data-sets were cloud-screened using temporal-based criteria that were developed and rigorously

tested by each network group. Only Level 2.0 AERONET data were used: this corresponds to temporal-based cloud-screened data (Smirnov et al., 2000) that has undergone a final quality assurance step. The GMD/NOAA data acquired at Barrow and Alert were further cloud-screened using a spectral criterion wherein  $\tau(\lambda)$  spectra were eliminated for  $\alpha < 0.38$ . This added cloud-screening feature was found to be necessary in order to eliminate the influence of homogeneous, thin cirrus clouds that has escaped the temporal cloud-screening step. Finally we note that the specific spectral ranges of the  $\alpha$  computations, while being nominally limited to  $0.40 \leq \lambda \leq 0.87 \mu\text{m}$  are given in Tables 1 and 2 for each type of instrument (the  $\alpha$  regression was carried out for all wavelength channels between and including the wavelength extremes given in the "Spectral interval" column).

Before presenting the evaluations of the seasonal variations in parameters  $\tau(0.50 \mu\text{m})$  and  $\alpha$  measured at the various Arctic and Antarctic sites, it seems useful for the reader to give a measure of the experimental errors and variability features associated with the aerosol optical characteristics varying as a function of aerosol origin and their chemical composition evolutionary patterns:

- (i) the mean experimental error of AOT measured with the most sophisticated sun-photometers leads to an uncertainty of  $\sim 0.01$  in the visible and near-IR, mainly due to calibration errors (Eck et al., 1999);
- (ii) the relative errors of exponent  $\alpha$  determined in terms of Ångström's (1964) formula is about twice the relative error of AOT (Gobbi et al., 2007), therefore leading to obtain at polar sites relative errors close to 30% and, hence, absolute errors of  $\sim 0.50$  (Mazzola et al., 2012); and
- (iii) the spread of  $\alpha$  arising from the natural variability of Arctic and Antarctic aerosol types has been estimated by Stone (2002), Tomasi et al. (2007) and Treffeisen et al. (2007) to yield average uncertainties of  $\pm 0.4$  for Arctic summer background aerosols,  $\pm 0.6$  for Arctic aerosols including particular cases (like Asian dust and boreal smoke particles), and  $\pm 0.5$  for austral summer background aerosol observed at Antarctic sites.

#### 2.1.1. Measurements in the Arctic

In order to define the seasonal variations in polar aerosol optical characteristics, sun-photometer measurements of  $\tau(\lambda)$  conducted at various visible and near-infrared wavelengths can be conveniently examined to evaluate the exponent  $\alpha$  in terms of Eq. (2). Such measurements have been carried out at various Arctic and Antarctic sites during the past decades, providing useful information on polar aerosol optical and microphysical features. In fact,  $\tau(\lambda)$  gives a measure of the overall aerosol extinction along the vertical atmospheric path, while  $\alpha$  depends on the combination of the different extinction effects produced by nuclei, accumulation and coarse particles. Values of  $\alpha$  higher than 1.3 are usually observed in air masses where Aitken nuclei and very fine particles (having radii  $r < \sim 0.12 \mu\text{m}$ ) optically predominate, while relatively low values of  $\alpha < 1.0$  are observed when accumulation (over the  $0.12 \leq r \leq 1.25 \mu\text{m}$  range) and coarse (over the  $r > 1.25 \mu\text{m}$  range) mode particles produce stronger extinction effects. The vertical profile of the aerosol volume backscattering coefficient can be determined by means of lidar measurements, allowing the classification of aerosol layers in the troposphere and lower stratosphere.

Direct solar radiation measurements have been regularly conducted for cloud-free sky conditions at numerous polar sites over the past decades, using multi-spectral sun-photometers of different design. Tables 1 and 2 list the 12 Arctic sites and 9 Antarctic sites, whose data were employed in this study together with their geographical coordinates, measurement periods, the peak wavelengths of the spectral channels used to measure AOT and determine the best-fit value of  $\alpha$ , and the main references where the technical characteristics of the instruments are detailed. The geographical locations of these sites are separately indicated in Fig. 2 for the Arctic and Antarctic regions.



The individual measurements of the spectral values of  $\tau(\lambda)$  and of the exponent  $\alpha$  obtained from the analysis of the field data recorded for cloud-free sky conditions were then averaged to yield daily means. Since the present analysis is devoted to tropospheric aerosols, the sun-photometer measurements conducted in the presence of stratospheric layers of volcanic particles were removed for the following sites and intervals at: (a) the Arctic sites, in May 2006 (Soufrière Hills eruption), October 2006 (Tavurvur eruption) (Stone et al., 2014), from mid-August to late September 2008 (Kasatochi eruption) (Hoffmann et al., 2010), from early July to early October 2009 (Sarychev eruption) (O'Neill et al., 2012), and in April 2010 (Eyjafjallajökull eruption), as well as the sun-photometer data collected at Barrow during the periods that followed both the Okmok eruption in July 2008, and the Mt. Redoubt eruption in March 2009 (Tomasi et al., 2012); and (b) the Antarctic sites, for all data affected by volcanic features comparable to those of Mt. Pinatubo observed from late spring 1992 to late autumn 1994 (Stone et al., 1993; Stone, 2002). Actually, the Stratospheric Aerosol and Gas Experiment (SAGE II) observations made since 2000 over Antarctica did not provide evidence of appreciable extinction features produced by volcanic particle layers at stratospheric altitudes (Thomason and Peter, 2006; Thomason et al., 2008), as also confirmed by the analysis of sun-photometer measurements conducted at Mirny, Neumayer, Mario Zucchelli and South Pole from 2000 to 2010 (Tomasi et al., 2012).

The remaining daily mean “tropospheric” data collected at each site were then subdivided into monthly sub-sets consisting of data measured in different years, for which the multi-year monthly mean values of  $\tau(0.50 \mu\text{m})$  and  $\alpha$  were determined. Relative frequency histograms (hereinafter referred to as RFHs) were defined separately using the daily mean values of  $\tau(0.50 \mu\text{m})$  and  $\alpha$  collected at Arctic sites during the following seasons: (i) winter–spring, from December to May, when Arctic haze events were most frequent, and (ii) the summer–autumn, from June to October, to characterise background aerosols in summer. For the Antarctic sites, RFHs were determined for austral

summer (from late November to February), to define the mean optical characteristics of background aerosols.

**2.1.1.1. Measurements in Northern Alaska.** Two multi-year sets of sun-photometer measurements from Barrow, located on the Arctic Ocean coast, were analysed in the present study: (a) the first series, acquired with the Carter Scott sun-photometer, was conducted from March 2000 to September 2012 by GMD/NOAA (see Table 1) and consisted of spectral  $\tau(\lambda)$  measurements, taken every minute on apparently cloud-free days and then cloud-screened by applying the GMD/NOAA selection procedure (for  $\alpha(0.412 \mu\text{m}/0.675 \mu\text{m}) < 0.38$ ); and (b) the second series was AERONET data collected from March 2002 to September 2013 (see Table 1). The results are shown in Fig. 3 for the GMD/NOAA and AERONET measurements, where the data coverage is 94% and 78% of the overall 14-year period (March 2000 to September 2013), respectively. The GMD/NOAA monthly mean values of  $\tau(0.50 \mu\text{m})$  increase from about 0.07 in February to more than 0.12 in April and May, and then gradually decrease to less than 0.10 in June and July, and to around 0.05 in October, with (grey toned) standard deviations  $\sigma_{\tau} > 0.05$  from April to July, and  $< 0.03$  in the other months. Similar results were obtained for the AERONET measurements, which exhibited monthly mean values of  $\tau(0.50 \mu\text{m})$  that increased from about 0.12 in March to more than 0.16 in April, and then decreased to 0.10 in June and August and 0.05 in September and October, with  $\sigma_{\tau} > 0.05$  from April to August, and  $< 0.03$  for the other months. The monthly mean values of  $\alpha$  determined from the GMD/NOAA and AERONET measurements were rather stable from February to April, varying from 1.10 to 1.20, with a standard deviation  $\sigma_{\alpha} = 0.3$  on average, followed by a convex cap from April to August, with values close to 1.50 from May to July, and increasing values from 1.30 to ~1.50 in August–October. Fig. 3 also shows the RFHs of the daily mean values of  $\tau(0.50 \mu\text{m})$  and  $\alpha$  measured during the winter–spring and summer–autumn seasonal periods. The analytical curves drawn to represent the RFHs are normal curves and are normalised to yield unit (100%) integration over the measured sampling intervals of

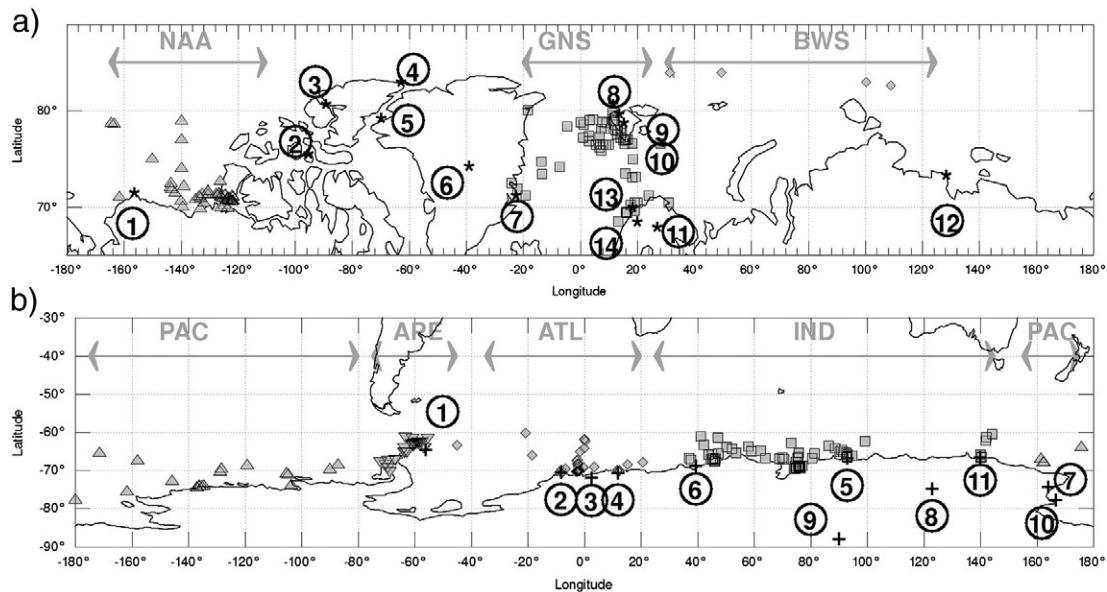


**Fig. 2.** Part (a): Map of the Arctic with the geographical positions of the ground-based sun-photometer stations (solid stars), labelled with the following numbered circles: (1) Barrow, (2) Resolute Bay, (3) Eureka-OPAL, (4) Alert, (5) Thule, (6) Summit, (7) Ittoqqortoormiit, (8) Ny-Ålesund, (9) Barentsburg, (10) Hornsund, (11) Sodankylä, (12) Tiksi, (13) Andenes/ALOMAR, and (14) Kiruna. Grey symbols indicate the geographical positions of ship-borne sun-photometer measurements made on clear-sky days during the AERONET/MAN cruises in three different sectors: (i) Northern Greenland–Norwegian Sea (GNS), between 20° W and 30° E (squares), (ii) Barents Sea and West Siberian Sea (BWS), between 30° E and 130° E (diamonds), and (iii) Eastern Chuckci Sea, Beaufort Sea and Amundsen Gulf (NAA), between 170° W and 110° W (triangles). Part (b): as in the upper part, for the Antarctic ground-based sun-photometer and/or lidar stations (crosses), labelled with the following numbered circles: (1) Marambio, (2) Neumayer, (3) Troll, (4) Novolazarevskaya, (5) Mirny, (6) Syowa, (7) Mario Zucchelli, (8) Dome Concordia, (9) South Pole, (10) McMurdo, and (11) Dumont d’Urville. Grey symbols indicate the geographical positions of the ship-borne sun-photometer measurement days during the AERONET/MAN cruises, subdivided into the four following oceanic sectors: (i) Southern Indian Ocean (IND), between 20° E and 150° E (squares), (ii) Southern Pacific Ocean (PAC), between 150° E and 75° W (upward triangles), (iii) Southern Atlantic Ocean (ATL), between 50° W and 20° E (diamonds), and (iv) Antarctic Peninsula (APE), between 75° and 50° W (downward triangles).

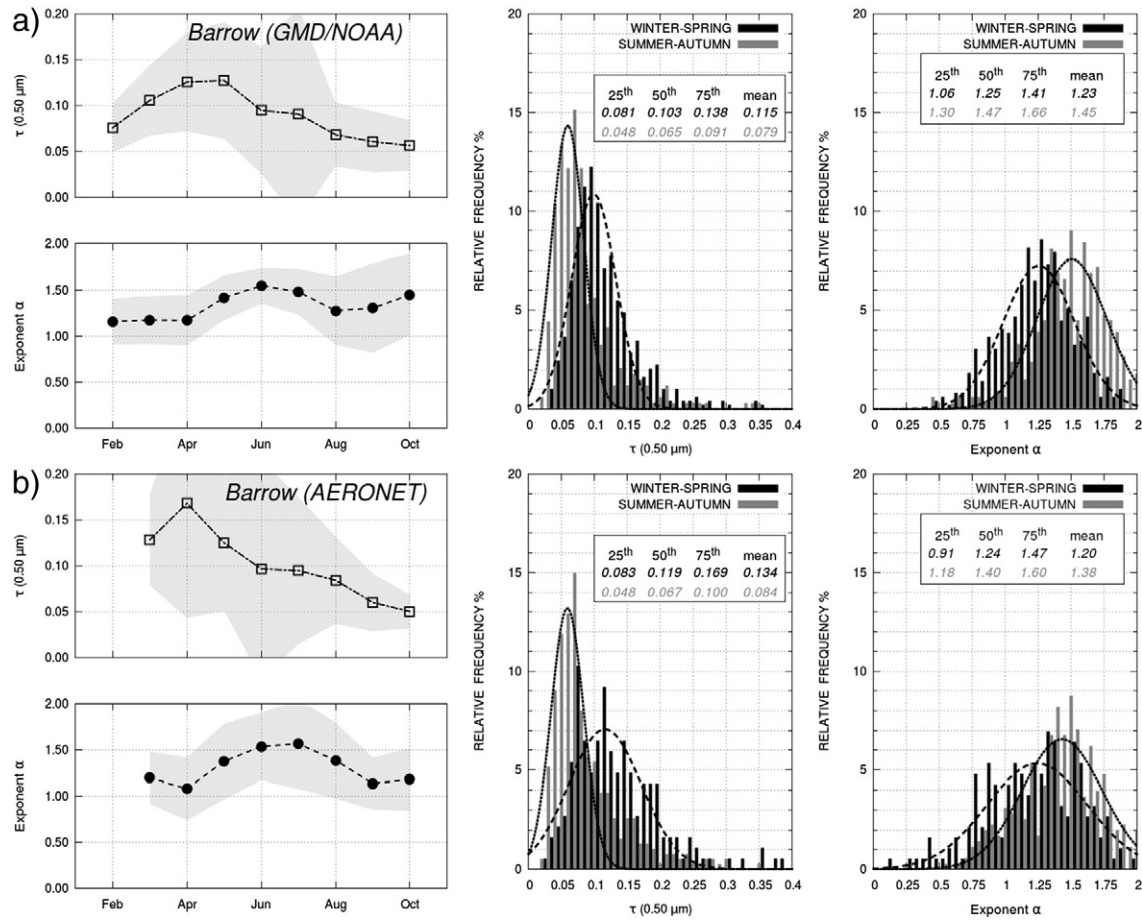


**Fig. 3.** Left-hand side: Time-patterns of the monthly mean values and standard deviations (defined by the grey shaded areas) of aerosol optical thickness  $\tau(0.50 \mu\text{m})$  (open squares) and Angström wavelength exponent  $\alpha$  (solid circles) obtained from both series of multi-year sun-photometer measurements conducted at Barrow (Alaska) by (a) GMD/NOAA (Boulder, Colorado, USA) over the period from March 2000 to September 2012, using the Carter Scott sun-photometers listed in Table 1, and (b) NASA/GSFC (USA) (in cooperation with the Brookhaven National Laboratory (Upton, NY, USA)) over the period from March 2002 to September 2013, using the AERONET Cimel CE-318 sun-photometer having the spectral characteristics given in Table 1. Right-hand side: Relative frequency histograms of  $\tau(0.50 \mu\text{m})$  and exponent  $\alpha$  obtained separately for the winter–spring (Arctic haze) period from December to May (black colour) and the summer–autumn (background aerosol) period from June to October (grey colour). The seasonal mean values and 25th, 50th, and 75th percentiles of  $\tau(0.50 \mu\text{m})$  and  $\alpha$  are reported in the boxes inserted into the graphs, as obtained by examining the daily mean values of both optical parameters measured at this coastal site of the Arctic Ocean in the winter–spring (black italics) and summer–autumn (grey italics) periods.

$\tau(0.50 \mu\text{m})$  and  $\alpha$  shown in Fig. 3. The RFHs for both instruments were very similar, although showing appreciable discrepancies between the means and percentiles, which are in general lower than the corresponding standard deviations. The seasonal mean values of  $\tau(0.50 \mu\text{m})$  were equal to 0.12 and 0.13 in winter–spring, for the GMD/NOAA and AERONET data, respectively, and close to 0.08 in summer–autumn for both data-sets. The RFHs also have long-tails towards high values for winter–spring data, and larger kurtosis in summer–autumn. The long-tail features could in part be ascribed to larger  $\tau(0.50 \mu\text{m})$  values in April and May (ranging from 0.12 to 0.16) attributable to the frequent Arctic haze cases observed in spring but would also be, in part, due to the (asymmetrical) log-normal distribution that is arguably a better fit to the AOT RFHs in general (c.f. O'Neill et al., 2000).

The small discrepancies found between the time-patterns of the monthly mean values of  $\tau(0.50 \mu\text{m})$  and  $\alpha$  defined for both data-sets as well as those between the RFHs of both parameters might well be attributable to slight differences in the total observation periods of both sun-photometers and/or differences in GMD/NOAA and AERONET cloud screening. The different seasonal features of  $\tau(0.50 \mu\text{m})$  and  $\alpha$  shown in Fig. 3 arise mainly from the origins of the aerosol load, associated with the transport of continental polluted air masses mainly from North America and Asia, in winter–spring (Hirdman et al., 2010). It can also be seen in Fig. 3 that the left-hand wings of the RFHs for  $\alpha$  contain some values  $<0.75$ : these are probably due to an optical

predominance of coarse mode sea-salt aerosols and/or local blown dust. Similarly, a fraction of values with  $\alpha < 1.20$  are presumably related to Asian dust transport episodes (Di Piero et al., 2011) that are most frequently observed in March and April, and which are generally characterised by persistent extinction features typical of coarse mineral dust particles (Stone et al., 2007).

**2.1.1.2. Measurements in Northern Canada (Nunavut).** The results derived from the AERONET/AEROCAN measurements conducted at Resolute Bay and Eureka-OPAL, and those carried out by GMD/NOAA at Alert (Canada) (see Table 1) over the past decade are shown in Fig. 4, as obtained for air masses containing aerosols mainly transported from the North American and Arctic Ocean areas (Hirdman et al., 2010) over these three Canadian sites. The monthly mean values of  $\tau(0.50 \mu\text{m})$  exhibit: (i) rather high values related to Arctic haze in March–April, varying between 0.10 and 0.15, and (ii) relatively low values in the subsequent months, decreasing to around 0.05 in September at all the three sites. The month-to-month differences, varying on average from 0.05 at Resolute Bay and Alert in March–June to 0.01 at Alert in September, are similar to or smaller than the monthly mean values of  $\sigma_\tau$ . The winter–spring RFHs exhibit higher mean values of  $\tau(0.50 \mu\text{m})$ , ranging from 0.09 to 0.12, and broader right-hand wings compared to the summer–autumn period, where the RFHs are narrower, giving seasonal mean values varying from 0.06 to no more than 0.08.

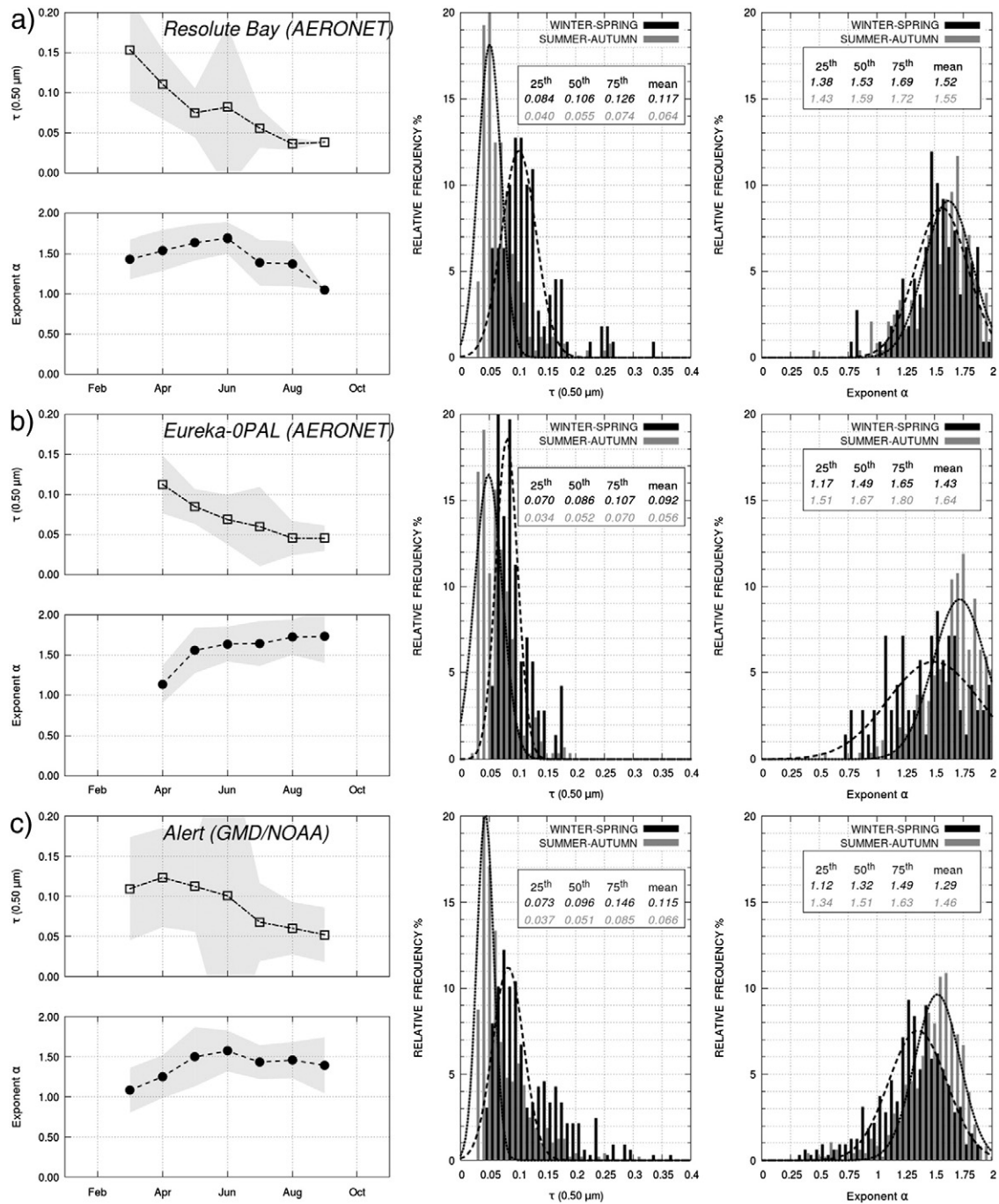


**Fig. 4.** As in Fig. 3, for the multi-year sun-photometer measurements of aerosol optical thickness  $\tau(0.50 \mu\text{m})$  and exponent  $\alpha$  conducted at: (a) Resolute Bay by Environment Canada (Ontario, Canada) over the period from July 2004 to October 2012, using the AERONET/AEROCAN Cimel CE-318 sun-photometer having the spectral characteristics given in Table 1; (b) Eureka-OPAL by CARTEL (Sherbrooke University, Canada) from April 2007 to September 2011, using the AERONET/AEROCAN Cimel CE-318 sun-photometer having the spectral characteristics given in Table 1; and (c) Alert by GMD/NOAA (Boulder, Colorado, USA) from August 2004 to September 2012, using the Carter Scott SP02 sun-photometer, with the characteristics given in Table 1.

Relatively small differences were found between the monthly mean values of  $\alpha$  in winter–spring and summer–autumn, with: (i) stable values close to 1.50 in March–June at Resolute Bay, gradually decreasing to 1.0 in July–September; and (ii) values increasing from 1.0 to 1.5 in March–June at Eureka and Alert, and remaining close to 1.50 from July to September (with  $\sigma_\alpha < \sim 0.3$ ). The monthly mean values of  $\alpha$  determined at Resolute Bay and Eureka-OPAL are appreciably higher than those measured at Barrow, presumably as a result of the weaker extinction produced by coarse sea-salt particles and/or local dust, and weaker contributions of Asian dust in the spring months. Fig. 4 shows that the seasonal RFHs of daily mean  $\alpha$  values do not exhibit symmetrical

shapes: (i) the winter–spring RFHs are rather wide, showing long-tailed left-hand wings and mean values varying from 1.29 (at Alert) to 1.52 (at Resolute Bay), and (ii) the summer–autumn RFHs are characterised by mean values varying from 1.46 (Alert) to 1.64 (Eureka). Only moderate, relative increases in the coarse particle content occurred at Resolute Bay from winter–spring to summer, while greater winter–spring to summer–autumn variations were measured at Eureka and Alert presumably due to fine particle smoke transported from North American boreal forest fires (Stohl et al., 2006). Finally, it is worth noting that a few cases were found with  $\alpha < 0.40$  at Alert, despite the  $\alpha < 0.38$  cloud-screening rejection criterion. They were



presumably associated with prevailing extinction by coarse mode sea-salt aerosols transported from the Arctic Ocean, especially in the spring months.

**2.1.1.3. Measurements in Greenland.** Fig. 5 shows the results derived from the multi-year sets of sun-photometer measurements conducted at: (i) the Thule AERONET site, in the north-western corner of Greenland; (ii) the Summit PMOD/WRC site, located in the middle of the Central Greenland ice sheet; and (iii) Ittoqqortoormiit AERONET site, on the eastern coast of Greenland (see Table 1 for details on these sites).

The monthly mean  $\tau(0.50 \mu\text{m})$  values at Thule decreased slowly from about 0.10 in April–May to around 0.05 in June–September, with  $\sigma_\tau \sim 0.03$ , while  $\alpha$  was rather stable with monthly mean values ranging from 1.40 to 1.50 from March to September, with  $\sigma_\alpha \sim 0.3$ . The winter–spring  $\tau(0.50 \mu\text{m})$  RFH is characterised by a mean value of 0.093 and an asymmetric shape whose long-tailed, right-hand wing is influenced by the frequent occurrences of Arctic haze episodes. The summer–autumn RFH for  $\tau(0.50 \mu\text{m})$  was more symmetric, with mean and median values equal to 0.058 and 0.049, respectively, and values of the 25th and 75th percentiles relatively close to the median value, as can be seen in

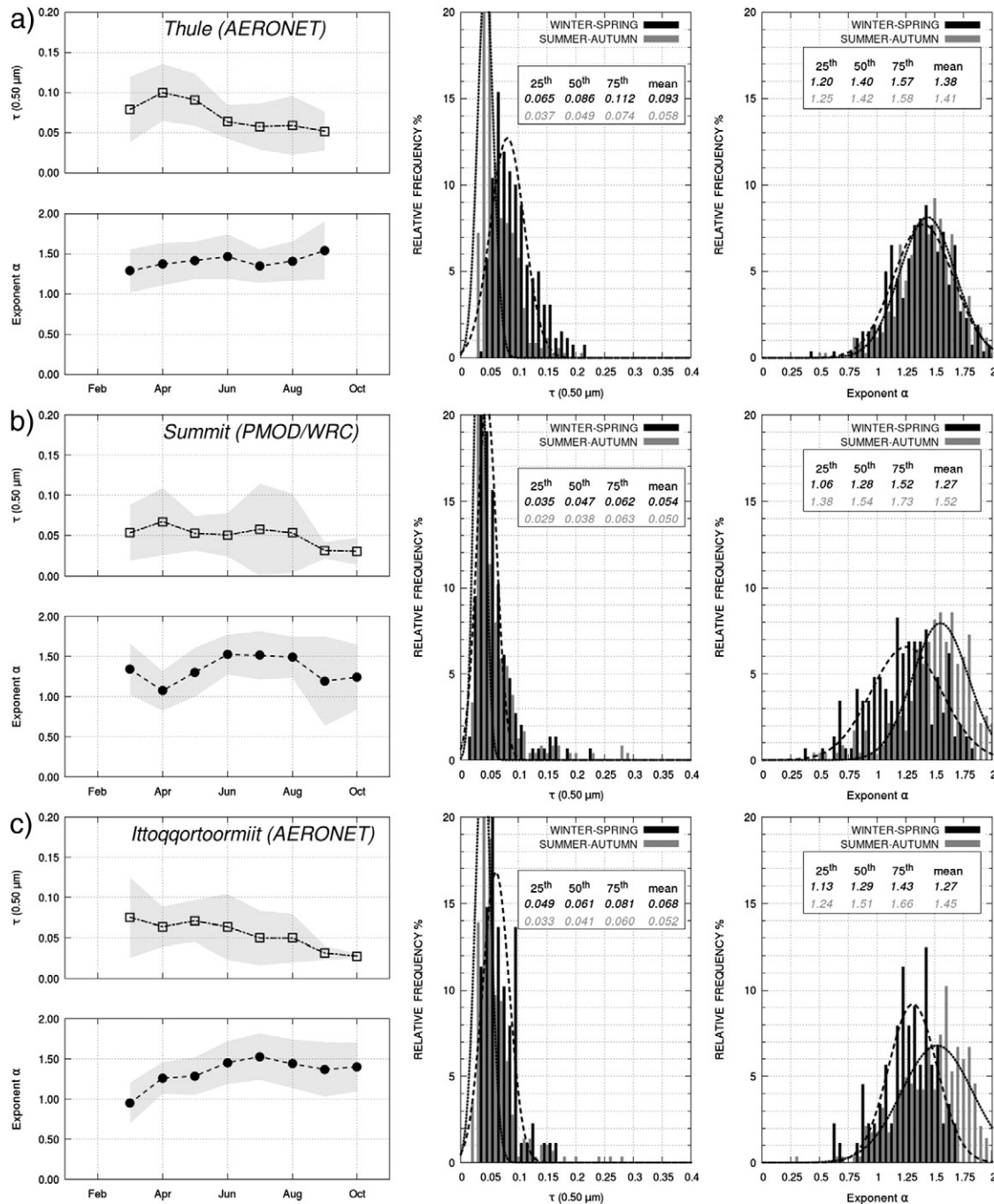


**Fig. 5.** As in Fig. 3, for the multi-year sun-photometer measurements of aerosol optical thickness  $\tau(0.50 \mu\text{m})$  and exponent  $\alpha$  conducted at: (a) Thule (North-western Greenland) by NASA/GSFC (USA) over the period from March 2007 to September 2012, using an AERONET Cimel CE-318 sun-photometer having the spectral characteristics reported in Table 1; (b) Summit (Central Greenland) by PMOD/WRC (Switzerland) from January 2001 to October 2011, using a PFR (No. N34) sun-photometer of the GAW-PFR network, having the spectral characteristics given in Table 1; and (c) Ittoqqortoormiit (Eastern Greenland) by NASA/GSFC (USA) over the period from May 2010 to October 2013, using an AERONET Cimel CE-318 sun-photometer having the spectral characteristics reported in Table 1.

Fig. 5. Very similar shapes of both seasonal RFHs for  $\alpha$  were obtained, with mean values of 1.38 in winter–spring and 1.41 in summer–autumn, and similar values of the main percentiles from winter–spring to summer–autumn, indicating no relevant seasonal changes in the aerosol size-distribution.

Rather stable monthly mean values of  $\tau(0.50 \mu\text{m})$  were obtained at the high-altitude Summit station, equal to  $0.05 \pm 0.03$  from March to August, and about  $0.03 \pm 0.01$  in September and October. Both seasonal RFHs of the daily mean  $\tau(0.50 \mu\text{m})$  values assumed very similar shapes, with mean values close to 0.05, and values of the main percentiles differing by no more than 0.01 from season to the other. Greater differences were determined between the two seasonal RFHs of  $\alpha$ , with mean values equal to 1.27 in winter–spring and 1.52 in summer–autumn, and the main percentiles differing by no more than 0.3. These aerosol optical characteristics indicate that Summit is representative of the Arctic free troposphere, influenced mainly by particulate transport from North America and Europe, and only weakly by Siberian aerosols (Hirdman et al., 2010).

The monthly mean values of  $\tau(0.50 \mu\text{m})$  at Ittoqqortoormiit showed similar seasonal variations to those at Thule, gradually decreasing from  $\sim 0.08$  in March to less than 0.04 in September–October, with  $\sigma_\tau = 0.05$  in spring, gradually decreasing in summer until reaching values of  $\sim 0.01$  in autumn. The monthly mean  $\alpha$  values increase from  $\sim 1.00$  in March to  $\sim 1.50$  in summer, and slowly decrease in September and October, varying around 1.40, with  $\sigma_\alpha = 0.2$  in March and close to 0.3 in the other months. The RFHs for  $\tau(0.50 \mu\text{m})$  did not vary largely from winter–spring to summer–autumn. The seasonal mean values were equal to 0.068 in winter–spring and 0.052 in summer–autumn, which were not considerably different from the median values in both seasons. They give a measure of the appreciable decrease in  $\tau(0.50 \mu\text{m})$  observed from winter–spring to summer–autumn. The seasonal RFHs for  $\alpha$  are more similar to those obtained at Summit than those of Thule. In fact, the winter–spring mean value of  $\alpha$  was equal to 1.28, and the summer–autumn value was equal to 1.45. These results suggest that the atmospheric content of fine mode particles increases considerably from winter to summer at Ittoqqortoormiit. Such variations are probably associated with the marked extinction effects produced by maritime accumulation/coarse mode particles in winter–spring and the predominant aerosol extinction effects produced by background continental particles mainly transported in summer–autumn from Europe and North America and containing in general significant loads of both anthropogenic and BFF particles.

The seasonal changes shown in Fig. 5 at the three Greenland sites can be mainly attributed to the variations in aerosol transport processes from anthropogenic/polluted regions or remote oceanic mid-latitude areas, and only rarely to Asian dust. Actually, the transport processes of anthropogenic soot aerosols are known to appreciably enhance  $\tau(\lambda)$ , yielding rather high values of  $\alpha$  in general (Tomasi et al., 2007; Stone et al., 2008). This may also occur in free-tropospheric layers, as observed during airborne measurements conducted at mid-altitudes over the Arctic Ocean (Stone et al., 2010).

**2.1.1.4. Measurements in Spitsbergen (Svalbard).** The results obtained at Ny-Ålesund, Barentsburg and Hornsund (Svalbard, Norway) from four different series of measurements are shown in Fig. 6, as conducted by AWI (Bremerhaven, Germany) and NILU (Kjeller, Norway) at Ny-Ålesund, IAO-SB-RAS (Tomsk, Russia) at Barentsburg, and the Institute of Geophysics (Warsaw University, PAS, Poland) in cooperation with NASA/GSFC (USA) at Hornsund (see Table 1).

The AWI monthly mean values of  $\tau(0.50 \mu\text{m})$  varied from 0.07 to 0.09 in winter–spring, and considerably decreased in summer–autumn from about 0.05 in June to 0.02 in October, with  $\sigma_\tau = 0.03$  on average. The NILU monthly mean values of  $\tau(0.50 \mu\text{m})$  were equal to  $\sim 0.10$  from March to May, and varied from 0.06 in June–July to less than 0.05 in August–September, with  $\sigma_\tau$  equal to 0.04 in spring and 0.03 in summer and autumn. The comparison between the AWI and NILU

results shows good agreement, although the NILU values were occasionally higher than those for AWI by no more than 10% on average in spring, such discrepancies probably arising from the slightly dissimilar measurement periods of 14 and 8 years, respectively. The AWI monthly mean values of  $\alpha$  increased from less than 1.30 in March to 1.50 in May, and slowly decreased in summer–autumn until reaching a value  $< 1.20$  in September and becoming nearly equal to 1.50 in October, with  $\sigma_\alpha = 0.30$  on average, while the NILU values increased slowly from 1.20 in March to 1.50 in June, and slowly decreased to  $\sim 1.30$  in September, with  $\sigma_\alpha = 0.20$  in all months. These discrepancies of no more than 15% are in general smaller than the monthly values of  $\sigma_\alpha$ . Therefore, it is not surprising that the RFHs found for the daily mean  $\tau(0.50 \mu\text{m})$  values derived from the AWI and NILU data-sets differ considerably from one season to another: (i) the AWI and NILU winter–spring mean values were equal to 0.082 and 0.089, respectively, with the main percentiles differing by no more than 0.007; and (ii) the AWI and NILU summer–autumn mean values of  $\tau(0.50 \mu\text{m})$  were equal to 0.052 and 0.059, respectively, with  $\sigma_\tau = 0.04$  on average, and having differences between the main percentiles no greater than 0.02. The AWI seasonal RFHs of  $\alpha$  yielded mean values of 1.32 in winter–spring and 1.28 in summer–autumn, while NILU RFHs gave mean values of 1.35 in winter–spring and 1.38 in summer–autumn. Comparable values of the three main percentiles of the AWI and NILU RFHs were also obtained, differing by less than 0.1 in winter–spring and less than 0.2 in summer–autumn. Therefore, the analysis of the AWI and NILU RFHs of  $\alpha$  showed: (i) more dispersed features of  $\alpha$  in winter–spring, presumably due to the larger variability of fine and coarse particle concentrations during the frequent Arctic haze episodes, and (ii) values of  $\alpha$  mainly varying from 1.00 to 1.60 in summer–autumn, due to the large variability of the fine particle mode atmospheric content (mainly related to BFFs smoke particle transport) with respect to that of accumulation/coarse mode particles (mainly of oceanic origin).

The data-sets of  $\tau(0.50 \mu\text{m})$  and  $\alpha$  derived from the Barentsburg IAO measurements consisted of a number of daily measurements smaller than 10% of that given by the AWI and NILU Ny-Ålesund measurements. The monthly mean  $\tau(0.50 \mu\text{m})$  values varied from 0.07 to 0.10, with  $\sigma_\tau = 0.02$  on average, and those of  $\alpha$  increased from  $\sim 0.90$  to 1.40 during summer, with  $\sigma_\alpha = 0.2$ . Therefore, these measurements differ only slightly from those measured at Ny-Ålesund over longer multi-year periods. The RFHs of the daily mean values of  $\tau(0.50 \mu\text{m})$  and  $\alpha$  were prepared only for the summer–autumn period, and were found to have a seasonal mean value of  $\tau(0.50 \mu\text{m}) = 0.078$ , with the main percentiles differing by less than 0.02 from the mean. These values are appreciably higher than those determined at Ny-Ålesund from the AWI and NILU data-sets. A summer–autumn mean value of  $\alpha = 1.29$  was obtained, with only slightly differing values of the main percentiles, and a considerably narrower RFH curve than those from the AWI and NILU data-sets measured at Ny-Ålesund.

The Ny-Ålesund results can also be compared in Fig. 6 with the AERONET measurements recorded at Hornsund. The Hornsund results are in close agreement with those of Ny-Ålesund, since the Hornsund monthly mean values of  $\tau(0.50 \mu\text{m})$  varied from 0.10 to no more than 0.12 in winter–spring, with  $\sigma_\tau = 0.04$  on average, and from 0.06 to 0.08 in summer–autumn, with  $\sigma_\tau < 0.03$ . The monthly mean values of  $\alpha$  were rather stable at Hornsund, mainly ranging from 1.20 to 1.50, and showing small differences with respect to the AWI and NILU results. The Hornsund RFHs of  $\tau(0.50 \mu\text{m})$  show that the winter–spring daily mean values were on average higher than those obtained in summer–autumn, by more than 0.03, with differences between the main seasonal percentiles no higher than 0.04. Small variations in  $\alpha < 0.07$  were observed from one season to the other between the seasonal mean values and the main percentiles. The long-tailed left-hand wings of the RFHs of  $\alpha$  determined during both seasons suggest that important extinction effects were presumably produced by the sea-salt accumulation/coarse mode particles during both seasons.

The seasonal variations in  $\tau(0.50 \mu\text{m})$  shown in Fig. 6 are mainly due to the different aerosol extinction features produced over the Svalbard region by Arctic haze, especially in spring, and by background aerosol in summer. They are in part associated with the significant seasonal mean decrease in the mean concentration of sulphate particles measured within the atmospheric ground-layer. For instance, on the basis of long-range routine measurements of particulate chemical composition conducted at the Zeppelin station ( $78^\circ 58' \text{ N}$ ,  $11^\circ 53' \text{ E}$ , 474 m a.m.s.l.), near Ny-Ålesund (Svalbard), Ström et al. (2003) estimated that the mean mass concentration of nss sulphate ions decreases on average with season, changing from about  $3 \times 10^{-1} \mu\text{g m}^{-3}$  in March–April (for frequent Arctic haze episodes) to around  $5 \times 10^{-2} \mu\text{g m}^{-3}$  in late summer (for background aerosol conditions). These features arise from the fact that the frequent Arctic haze episodes observed in winter and spring over the Svalbard region are mainly due to aerosol transport from the Eurasian area, rather than from North America or East Asia (Hirdman et al., 2010). The region north of  $70^\circ \text{ N}$  is isolated in summer from the mid-latitude aerosol sources, as demonstrated by Stohl et al. (2006), who analysed aerosol transport patterns into the Arctic. BFF smoke particles are episodically transported over the Svalbard region in summer, from the Siberian region and sometimes from North America (Tomasi et al., 2007; Stone et al., 2008). For instance, huge emissions from BFFs in North America reached Svalbard (Stohl et al., 2006) in July 2004, while agricultural fires in Eastern Europe caused very strong pollution levels in the Arctic during spring 2006 (Stohl et al., 2006; Lund Myhre et al., 2007).

**2.1.1.5. Measurements in Scandinavian and Siberian regions.** Fig. 7 shows the time-patterns of the monthly mean values of  $\tau(0.50 \mu\text{m})$  and  $\alpha$  and the winter–spring and summer–autumn RFHs of both parameters, derived from the sets of FMI/PFR and AERONET sun-photometer measurements carried out at Sodankylä (Northern Finland), and the set of AERONET measurements conducted at Tiksi in Northern-Central Siberia (Russia) (see Table 1).

The FMI/PFR monthly mean values of  $\tau(0.50 \mu\text{m})$  slowly increased from  $\sim 0.05$  in February to 0.08 in May, remained quite stable from June to August, then slowly decreased to 0.05 in September–October, with comparable values of  $\sigma_\tau$  ranging mainly from 0.04 to  $\pm 0.06$ , without showing clear variations from winter–spring to summer–autumn. The monthly mean values of  $\alpha$  increased from about 1.10 in February to over 1.50 in July, and then gradually decreased to 0.75 in November. Different time-patterns of the monthly mean values of  $\tau(0.50 \mu\text{m})$  and  $\alpha$  were obtained from the AERONET measurements conducted at Sodankylä over a shorter 7-year period, including only about a third of the daily PFR observations, and giving monthly mean values of  $\tau(0.50 \mu\text{m})$  varying from 0.05 to 0.09 in winter–spring, and from 0.06 to 0.11 in summer, which then decreased to less than 0.04 in September–October. The monthly mean values of  $\alpha$  varied from 1.20 to 1.40 in winter–spring, increasing to more than 1.70 in July and decreasing to nearly 1.00 in October.

To provide a more complete picture of the atmospheric turbidity features over Northern Scandinavia, the time-patterns of the PFR and AERONET monthly mean values of  $\tau(0.50 \mu\text{m})$  and  $\alpha$  obtained at Sodankylä are compared in Fig. 7 with those determined by Toledano et al. (2012) analysing the  $\tau(0.50 \mu\text{m})$  and  $\alpha$  data-sets collected at: (i) Kiruna ( $67^\circ 51' \text{ N}$ ,  $20^\circ 13' \text{ E}$ , 580 m a.m.s.l.) in Northern Sweden (270 km WNW from Sodankylä) using the GAW-PFR sun-photometer of the Swedish Meteorological and Hydrological Institute (SMHI) from 2007 to 2010 by, and (ii) Andenes/ALOMAR ( $69^\circ 18' \text{ N}$ ,  $16^\circ 01' \text{ E}$ , 380 m a.m.s.l.) in Northern Norway, using the AERONET/RIMA Cimel

CE-318 sun-photometer from 2002 to 2007. The Kiruna PFR results are compared in Fig. 7 with those recorded at Sodankylä. The Kiruna monthly mean values of  $\tau(0.50 \mu\text{m})$  were rather stable over the whole measurement period, with  $\sigma_\tau$  varying from 0.01 to 0.04, while the monthly mean values of  $\alpha$  increased from 1.10 in February to nearly 1.60 in July, and then decreased gradually to  $\sim 1.00$  in August and 1.20 in October, with values of  $\sigma_\alpha$  varying from 0.10 to 0.25. Thus, the Kiruna monthly mean values of  $\tau(0.50 \mu\text{m})$  closely agree with those measured at Sodankylä and only exhibit small differences between the August–October monthly mean values of  $\alpha$ .

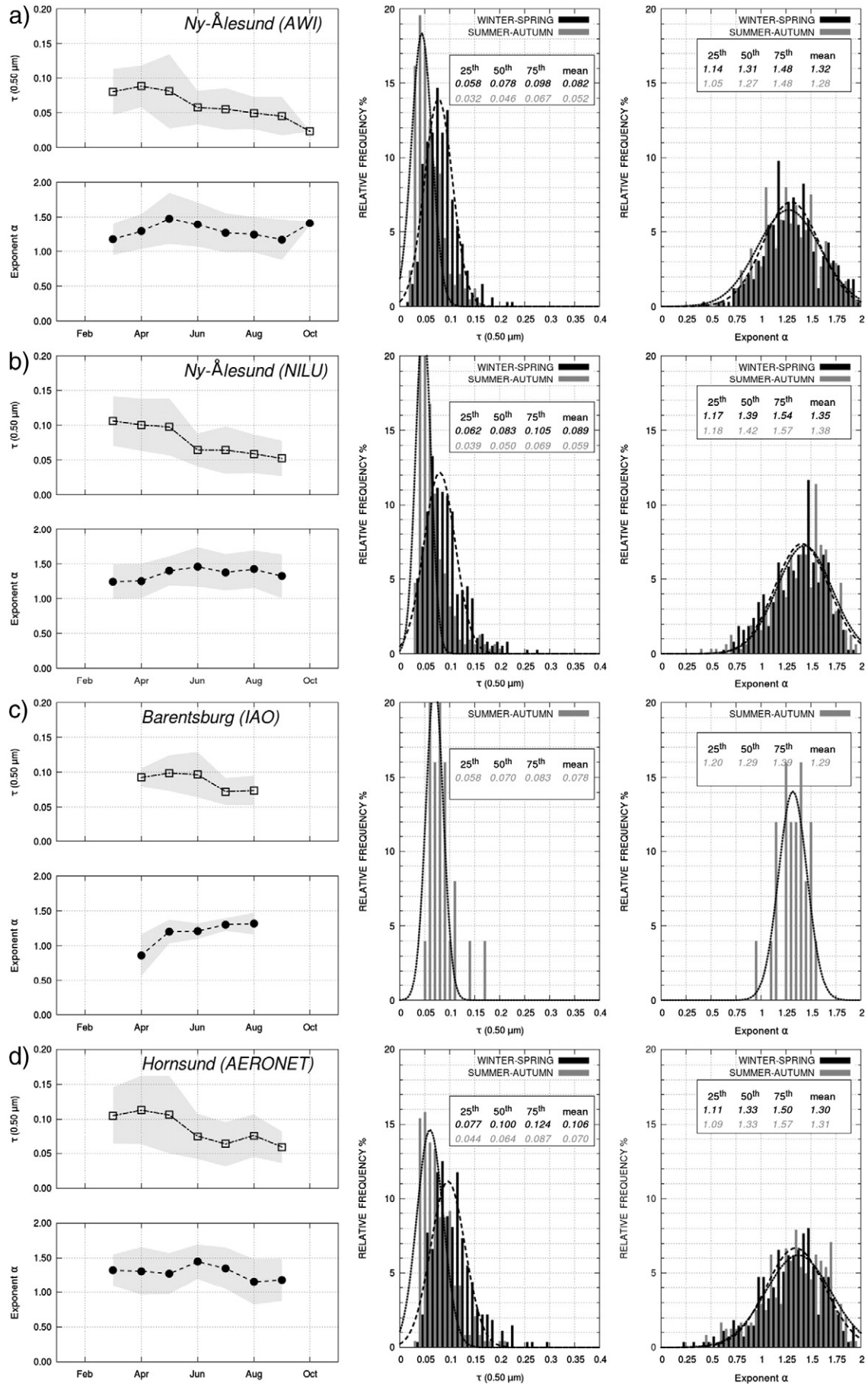
A similar comparison is also made in Fig. 7 between the AERONET/FMI results obtained at Sodankylä and the ALOMAR results derived from the AERONET/RIMA Cimel CE-318 sun-photometer measurements at Andenes, from 2002 to 2007. The ALOMAR monthly mean values of  $\tau(0.50 \mu\text{m})$  increased from about 0.04 in February to 0.13 in May, and then slowly decreased to around 0.11 in September–October, having values of  $\sigma_\tau$  mainly varying from 0.04 to 0.06. Therefore, the ALOMAR evaluations of  $\tau(0.50 \mu\text{m})$  were in general considerably higher than those measured at Sodankylä, with differences comparable to the standard deviations. The ALOMAR monthly mean values of  $\alpha$  varied at Andenes from about 0.85 to 1.05 in February–May, increased in the following months to  $\sim 1.30$ , and subsequently decreased in late summer and autumn to reach a value close to 1.00 in October, with  $\sigma_\alpha$  varying mainly from 0.20 in winter–spring to 0.40 in summer–autumn. These findings indicate that the ALOMAR monthly mean values of  $\alpha$  were considerably higher than the AERONET evaluations obtained at Sodankylä, by about 15% on average, presumably because of the more pronounced extinction effects by maritime particles.

The time-patterns of the monthly mean values of  $\tau(0.50 \mu\text{m})$  and  $\alpha$  shown in Fig. 7, as obtained by us at Sodankylä, and at Kiruna and Andenes by Toledano et al. (2012) differ appreciably from those typically observed at the other Arctic sites located at higher latitudes and shown in Figs. 3–6. The reason for such differences is that the air masses reaching Northern Scandinavia during the year originate from the Eurasian continent and mid-latitude Atlantic Ocean in 56% of cases, and from the Arctic Basin and Northern Atlantic Ocean in the remaining 44% (Aaltonen et al., 2006). Due to the alternation of polluted air masses from Eurasia with sea-salt particles from ocean areas, the monthly mean values of  $\tau(\lambda)$  were rather stable over the entire year, while the monthly mean values of  $\alpha$  were higher in early summer, when the Arctic Basin was the principal aerosol source. Because of the efficient transport processes taking place during the year from continental polluted or ocean areas, the FMI/PFR and AERONET Sodankylä RFHs of  $\tau(0.50 \mu\text{m})$  did not exhibit significant differences between the seasonal mean values and the main percentiles defined in winter–spring and summer–autumn. These had monthly mean values of around 0.08 and 0.07 in winter–spring, respectively, with the main percentiles differing by no more than 0.01, and summer–autumn monthly mean values close to 0.07 on average, with differences of about 0.01 between the main percentiles. The FMI/PFR and AERONET Sodankylä monthly mean values of  $\alpha$  decreased by 0.10–0.20 on average, from winter–spring to summer–autumn. Clearer discrepancies over both seasonal periods were found, with FMI mean values of about 1.32 and 1.52 in winter–spring and summer–autumn, respectively, and AERONET mean values equal to 1.23 and 1.44 in the same two seasons, providing similar values of the main seasonal percentiles.

A comparison between the winter–spring and summer–autumn estimates of  $\tau(0.50 \mu\text{m})$  and  $\alpha$  was not made at Tiksi, since AERONET sun-photometer measurements have been routinely conducted at this remote Siberian site only over the May–October period. The monthly

**Fig. 6.** As in Fig. 3, for the sun-photometer measurements of aerosol optical thickness  $\tau(0.50 \mu\text{m})$  and exponent  $\alpha$  conducted on Spitsbergen Island (Svalbard, Norway) at: (a) Ny-Ålesund by AWI (Bremerhaven, Germany) from April 2000 to September 2013, using the sun- and star-photometers listed in Table 1; (b) Ny-Ålesund by NILU (Kjeller, Norway) from April 2002 to September 2004 and from March 2006 to September 2013, using a PFR (No. N18) sun-photometer of the GAW network; (c) Barentsburg by IAO-SB-RAS (Tomsk, Russia) in the April–August months of 2011 and 2012, using the SPM portable sun-photometer having the characteristics reported in Table 1, and (d) Hornsund by NASA/GSFC (USA) in cooperation with the Warsaw University (PAS, Poland from April 2005 to August 2013), using an AERONET Cimel CE-318 sun-photometer having the characteristics reported in Table 1.





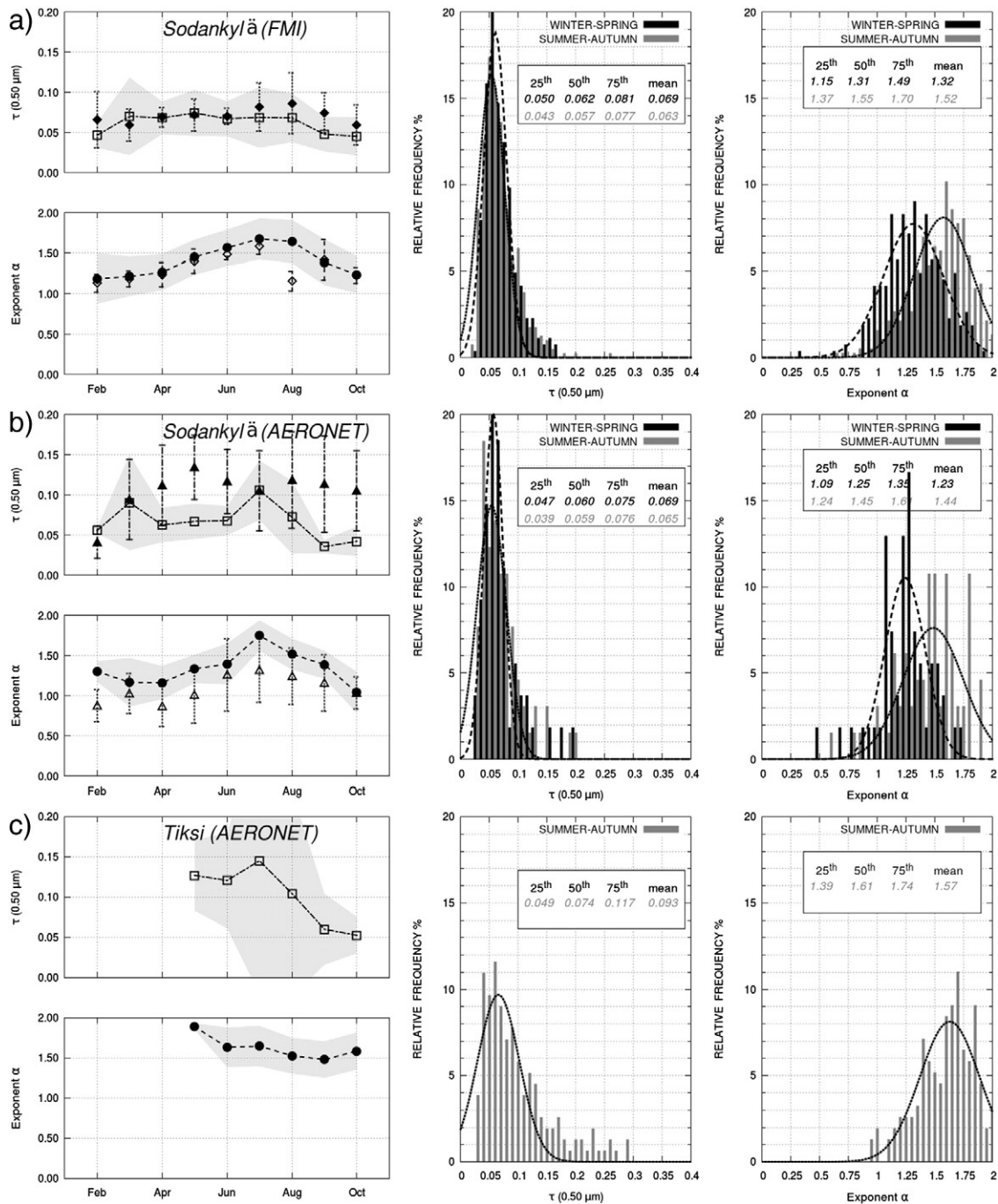


**Fig. 7.** As in Fig. 3, for the sun-photometer measurements of aerosol optical thickness  $\tau(0.50 \mu\text{m})$  and exponent  $\alpha$  conducted at: (a) Sodankylä (Northern Finland) by FMI (Helsinki, Finland) in the winter–spring and summer–autumn periods from late May 2004 to March 2013, using a PFR (No. N32) sun-photometer having the characteristics reported in Table 1, (b) Sodankylä by NASA/GSFC (USA) in cooperation with FMI (Helsinki, Finland) from February 2007 to November 2013, using an AERONET Cimel CE-318 sun-photometer having the characteristics reported in Table 1; and (c) Tiksi (North-central Siberia, Russia) by NASA/GSFC (USA) in the summer–autumn months (June–October) of 2010, 2011 and 2012, using an AERONET Cimel CE-318 sun-photometer having the characteristics given in Table 1. In the first graphs, the time-patterns of the monthly mean values of  $\tau(0.50 \mu\text{m})$  and  $\alpha$  (solid and open diamonds, respectively) estimated by Toledano et al. (2012) at Kiruna from PFR measurements conducted over the 2007–2010 period are shown with their standard deviations (vertical bars) for comparison with the FMI results found at Sodankylä. The time-patterns of the monthly mean values of  $\tau(0.50 \mu\text{m})$  and  $\alpha$  (solid and open triangles, respectively) estimated by Toledano et al. (2012) at Kiruna from the Cimel CE-318 measurements conducted from 2002 to 2007 are shown in the second graph for comparison with those derived from the AERONET measurements carried out at Sodankylä.

mean values of  $\tau(0.50 \mu\text{m})$  exhibit a clear increase from  $\sim 0.13$  in May to 0.16 in July, with large average values of  $\sigma_\tau = 0.14$ , followed by a marked decrease in the subsequent months to about  $0.05 \pm 0.03$  in October. Such large variations in  $\tau(0.50 \mu\text{m})$  were associated with a slow decrease in the monthly mean values of  $\alpha$  from 1.9 in May to  $\sim 1.5$  in September, for which  $\sigma_\alpha \leq 0.2$ . The rather high values of  $\tau(0.50 \mu\text{m})$  and  $\alpha$  determined in summer were probably due to the

frequent BFF smoke transport episodes from the inner regions of Siberia. In fact, the summer–autumn RFH of  $\tau(0.50 \mu\text{m})$  exhibits a mean value close to 0.09 and a value of the 75th percentile equal to 0.12, which are both appreciably higher than those measured at Sodankylä in summer. The RFH of  $\alpha$  yields a mean value of 1.57, and shows a long-tailed left-hand wing with 25th percentile of 1.39, and a long-tailed right-hand wing with 75th percentile of 1.74. This rather high value is

probably associated with small fine particles generated by combustion processes, which dominate extinction effects.

In summary, the Arctic results provide evidence of the seasonality of  $\tau(0.50 \mu\text{m})$  and  $\alpha$ . A scatter plot of the median values of  $\alpha$  versus those of  $\tau(0.50 \mu\text{m})$  is shown in Fig. 8a, separately for the winter–spring and summer–autumn seasonal periods. Fig. 8a shows that the median values of  $\alpha$  vary from 1.10 to 1.70 over the whole year, with: (i) winter–spring median values of  $\tau(0.50 \mu\text{m})$  ranging from 1.20 to 1.50 over the 0.04–0.12 range, and (ii) summer–autumn median  $\tau(0.50 \mu\text{m})$  values all smaller than 0.08 and mainly ranging from 1.30 to 1.70. These features suggest that appreciable differences characterise aerosol extinction in: (a) winter–spring, when the median values of  $\tau(0.50 \mu\text{m})$  vary greatly from one Arctic site to another. This results from their dependency on the importance of particulate transport from the most densely populated mid-latitude regions towards the Arctic, which is particularly strong in late winter and early spring; and (b) summer, when the background aerosol composition varies from

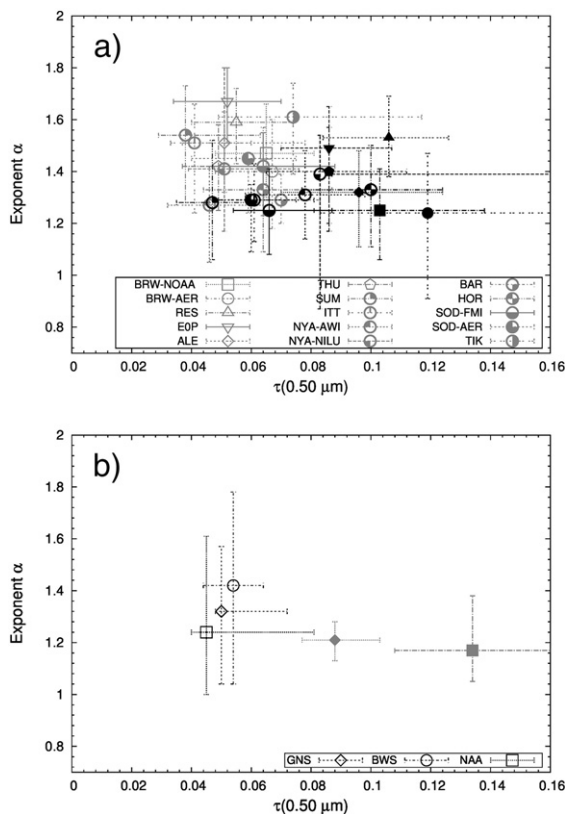


**Fig. 8.** Upper part (a): Scatter plot of the seasonal median values of the Ångström exponent  $\alpha$  versus the corresponding seasonal median values of aerosol optical thickness  $\tau(0.50 \mu\text{m})$  determined from the sun-photometer measurements listed in Table 1. Acronym key: Barrow (BRW-NOAA for the GMD/NOAA measurements, and BRW-AER for the NASA/GSFC AERONET measurements), Resolute Bay (RES), Eureka-OPAL (EOP), Alert (ALE) Thule (THU), Summit (SUM), Ittoqqortoormiit (ITT), Ny-Ålesund (NYA-AWI and NYA-NILU, for the AWI and NILU measurements, respectively), Barentsburg (BAR), Hornsund (HOR), Sodankylä (SOD-PFR and SOD-AER, for the PFR and AERONET measurements, respectively) and Tiksi (TIK). The median values are represented using grey-solid and grey-and-white open symbols to represent the summer–autumn results (as shown in the legend) and solid or black-and-white open symbols to represent the winter–spring results, showing the background aerosol and Arctic haze optical characteristics, respectively. The 25th and 75th percentiles are used to define the limits of the vertical and horizontal dashed bars. Part (b), as in the upper part (a), for the winter–spring (grey symbols) and summer–autumn (open symbols) median values of  $\alpha$  plotted versus the corresponding median values of  $\tau(0.50 \mu\text{m})$ , as obtained from the seasonal sets of ship-borne sun-photometer measurements collected over the Arctic Ocean sectors: (i) GNS (Greenland Sea and Norwegian Sea) (diamonds), (ii) BWS (Barents Sea and West Siberian Sea) (circles), and (iii) NAA (North American Arctic ocean, including the East Chukchi Sea, the Bering Strait, the Beaufort Sea and the Amundsen Gulf) (squares).

one site to another, as a result of different extinction characteristics of fine and coarse mode particles transported from remote regions.

## 2.1.2. Measurements in Antarctica

Ground-based sun-photometer measurements of aerosol optical parameters have been conducted in Antarctica during the short austral summer period. In the present study, nine multi-year sets of measurements made since 2000 have been analysed (see Table 2), collected at six coastal sites (Marambio, Neumayer, Novolazarevskaya, Mirny, Syowa, and Mario Zucchelli), a mid-altitude station (Troll) and two high-altitude sites (Dome Concordia and South Pole).

**2.1.2.1. Measurements at coastal and mid-altitude sites.** The results obtained from the sun-photometer measurements carried out at Marambio, Neumayer and Troll are presented in Fig. 9. The Marambio measurements were conducted from September to April, and provided monthly mean values of  $\tau(0.50 \mu\text{m})$  varying from  $\sim 0.03$  in January to 0.06 in March (with  $\sigma_\tau$  varying from 0.02 to 0.04) and  $\alpha$  ranging from 0.50 in March to 1.50 in November–January (with  $\sigma_\alpha = 0.50$  on average). The austral summer RFHs exhibit regular features with mean values of  $\tau(0.50 \mu\text{m}) = 0.038$  and  $\alpha = 1.20$ , probably due to sea-salt particles, which dominate extinction. The Neumayer measurements were conducted over the September–April period, showing rather stable time-patterns of the monthly mean values of  $\tau(0.50 \mu\text{m})$ , ranging from 0.04 to 0.06 (with  $\sigma_\tau = 0.03$  on average) and associated with very stable values of  $\alpha$  varying from 0.50 to 1.00 (with  $\sigma_\alpha = 0.3$  on average), which indicate that aerosols are mostly of oceanic origin. The RFHs of both optical parameters are similar to those determined at Marambio, showing mean values of  $\tau(0.50 \mu\text{m}) = 0.041$  and  $\alpha = 0.82$ , confirming that these stable extinction features are mainly produced by sea-salt particles. The time-patterns of the monthly mean values of  $\tau(0.50 \mu\text{m})$  and  $\alpha$  measured at Troll, about 235 km from the Atlantic Ocean coast in the Queen Maud Land, were also quite stable from September to April, yielding values of  $\tau(0.50 \mu\text{m})$  varying from  $\sim 0.02$  to 0.03 (with  $\sigma_\tau < 0.005$ ), and values of  $\alpha$  slowly increasing from 1.25 in September to  $\sim 1.50$  in January, and then decreasing to 1.00 in April. The RFH of  $\tau(0.50 \mu\text{m})$  exhibits nearly symmetrical features with little dispersion, with a mean value of 0.023, and 25th and 75th percentiles equal to 0.019 and 0.026, respectively, while the RFH of  $\alpha$  was also quite symmetrical over the 0.60–2.10 range, with a mean value of 1.42 and 25th and 75th percentiles differing by less than 0.4 one from the other. These estimates of  $\tau(0.50 \mu\text{m})$  and  $\alpha$  differ appreciably from those obtained at Marambio and Neumayer, showing that the aerosol extinction features are only in part produced by maritime aerosols at this mid-altitude site, and in part by fine mode particles, such as nss sulphate aerosols.

Fig. 10 shows the results obtained from the measurements conducted at Novolazarevskaya (Queen Maud Land) and Mirny (on the Davis Sea coast), using various sun-photometer models during different years, as reported in Table 2. The monthly mean values of  $\tau(0.50 \mu\text{m})$  obtained at Novolazarevskaya were very close to  $0.02 \pm 0.01$  over the whole period, while  $\alpha$  varied from about 0.80 in November to 1.10 in January, with  $\sigma_\alpha$  equal to 0.10 in the first two months and 0.50 in January and February. The RFH of  $\tau(0.50 \mu\text{m})$  exhibited a leptokurtic curve, with mean value close to 0.02, while a more dispersed distribution curve was shown by the RFH of  $\alpha$ , with the mean value close to unity, and 25th and 75th percentiles differing by less than 0.20 from it. The monthly mean values of  $\tau(0.50 \mu\text{m})$  determined at Mirny varied from 0.02 to 0.03 (with  $\sigma_\tau = 0.01$ ), and those of  $\alpha$  from 1.50 to 2.00 in September–January, which then slowly decreased to  $\sim 1.20$  in April. The RFH of  $\tau(0.50 \mu\text{m})$  exhibited features which had a nearly symmetrical peak, with a mean value of 0.025, only slightly differing from that obtained at Novolazarevskaya, while the RFH of  $\alpha$  was found to be dispersed and platykurtic, having a mean value of 1.60, and 25th and 75th percentiles differing by more than 0.40 from the mean value. Therefore, it can be concluded that the aerosol extinction features



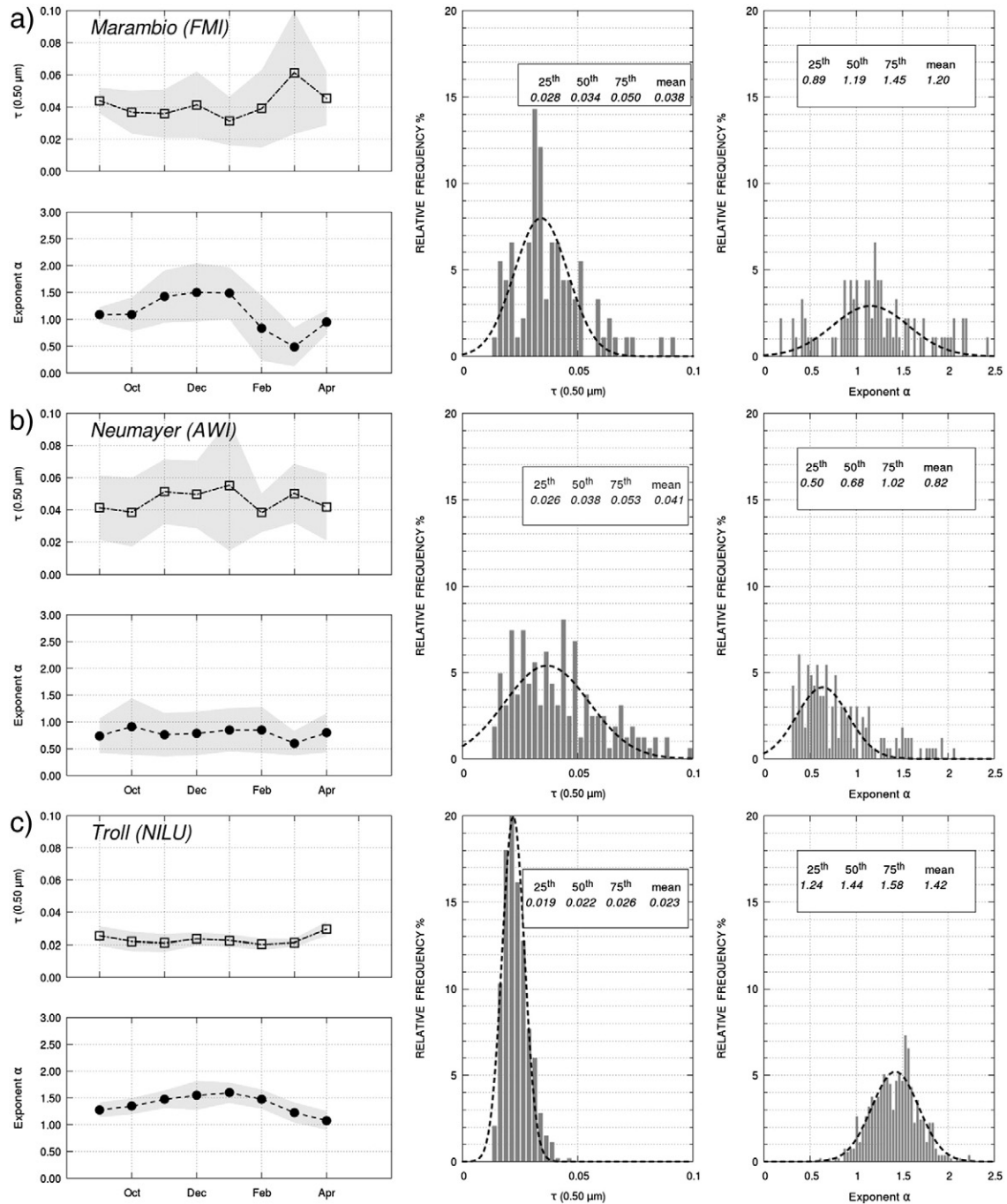


**Fig. 9.** As in Fig. 3, for sun-photometer measurements of aerosol optical thickness  $\tau(0.50 \mu\text{m})$  and exponent  $\alpha$  conducted during the September–April period at: (a) Marambio in the Seymour–Marambio Island (Antarctic Peninsula) by FMI (Helsinki, Finland), using a PFR (No. N29) sun-photometer from August 2011 to March 2013; (b) Neumayer on the Akta Bay (Weddel Sea coast) by AWI (Bremerhaven, Germany), using the sun-photometers SP1A and SP2H, and the star-photometer STAR01 listed in Table 2 from September 2000 to April 2007; and (c) Troll located at Jutulssessen (in the Queen Maud Land, 235 km from the coast, at 1309 m a.m.s.l.) by NILU (Kjeller, Norway), alternately using two PFR (Nos. N40 and N42) sun-photometers from January 2007 to April 2013.

shown in Fig. 10 are predominantly produced by sea-salt particles generated by winds over the ocean, yielding values of  $\alpha$  mainly ranging from 0.50 to 1.30.

The results derived from the measurements conducted at Syowa and Mario Zucchelli are shown in Fig. 11, as obtained using various sun-photometer models over the different periods reported in Table 2. The monthly mean values of  $\tau(0.50 \mu\text{m})$  varied from less than 0.02 to ~0.04 over the September–April period (with  $\sigma_\tau < 0.03$ ), while the monthly mean values of  $\alpha$  were also very stable, and described a large maximum of around 1.30 in December, with minima of ~1.00 in September and ~0.90 in April. The RFH of  $\tau(0.50 \mu\text{m})$  assumed a

mesokurtic shape, skewed to the right, with the mean value close to 0.02, while the RFH of  $\alpha$  exhibited mesokurtic and symmetrical features, arising from sea-salt particles, which caused the predominant extinction. The ISAC–CNR measurements conducted at Mario Zucchelli provided the time-patterns of the monthly mean values of  $\tau(0.50 \mu\text{m})$  shown in Fig. 11, which were close to 0.02 in November and December (with  $\sigma_\tau = 0.01$ ) and then increased to ~0.04 in January and February (with  $\sigma_\tau = 0.02$ ), while the monthly mean values of  $\alpha$  were stable and very close to 1.00 from November to January, and equal to ~0.80 in February (with  $\sigma_\alpha$  not exceeding 0.30). The RFHs of  $\tau(0.50 \mu\text{m})$  and  $\alpha$  were found to exhibit more dispersed features than those determined at Syowa and

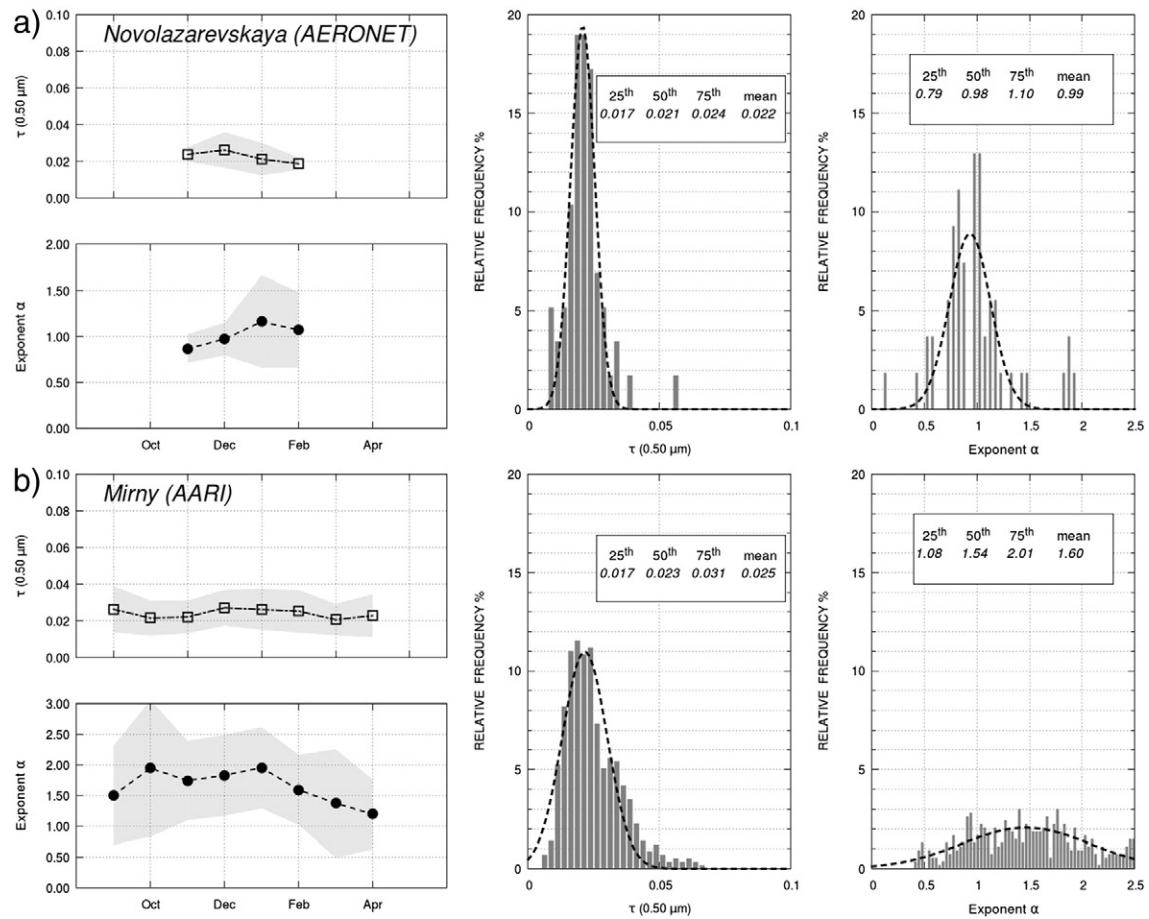


**Fig. 10.** As in Fig. 3, for sun-photometer measurements of aerosol optical thickness  $\tau(0.50 \mu\text{m})$  and exponent  $\alpha$  conducted at the Antarctic sites of: (a) Novolazarevskaya in the Schirmaker Oasis (Quenn Maud Land), 75 km from the coast, by AARI (St. Petersburg, Russia), using a hand-held Microtops calibrated at GSFC (USA) over the periods from December 2008 to February 2009 and from November 2009 to February 2010, and obtaining Level 1.5 cloud-screened data; and (b) Mirny on the Davis Sea coast by AARI (St. Petersburg, Russia), using the AARI, SPM and Microtops sun-photometers, having the spectral characteristics given in Table 2, over the period from March 2000 to October 2013.

both Russian stations, giving mean values equal to 0.04 and 0.96, respectively. However, they clearly indicate that aerosol extinction is mainly due to sea-salt particles at this coastal site, yielding values of  $\alpha$  ranging in general from 0.50 to 1.30.

#### 2.1.2.2. Measurements at the high-altitude sites on the Antarctic Plateau.

The results obtained analysing the sun-photometer measurements conducted since 2000 at the Dome Concordia and South Pole high-altitude sites are shown in Fig. 12. The measurements were conducted by five groups using different instruments over distinct periods, as reported in Table 2. Due to the background transport of aerosols from very remote sources and the predominant role of subsidence processes on the aerosol load, the time-patterns of the monthly mean values of  $\tau(0.50 \mu\text{m})$  determined at Dome Concordia with different sun-photometers were found to be very stable, mainly ranging from 0.02 to 0.04 (with  $\sigma_\tau$  evaluated to be  $\leq 0.01$ ) in September–April. The corresponding monthly mean values of  $\alpha$  mainly varied from 1.00 to 2.00, with  $\sigma_\alpha = 0.20$  on average. The RFH of  $\tau(0.50 \mu\text{m})$  exhibited a well-marked leptokurtic shape, with a mean value close to 0.02, while the RFH of  $\alpha$  showed dispersed features over the 0.5–2.2 range, with a mean value close to 1.40, and 25th and 75th percentiles equal to about 1.0 and 1.80, respectively.

The South Pole multi-year measurements conducted by GMD/NOAA at the Amundsen-Scott base were found to provide very stable time-patterns of the monthly mean values of  $\tau(0.50 \mu\text{m})$ , mainly ranging from September to March from  $\sim 0.02$  to 0.04 (with  $\sigma_\tau = 0.01$  on average), and monthly mean values of  $\alpha$  varying from 1.00 to 2.00, with the highest values in October and November (with  $\sigma_\alpha = 0.10$  on

average). The AERONET monthly mean values of  $\tau(0.50 \mu\text{m})$  were found to increase from about 0.01 to 0.02 over the November–February period, with  $\sigma_\tau = 0.01$  on average, the uncertainty of these measurements being primarily due to both calibration (estimated by Eck et al. (1999) to be of  $\sim 0.01$  in the visible), and forward scattered light entering the instrument (Sinyuk et al., 2012). Very stable monthly mean values of  $\alpha \sim 1.00$  were correspondingly found, with  $\sigma_\alpha = 0.50$  on average. Both RFHs of  $\tau(0.50 \mu\text{m})$  derived from the GMD/NOAA and AERONET measurements assumed very narrow and “peaked” curves, with mean values of around 0.02, which appeared to be slightly skewed to the right. The corresponding RFHs of  $\alpha$  presented dispersed features over the 0.50–2.00 range, with mean values of 1.54 and 1.06. Although such clearly dispersed results suggest the presence of an important fraction of large-size particles, it is important to take into account that a predominant particulate mass fraction of around 66% was estimated to consist of nss sulphates at South Pole, with lower concentrations of nitrates and sea-salt particles (Arimoto et al., 2004; Tomasi et al. 2012), mainly associated with the background transport of aerosols from very remote sources and the strong effects exerted by subsidence processes. A few cases showing values of  $\alpha < 0.50$  were probably caused by consistent loads of diamond dust ice-crystals within the lower planetary boundary layer (hereinafter referred to as PBL), due to wind mobilisation.

The covariance of the median values of  $\tau(0.50 \mu\text{m})$  and  $\alpha$  obtained at the nine Antarctic sun-photometer stations is shown in Fig. 13a. There are two clusters: (i) the first at coastal sites, where the median values of  $\tau(0.50 \mu\text{m})$  were in general considerably higher (at least by a factor two) than those found at the high-altitude Antarctic sites, and the

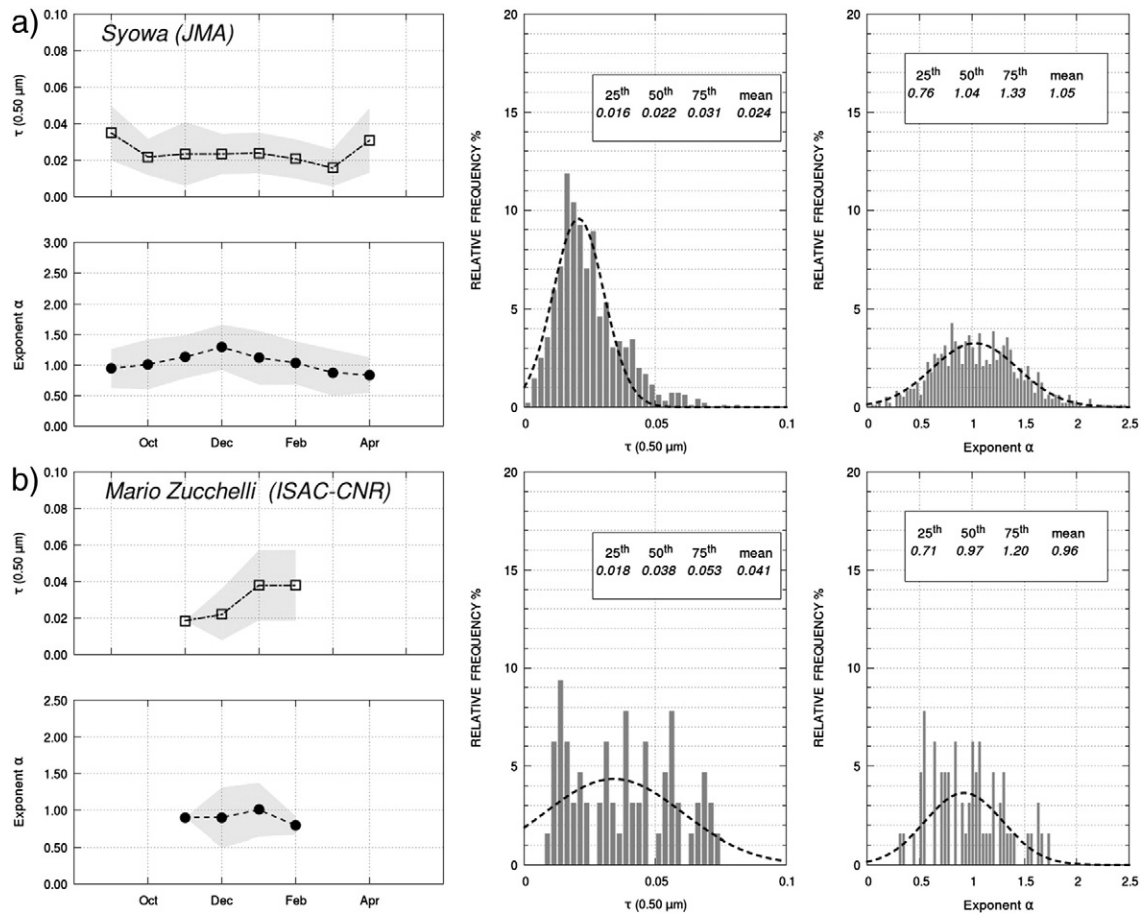


**Fig. 11.** As in Fig. 3, for sun-photometer measurements of aerosol optical thickness  $\tau(0.50 \mu\text{m})$  and exponent  $\alpha$  conducted at the Antarctic sites of: (a) Syowa (East Ongul Island, Lützow-Holm Bay) over the period from January 2000 to December 2011 by the Office of Antarctic Observation (Japan Meteorological Agency, Tokyo, Japan), using the EKO MS-110 sun-photometer, having the spectral characteristics given in Table 2; and (b) Mario Zucchelli on the Terra Nova Bay (Ross Sea, Victoria Land) during the austral summer periods of 2001/2002 and 2005/2006 by ISAC-CNR (Bologna, Italy), using the PREDE POM-01 L and the ASP-15WL sun-photometers, having the spectral characteristics given in Table 2.

median values of  $\alpha$  are in general smaller than 1.20, and (ii) the second cluster, with lower median values of  $\tau(0.50 \mu\text{m})$  and median values of  $\alpha > 1.40$ , for which aerosol extinction is predominantly due to sea-salt coarse particles. It is interesting to note that lower median values of  $\tau(0.50 \mu\text{m})$  associated with higher values of  $\alpha$  were observed at the coastal sites of Mirny and Marambio, probably because of aeolian fine particles, which dominated extinction effects when compared to sea-salt particles. The median values of  $\tau(0.50 \mu\text{m})$  and  $\alpha$  determined at the Troll mid-altitude station indicate that the extinction effects exhibit intermediate features at this non-coastal site. This can probably be attributed in part to sea-salt aerosol and in part to background nss sulphate aerosol transported over large distances, which themselves contribute towards an appreciable enhancement in  $\alpha$ . As can be seen in Fig. 13a, the weak median values of  $\tau(0.50 \mu\text{m})$  and relatively strong median values of  $\alpha$  at Dome Concordia and South Pole (the latter being partially obscured by the DMC-OPAR symbol) show that atmospheric aerosol extinction is rather weak above the Antarctic Plateau and mainly produced by fine particles consisting of nss sulphates. The lower extremes of the  $\alpha$  error bars and the low  $\alpha$  value of the AERONET South Pole point are likely due to near-surface diamond dust layers that are observed on windy, cloud-free days at these sites.

### 3. Ship-borne measurements

A large number of ship-borne measurements of the main columnar aerosol radiative parameters  $\tau(\lambda)$  and  $\alpha$  were made over the Arctic and Antarctic oceanic regions during the past 10 years. The cruises were conducted by research groups and institutions from different

countries, using hand-held Microtops II sun-photometers calibrated at the NASA/GSFC calibration facility. As can be seen in Fig. 2, large areas of the polar oceans were studied during these cruises, yielding an exhaustive picture of aerosol optical characteristics in these high-latitude remote regions. These ship-borne sun-photometer measurements were conducted as a part of the activities promoted and developed in the framework of the Maritime Aerosol Network (MAN), which is a component of the AERONET network (see [http://aeronet.gsfc.nasa.gov/new\\_web/maritime\\_aerosol\\_network.html](http://aeronet.gsfc.nasa.gov/new_web/maritime_aerosol_network.html)). The measurements of  $\tau(\lambda)$  were carried out at visible and near-infrared wavelengths. Arctic Ocean cruises are listed in Table 3, while those taken in the oceanic regions around Antarctica are listed in Table 4. The hand-held Microtops II sun-photometers are equipped with five narrow-band interference filters with peak wavelengths of 0.340 (or 0.380), 0.440, 0.675, 0.870 and 0.936  $\mu\text{m}$  for most cruises, or 0.440, 0.500, 0.675, 0.870 and 0.936  $\mu\text{m}$  in other cruises, as reported in Tables 3 and 4. The first four filters of each spectral set were used to measure the spectral values of  $\tau(\lambda)$  and determine the best-fit value of exponent  $\alpha$  over the wavelength range from 0.440 to 0.870  $\mu\text{m}$ , while the measurements taken at 0.936  $\mu\text{m}$  were combined with those made within the nearby channel centred at 0.870  $\mu\text{m}$  to evaluate precipitable water (Smirnov et al., 2009). Among the data-sets available at the MAN website, we only selected measurements conducted since 2006 at latitudes higher than 67° N in the Arctic and within ocean areas far by no more than 1000 km from the Antarctic coasts. In addition, the measurement sets obtained by Tomasi et al. (2007) during the RV Oceania cruises made in the summer months of 2003 and 2006 were included in the present analysis.



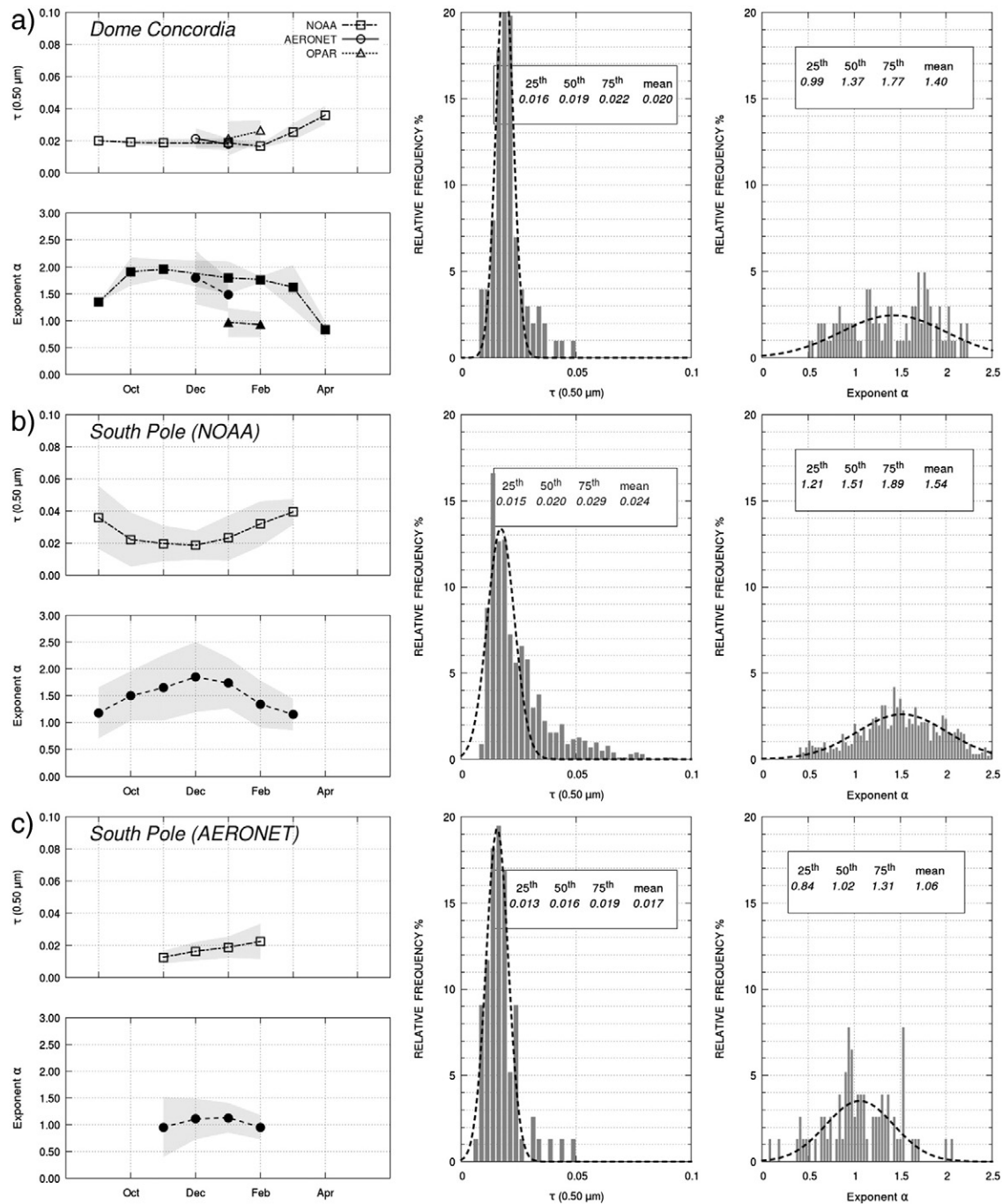


**Fig. 12.** Upper part: as in Fig. 3, for sun-photometer measurements of aerosol optical thickness  $\tau(0.50 \mu\text{m})$  and exponent  $\alpha$  conducted at: (a) the high-altitude site of Dome Concordia (DomeC), on the Eastern Antarctic Plateau, over the period from September to April, by (i) GMD/NOAA (Boulder, Colorado, USA) from January to November 2010, using a Carter Scott SP02 sun-photometer (squares); (ii) NASA/GSFC (USA) in cooperation with LGGE/CNRS (Grenoble, France) in January and December of 2003, and in January 2004, using an AERONET Cimel CE-318 sun-photometer having the spectral characteristics reported in Table 2 (circles); and (iii) OPAR Institute (University of Réunion, St. Denis, France) in January of 2010, 2011 and 2012, using a hand-held Microtops II sun-photometer calibrated at GSFC (USA), obtaining Level 1.5 cloud-screened data (triangles). Lower part: as in Fig. 3, for sun-photometer measurements of aerosol optical thickness  $\tau(0.50 \mu\text{m})$  and exponent  $\alpha$  conducted at the high-altitude site of South Pole (SPO) by (i) GMD/NOAA (Boulder, Colorado, USA) in cooperation with Carter Scott SP02 sun-photometer in the September–March period from November 2001 to March 2012; and (ii) NASA/GSFC (USA) in cooperation with GMD/NOAA (Boulder, Colorado, USA) using an AERONET Cimel CE-318 sun-photometer having the spectral characteristics reported in Table 2 in the November–February period from November 2007 to December 2012.

### 3.1. Aerosol measurements in the Arctic Ocean

Fourteen Arctic Ocean cruises were selected for this study, as summarised in Table 3. The data-set collected during the cruise of RV Polarstern (Alfred Wegener Institute (AWI), Bremerhaven, Germany) in August–September 2009 was not examined to evaluate the background tropospheric aerosol extinction features, because these measurements were found to be strongly affected by the extinction of

stratospheric volcanic aerosols generated by the Sarychev eruption in July–October 2009. No evidence of Sarychev volcanic particle extinction at stratospheric levels was found in CALIPSO (Cloud-Aerosol Lidar and Infrared Pathfinder Satellite Observations) data recorded over the Beaufort Sea (O'Neill et al., 2012) during the CCGS Amundsen cruise of August 2009. Therefore, this set of measurements was used to calculate the extinction effects associated in August 2009 with the BFF smoke particles transported from the North American forests over the Arctic

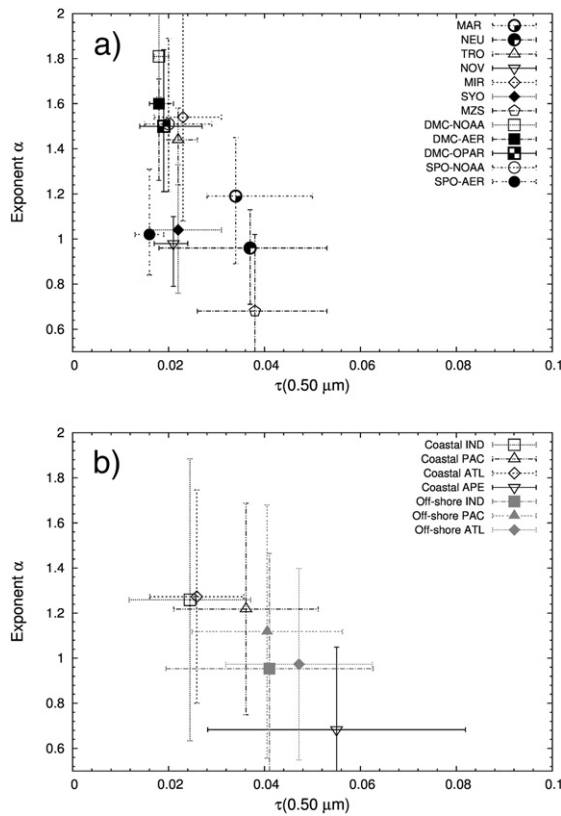


**Fig. 13.** Part (a): as in Fig. 8, but for the sun-photometer measurements listed in Table 2. Acronym key: Marambio (MAR), Neumayer (NEU), Troll (TRO), Novolazarevskaya (NOV), Mirny (MIR), Syowa (SYO), Mario Zucchelli (MZS), Dome Concordia (DMC-NOAA, DMC-AER, and DMC-OPAR, for the measurement sets collected by GMD/NOAA, AERONET and OPAR groups, respectively (see Table 4)) and South Pole (SPO-NOAA and SPO-AER, for the measurement sets collected by GMD/NOAA and AERONET groups, respectively). Part (b): as in part (a), for the Microtops sun-photometer measurements performed in Antarctic coastal (open symbols) and off-shore areas (solid symbols) during the cruises conducted in the four following oceanic sectors: (i) IND (Southern Indian Ocean, squares), (ii) PAC (Southern Pacific Ocean, upward triangles), (iii) ATL (Southern Atlantic Ocean, diamonds), and (iv) APE (Antarctic Peninsula, downward triangles).

Ocean. In order to study the aerosol extinction features of the Arctic Ocean, the 14 Microtops sun-photometer data-sets collected during the above-selected MAN cruises were subdivided into three sub-sets pertaining to the following large-scale oceanic sectors: (a) Northern Greenland Sea and Norwegian Sea (hereinafter referred to as GNS sector), between 20° W and 30° E longitudes; (b) Barents Sea and West Siberian Sea (BWS sector), between 30° E and 130° E longitudes; and (c) the North American Arctic Ocean (NAA sector), including the East Chukchi Sea, the Bering Strait, the Beaufort Sea and the Amundsen Gulf, between 170° W and 110° W longitudes. No MAN cruises were carried out in the East Siberian Sea and West Chukchi Sea sectors, at latitudes higher than 67° N and longitudes ranging from 130° E to 170° W, as well as in the Canadian sector from 110° W to 20° W longitudes, including the Baffin Bay, the Davis Straits and the Northern Atlantic Ocean.

The same criteria as used for the ground-based stationary sun-photometer measurements taken at the various Arctic sites were also adopted to examine the ship-borne measurements, including the selection of data made to reject all the measurements affected by stratospheric volcanic particle extinction. The daily mean values of  $\tau(0.50 \mu\text{m})$  and  $\alpha$  obtained from the data-sets collected within each of the three oceanic sectors were subdivided into monthly sub-sets to determine the monthly mean values of both parameters, and define their RFHs separately for the winter–spring (Arctic haze) and summer–autumn (background aerosol) periods. The main purpose of the analysis was

to provide evidence of the seasonal characteristics of aerosol optical parameters in the Arctic Ocean areas far from anthropogenic aerosol sources.

### 3.1.1. Northern Greenland Sea and Norwegian Sea

Monthly mean values of  $\tau(0.50 \mu\text{m})$  and  $\alpha$  derived from the Microtops measurements performed during nine cruises made in the Norwegian Sea, west of Spitsbergen, and one cruise in the northern Greenland Sea and Norwegian Sea are shown in Fig. 14a. Values of  $\tau(0.50 \mu\text{m})$  gradually decreased from less than 0.10 in April to nearly 0.05 in August, with values of  $\sigma_\tau < 0.03$  over the entire period. The monthly mean values of  $\alpha$  were rather stable from April to August, ranging from 1.20 to 1.30, with values of  $\sigma_\alpha$  equal to 0.10 in spring and 0.40 in summer. These features suggest that the columnar aerosol content was mixed in spring, consisting of anthropogenic (Arctic haze) and natural sea-salt aerosols, and contained sea-salt aerosol mixed with BFF smoke particles in summer. In fact, the aerosol extinction parameters measured in spring and summer with the Microtops sun-photometers turn out to be very similar to those determined at Ittoqqortoormiit and Hornsund from the AERONET sun-photometer measurements, during spring (when polluted air masses are mainly transported from Europe) and summer (when polar air masses are transported from the Arctic land and oceanic regions towards the Svalbard Archipelago) (Rozwadowska and Sobolewski, 2010; Rozwadowska et al., 2010). These variable features can be more clearly seen by considering the seasonal RFHs of  $\tau(0.50 \mu\text{m})$  and  $\alpha$  shown in Fig. 14b, derived from the measurements taken on 77 measurement days in the Greenland Sea and Norwegian Sea (GNS) sector. The RFH of  $\tau(0.50 \mu\text{m})$  exhibits a large peak over the 0.02–0.20 range, with a mean value equal to 0.075, and 25th and 75th percentiles equal to 0.054 and 0.094, respectively, indicating significant variations even in the remote Arctic Ocean. The corresponding RFH of  $\alpha$  is also rather wide, showing a mean value of 1.23, and 25th and 75th percentiles equal to 1.02 and 1.47, respectively, as a result of the combination of natural maritime and anthropogenic/continental aerosol loads. It is worth noticing that the GNS average values of  $\tau(0.50 \mu\text{m})$  and  $\alpha$  agree fairly well with those determined at Ittoqqortoormiit (Fig. 5) and Hornsund (Fig. 6) and exhibit similar relationships between  $\alpha$  and  $\tau(0.50 \mu\text{m})$  to those of the above-mentioned AERONET stations (compare Fig. 8a with those of Fig. 8b).

### 3.1.2. Barents Sea and West Siberian Sea

Only the RV Polarstern 2012 cruise crossed the Barents Sea and West Siberian Sea (BWS) sector, in August 2012, at latitudes varying from 80° N to 84° N and longitudes ranging from 28° E to 120° E (see Fig. 2). Thus, the monthly mean values of  $\tau(0.50 \mu\text{m})$  and  $\alpha$  were only calculated for three measurement days, giving statistically poor values of  $\tau(0.50 \mu\text{m}) = 0.054 \pm 0.010$  and  $\alpha = 1.42 \pm 0.33$ . As noted in Fig. 14a, the above value of  $\tau(0.50 \mu\text{m})$  closely agrees with that measured within the GNS sector on the same month, and  $\alpha$  is slightly higher than that measured in August within the same sector. Such results are typical of an oceanic area during relatively calm wind periods.

### 3.1.3. North American Arctic Ocean

Within the North American Arctic (NAA) oceanic sector, including the East Chukchi Sea, Bering Strait, Beaufort Sea and Amundsen Gulf, only four cruises were considered among those reported in Table 3. The time-patterns of the monthly mean values of  $\tau(0.50 \mu\text{m})$  and  $\alpha$  calculated over the March–September period are shown in Fig. 14a. Monthly mean value of  $\tau(0.50 \mu\text{m})$  were about 0.10 in March, peaked in April and May at 0.17 and 0.20, respectively, and decreased in the summer months to 0.10 in June and 0.05 in September. No pronounced variations in  $\alpha$  were obtained, with values from 0.90 to 1.20 from March to September, and  $\sigma_\alpha$  varying from 0.20 (in April) to 0.50 (in July). An overall number of 58 measurement days was collected in this oceanic sector over the 7-month period from March to September, for which

**Table 3**

List of the 14 cruises undertaken in the Arctic oceanic regions by various managing institutions in different geographical areas (at latitudes  $>67^\circ$  N), where the ship-borne Level 2.0 sun-photometer measurements of the Maritime Aerosol Network (MAN) programme were conducted from 2003 to 2012, using hand-held Microtops sun-photometers calibrated at the NASA/GSFC calibration facility (Smirnov et al., 2009, 2011). The peak wavelengths of the narrow-band interference filters mounted on the instruments are given, together with the names of the sun-photometer measurement P.I.s.

Cruises and sun-photometer managing institutions	Geographical area	Overall number of measurement days	Measurement period	Peak wavelengths (nm) of the spectral channels used to measure aerosol optical thickness $\tau(\lambda)$	Principal investigator and references
RV Oceania 2003 (IOPAS, Sopot, Poland)	Norwegian Sea, west Spitsbergen $69^\circ$ – $79^\circ$ N, $2^\circ$ – $14^\circ$ E	5	June–July 2003	440, 500, 675, 870	T. Zielinsky (Tomasi et al., 2007)
RV Oceania 2006 (IOPAS, Sopot, Poland)	Greenland Sea and Norwegian Sea, $69^\circ$ – $79^\circ$ N, $15^\circ$ W– $14^\circ$ E	6	June–July 2006	440, 500, 675, 870	T. Zielinsky (Tomasi et al., 2007)
RV Oceania 2007 (IOPAS, Sopot, Poland)	Norwegian Sea, $69^\circ$ – $78^\circ$ N, $1^\circ$ – $16^\circ$ E	6	July 15–August 11, 2007	440, 500, 675, 870	T. Zielinsky
CCGS Louis St. Laurent 2007 (Wood Hole Oceanographic Institution, Woods Hole, Massachusetts, USA)	Beaufort Sea, $70^\circ$ – $79^\circ$ N, $125^\circ$ – $150^\circ$ W	9	July 28–August 25, 2007	440, 500, 675, 870	A. Proshutinsky
RV Knorr 2008 (PMEL, NOAA, Seattle, Washington, USA)	Norwegian Sea, $70^\circ$ – $71^\circ$ N, $19^\circ$ – $31^\circ$ E	4	April 6–10, 2008	440, 500, 675, 870	P. K. Quinn
CCGS Amundsen 2008 (Institut Maurice-Lamontagne, Mont-Joli, Quebec, Canada)	Beaufort Sea, $70^\circ$ – $73^\circ$ N, $121^\circ$ – $131^\circ$ W	43	March 16–August 2, 2008	440, 500, 675, 870	P. Larouche
RV Jan Mayen 2009 (IMEDEA, Esporles, Mallorca, Spain)	Norwegian Sea, $76^\circ$ – $80^\circ$ N, $11^\circ$ – $28^\circ$ E	4	June 18–22, 2009	440, 500, 675, 870	C. Duarte
RV Oceania 2009 (IOPAS, Sopot, Poland)	Norwegian Sea, $73^\circ$ – $79^\circ$ N, $3^\circ$ – $16^\circ$ E	11	June 23–July 13, 2009	440, 500, 675, 870	T. Zielinsky
CCGS Amundsen 2009 (Université du Québec, Rimouski, Québec, Canada)	Beaufort Sea, $70^\circ$ – $72^\circ$ N, $127^\circ$ – $135^\circ$ W	9	July 31–August 25, 2009	440, 500, 675, 870	S. Bélanger
RV Oceania 2010 (IOPAS, Sopot, Poland)	Norwegian Sea, $68^\circ$ – $80^\circ$ N, $0^\circ$ – $13^\circ$ E	9	July 6–August 17, 2010	380, 440, 500, 675, 870	T. Zielinsky
RV Oceania 2011 (IOPAS, Sopot, Poland)	Norwegian Sea, $69^\circ$ – $79^\circ$ N, $3^\circ$ – $19^\circ$ E	10	June 17–August 13, 2011	440, 500, 675, 870	T. Zielinsky
USCGC Healy 2011 (Naval Research Laboratory, Monterey, California, USA)	Eastern Chukchi Sea, Beaufort Sea and Arctic Canadian Ocean, $71^\circ$ – $79^\circ$ N, $142^\circ$ – $165^\circ$ W	6	August 18–September 24, 2011	440, 500, 675, 870	E. A. Reid
RV Oceania 2012 (IOPAS, Sopot, Poland)	Norwegian Sea, $73^\circ$ – $78^\circ$ N, $10^\circ$ – $20^\circ$ E	7	June 27–July 31, 2012	440, 500, 675, 870	T. Zielinsky
RV Polarstern 2012 (Institute of Environmental Physics, University of Bremen, Bremen, Germany)	Norwegian Sea, Barents Sea and West Siberian Sea, $70^\circ$ – $84^\circ$ N, $18^\circ$ – $109^\circ$ E	5	August 2–22, 2012	440, 500, 675, 870	L. Istomina

calculations of the RFHs were made, illustrating a statistically robust data-set. The RFH of  $\tau(0.50 \mu\text{m})$  showed a more dispersed distribution curve over the 0.02–0.25 range than that determined for the GNS sector, with a mean value of 0.16, which was considerably higher than that measured in the GNS sector, and also had wider right-hand wings. The RFH of  $\alpha$  exhibits a similar shape to that determined in the GNS sector, with a mean value close to 1.10.

The median values and the 25th and 75th percentiles of parameters  $\tau(0.50 \mu\text{m})$  and  $\alpha$  were calculated for the sets of daily mean values derived from the Microtops sun-photometer measurements conducted over the GNS, BWS and NAA sectors. The results are shown in Fig. 8b for an easier comparison with those derived from the ground-based sun-photometer measurements conducted at Arctic sites. The ship-borne measurements provided median values of  $\tau(0.50 \mu\text{m})$  ranging from 0.04 to about 0.13, which are therefore comparable with the mean background extinction parameter measured in summer at the ground-based stations. The ship-borne median values of  $\alpha$  varied mainly from 1.10 to 1.50, and were appreciably lower than those measured in summer–autumn at the land stations: the scatter plot shown in Fig. 8b provides clear evidence of the prevailing oceanic origins of these aerosol loads.

### 3.2. Aerosol measurements in the Antarctic Ocean

Eighteen AERONET/MAN cruises were conducted from 2006 to early 2013 over the Antarctic Oceans. They are listed in Table 4, together with the geographical areas covered by the various cruises, the number of measurements days (see also Fig. 2), the measurement periods and the spectral characteristics of the portable Microtops sun-photometers onboard the vessels. To analyse the aerosol optical parameters more

homogeneously, the sun-photometer data-sets recorded during the 18 cruises were subdivided into the following four sub-sets: (1) the Southern Indian Ocean (IND) sector, between  $20^\circ$  E and  $150^\circ$  E longitudes; (2) the Southern Pacific Ocean (PAC) sector, between  $150^\circ$  E and  $75^\circ$  W longitudes; (3) the Southern Atlantic Ocean (ATL) sector, between  $50^\circ$  W and  $20^\circ$  E longitudes; and (4) the oceanic region around the Antarctic Peninsula (APE), between  $75^\circ$  and  $50^\circ$  W longitudes. The daily mean values of  $\tau(0.50 \mu\text{m})$  and  $\alpha$  measured with the portable Microtops sun-photometers calibrated at NASA/GSFC facility (Smirnov et al., 2009, 2011) were analysed separately for coastal data (for distances smaller than 300 km from the Antarctic coast) and off-shore data (for distances of 300 to 1000 km from the coast), according to the criteria used by Wilson et al. (2010) to distinguish the data related to a significant landmass from those of pure oceanic origin (i.e., given for the large part by maritime aerosols generated by wind-related sources). The overall set of Microtops data was then examined following the same criteria adopted to analyse the Arctic ship-borne measurements, separately for the above-mentioned four oceanic sectors.

#### 3.2.1. Southern Indian Ocean

As can be seen in Table 4, eleven cruises were conducted in the Southern Indian Ocean, during periods from December to March in the years from 2005/2006 to 2011/2012, collecting an overall set of 226 coastal measurement days, and only nine off-shore measurement days (see Fig. 2). The time-patterns of the monthly mean values of  $\tau(0.50 \mu\text{m})$  and  $\alpha$  are shown in Fig. 15a for coastal and off-shore data. AOT values of  $\tau(0.50 \mu\text{m})$  were rather stable from December to April over the coastal areas, varying from 0.010 to 0.025, with  $\sigma_\tau = \pm 0.01$  on average, and were appreciably greater over the off-shore area, being close to  $\sim 0.06$  in January, 0.04 in November and December, and



**Table 4**

List of the 18 cruises undertaken in the Antarctic oceanic regions by various managing institutions in different geographical areas (at latitudes  $>62^{\circ}$  S), where the ship-borne sun-photometer measurements of the Maritime Aerosol Network (MAN) programme were conducted from 2005/2006 to 2012/2013 in the austral summer months, using hand-held Microtops sun-photometers calibrated at the NASA/GSFC calibration facility (Smirnov et al., 2009, 2011). The peak wavelengths of the narrow-band interference filters mounted on the instruments are given, together with the names of the sun-photometer measurement P.I.s.

Cruises and sun-photometer managing institution	Geographical area	Overall number of measurement days	Measurement period	Peak wavelengths (nm) of the spectral channels used for measuring aerosol optical thickness $\tau(\lambda)$	Principal investigator
RV Akademik Fedorov 2005/2006 (IAO-SB-RAS, Tomsk, Russia)	Southern Indian Ocean 65°–70° S, 44°–93° E	20	December 20, 2005–January 26, 2006	340, 440, 500, 675, 870	S. M. Sakerin
RV Akademik Fedorov 2006/2007 (IAO-SB-RAS, Tomsk, Russia)	Southern Indian Ocean 65°–69° S, 46°–93° E	40	December 13, 2006–March 4, 2007	340, 440, 500, 675, 870	S. M. Sakerin
MV SA Agulhas 2007/2008 (Climatology Research Group, University of Witwatersrand, Johannesburg, South Africa)	Southern Atlantic Ocean, 68°–70° S, 2° W–4° E	15	December 18, 2007–January 10, 2008	440, 500, 675, 870	S. Piketh (Wilson et al., 2010)
RV Akademik Fedorov 2007/2008 (IAO-SB-RAS, Tomsk, Russia)	Southern Indian Ocean, 66°–69° S, 45° E–95° E	18	December 14, 2007–January 4, 2008	440, 500, 675, 870	S. M. Sakerin
	Southern Pacific Ocean, 68°–72° S, 90°–163° W	14	January 24–February 17, 2008		
	Antarctic Peninsula, 63°–65° S, 60°–45° W	3	February 20–24, 2008		
	Southern Atlantic Ocean, 65°–70° S, 50°W–15° E	13	March 25–April 22, 2008		
RV Akademik Fedorov 2008/2009 (IAO-SB-RAS, Tomsk, Russia)	Southern Indian Ocean, 66°–69° S, 76°–93° E	11	December 22, 2008–January 6, 2009; January 25–March 23, 2009	440, 500, 675, 870	S. M. Sakerin
	Southern Pacific Ocean, 67° S, 161° E	1	January 17, 2009		
Vessel RV Astrolabe 2009/2010 (OPAR, Univ. de Reunion, Reunion, France)	Southern Indian Ocean 66°–67° S, 140°–141° E	5	January 5–23, 2010	440, 500, 675, 870	Y. Courcoux
RV Akademik Fedorov 2009/2010 (IAO-SB-RAS, Tomsk, Russia)	Southern Indian Ocean, 65°–70° S, 70°–100° E	12	December 15, 2009–January 4, 2010; March 30–April 6, 2010	440, 500, 675, 870	S. M. Sakerin
	Southern Pacific Ocean 65°–75° S, 87°–172° W	7	January 19–28, 2010		
	Antarctic Peninsula, 62° S, 59° W	1	February 6, 2010		
Prince Albert II 2010 (Space Physics Laboratory, University of Kyiv, Kyiv, Ukraine)	Antarctic Peninsula 62°–67° S, 58°–67° W	11	January 9–February 17, 2010	440, 500, 675, 870	G. Milinevsky
NP Almirante Maximiano 2010/2011 (Rio de Janeiro State University, Rio de Janeiro, Brazil)	Antarctic Peninsula 62°–64° S, 56°–61° W	7	January 7–March 21, 2011	440, 500, 675, 870	H. Evangelista
RV Akademik Fedorov 2010/2011 (AARI, St. Petersburg, Russia)	Southern Indian Ocean 65°–69° S, 45°–93° E	18	December 18, 2010–February 2, 2011	440, 500, 675, 870	V. F. Radionov
RV Astrolabe 2011 (OPAR Institute, Univ. de la Réunion, Saint Denis de la Réunion, France)	Southern Indian Ocean 67° S, 140° E	24	January 5–March 1, 2011	340, 440, 500, 675, 870	Y. Courcoux
MV SA Agulhas 2011/2012 (Climatology Research Group, University of Witwatersrand, Johannesburg, South Africa)	Southern Atlantic Ocean 67°–71° S, 0°–9° W	17	December 19, 2011–February 13, 2012	340, 440, 500, 675, 870	S. Broccardo
NP Almirante Maximiano 2011/2012 (Rio de Janeiro State University, Rio de Janeiro, Brazil)	Antarctic Peninsula, 61°–62° S, 55°–59° W	6	October 24, 2011–November 14, 2011	440, 500, 675, 870	H. Evangelista
RV Akademik Fedorov 2011/2012 (AARI, St. Petersburg, Russia)	Southern Indian Ocean 66°–69° S, 37°–93° E	19	December 12, 2011–March 21, 2012	440, 500, 675, 870	V. F. Radionov
	Southern Atlantic Ocean 62°–70° S, 18° W–20° E	8	March 22–April 7, 2012		
	Antarctic Peninsula 62.2° S, 58.9° W	2	April 21 and 22, 2012		
RV Astrolabe 2012 (OPAR Institute, Univ. de la Réunion, Saint Denis de la Réunion, France)	Southern Indian Ocean 66° 40' S, 140° E	14	February 20–March 2, 2012	380, 440, 500, 675, 870	Y. Courcoux
RV SA Agulhas II 2012/2013 (Climatology Research Group, University of Witwatersrand, Johannesburg, South Africa)	Southern Atlantic Ocean 70°–71° S, 1°–8° W	11	December 19, 2012–February 5, 2013	380, 440, 500, 675, 870	S. Broccardo
RV Akademik Fedorov 2012/2013 (AARI, St. Petersburg, Russia)	Southern Indian Ocean 66°–70° S, 46°–93° E	24	December 13, 2012–March 15, 2013	440, 500, 675, 870	V. F. Radionov
	Southern Atlantic Ocean 67°–70° S, 10°–12° E	3	March 22–24, 2013		
RV Akademik Treshnikov 2012/2013 (AARI, St. Petersburg, Russia)	Antarctic Peninsula, 64°–70° S, 57°–72° W	13	February 11–March 5, 2013	440, 500, 675, 870	V. F. Radionov

0.02 in February. The coastal values of  $\alpha$  varied from 1.20 to 1.40 in the December–April period, while the off-shore values decreased from 1.20 to less than 0.60 from November to December, and then slowly increased to around 0.90 in February. These findings give a measure of the increase in  $\tau(\lambda)$  and the variations in  $\alpha$ , which are observed passing from coastal to off-shore areas as a result of the stronger production of sea-salt coarse particles. The daily mean values of  $\tau(0.50 \mu\text{m})$  and  $\alpha$

were derived over the Southern Indian Ocean on 226 measurement days near the Antarctic coasts, and on only nine days in off-shore areas. Therefore, only the RFHs of the coastal daily mean values of  $\tau(0.50 \mu\text{m})$  and  $\alpha$  have been analysed: the RFH of  $\tau(0.50 \mu\text{m})$  shown in Fig. 15b presents a very narrow curve, with a mean value of 0.024, and 25th and 75th percentiles very close to the mean, while the RFH of  $\alpha$  exhibits a broad curve, with a mean value of 1.20 and 25th and

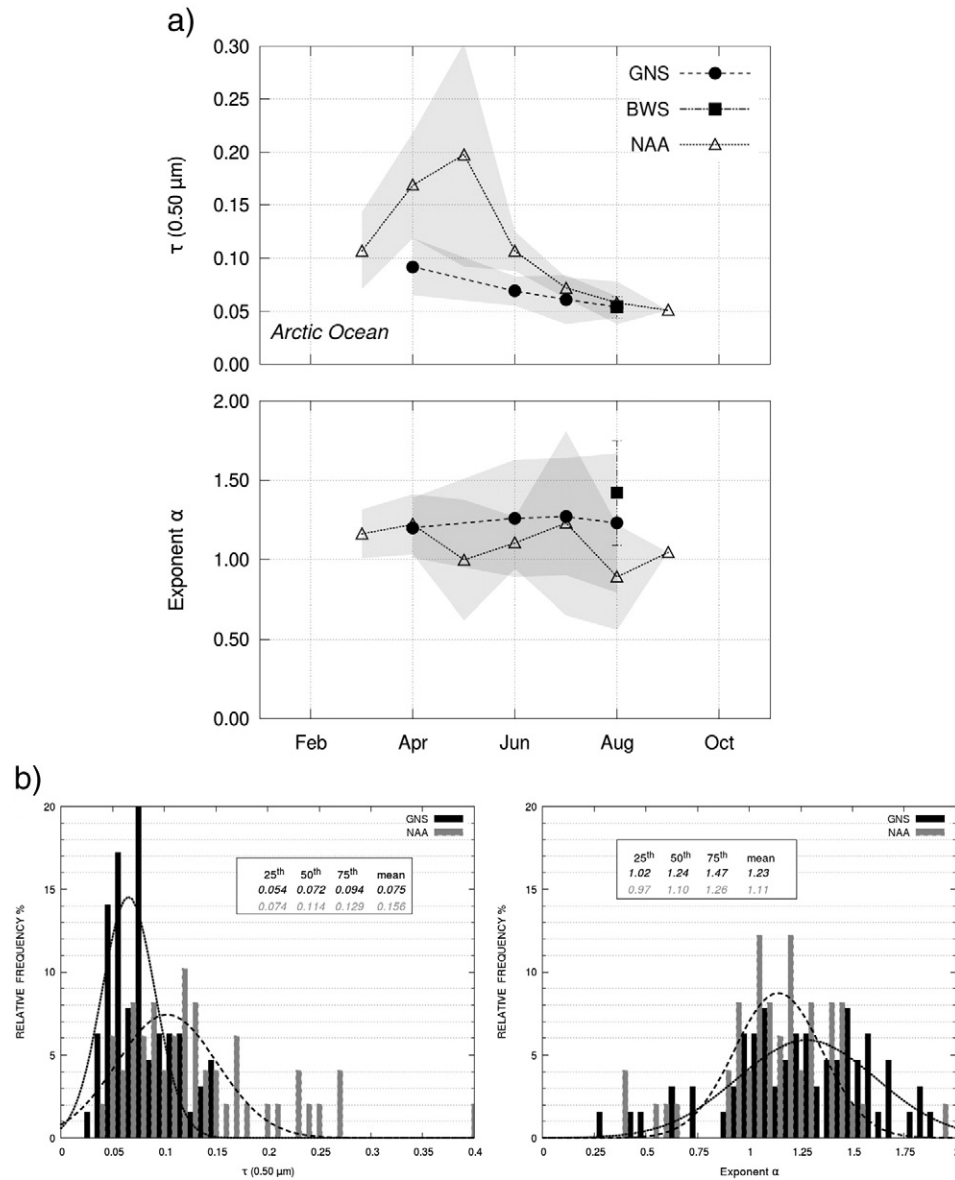


**Fig. 14.** Part (a): as in Fig. 3, for Microtops sun-photometer measurements of aerosol optical thickness  $\tau(0.50 \mu\text{m})$  and exponent  $\alpha$  performed during the cruises conducted from 2003 to 2012 in the GNS (Greenland Sea and Norwegian Sea) sector (solid circles), from 2006 to 2012 in the BWS (Barents Sea and West Siberian Sea) sector (solid squares), and from 2008 to 2011 in the NAA (Eastern Chuckci Sea, Beaufort Sea and Amundsen Gulf) sector (open triangles) (see also Table 3). Part (b): relative frequency histograms of the daily mean values of aerosol optical thickness  $\tau(0.50 \mu\text{m})$  and exponent  $\alpha$  determined from the Microtops measurements conducted from March to September over the GNS (Greenland Sea and Norwegian Sea) sector, and the NAA (North American Arctic Ocean) sector, including the Eastern Chuckci Sea, Beaufort Sea and Amundsen Gulf.

75th percentiles equal to 0.84 and 1.51. These findings clearly indicate that a large variability characterises the sea-salt accumulation and coarse mode particle concentrations in coastal areas.

### 3.2.2. Southern Pacific Ocean

As reported in Table 4, only three AERONET/MAN cruises were conducted in the Southern Pacific Ocean over the December–January periods of 2007/2008 to 2009/2010, over the area defined in Fig. 2, giving an overall number of 20 coastal and 5 off-shore measurement days. The monthly mean values of  $\tau(0.50 \mu\text{m})$  and  $\alpha$  varied from 0.03 to 0.04 near the coasts, and from 0.04 to 0.05 in the off-shore areas, while the coastal monthly mean values of  $\alpha$  decreased from  $\sim 1.45$  in December to  $\sim 1.00$  in January, and the off-shore values from 1.40 to 0.70. The values of  $\tau(0.50 \mu\text{m})$  and  $\alpha$  result to closely agree with those measured at Neumayer, Novolazarevskaya, Mirny, Syowa, and Mario Zucchelli, shown in Figs. 9–12. A coastal median value of  $\tau(0.50 \mu\text{m})$  equal to  $\sim 0.04$  was obtained, with the main percentiles differing by

less than 0.02, while the median value of  $\alpha$  was equal to 1.20, with the main percentiles differing by about 0.50. The off-shore data-set provided a similar value of  $\tau(0.50 \mu\text{m})$  and more distant main percentiles, with a median value of  $\alpha = 1.15$ , and main percentiles differing by more than 0.40.

### 3.2.3. Southern Atlantic Ocean

A large set of AERONET/MAN sun-photometer measurements was collected in the Southern Atlantic Ocean during five cruises conducted in 2007/2008, 2011/2012 and 2012/2013, as reported in Table 4, giving 63 coastal and only 8 off-shore measurement days. The monthly mean values of  $\tau(0.50 \mu\text{m})$  varied from 0.03 in December to less than 0.02 in April, with  $\sigma_\tau = 0.01$  on average, while those of  $\alpha$  increased from  $\sim 1.10$  in December to 1.50 in February, and then decreased to 1.30 in April. The RFH of the coastal  $\tau(0.50 \mu\text{m})$  values was found to exhibit similar features to those determined in the coastal area of the Antarctic Indian Ocean, with a leptokurtic shape having a mean value of 0.025

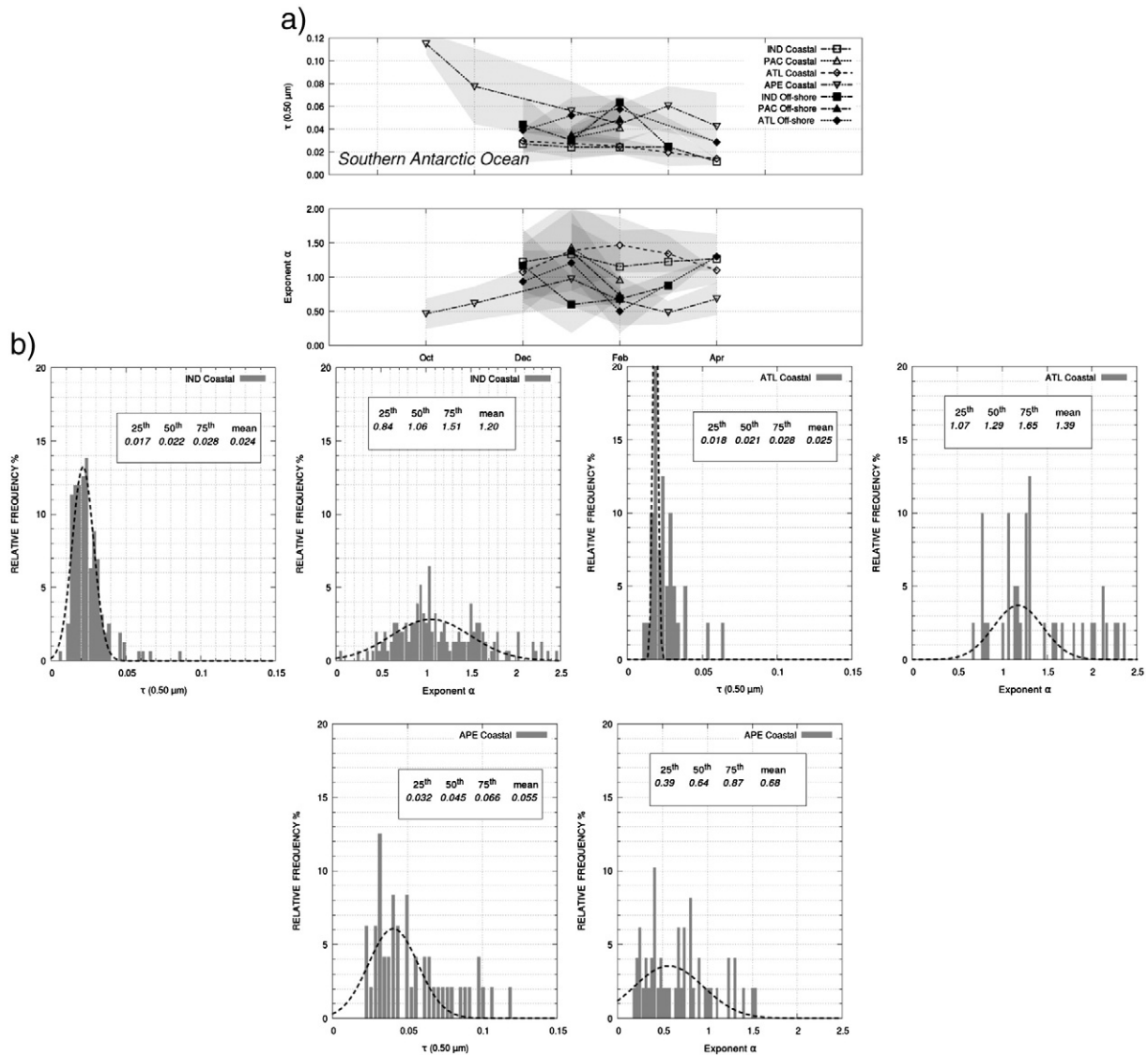


**Fig. 15.** Part (a): as in Fig. 3, for Microtops sun-photometer measurements of  $\tau(0.50 \mu\text{m})$  and  $\alpha$  performed during the cruises conducted from late 2005 to spring 2013 in the frame of the Maritime Aerosol Network (MAN) activities listed in Table 4. The data refer to coastal (open symbols) and off-shore (solid symbols) measurements, carried out in the IND sector (Southern Indian Ocean, circles), PAC sector (Southern Pacific Ocean, upward triangles), ATL sector (Southern Atlantic Ocean, squares), and APE sector (Antarctic Peninsula, downward triangles). Part (b): Relative frequency histograms of  $\tau(0.50 \mu\text{m})$  and  $\alpha$  obtained for the coastal data-sets collected (i) on 226 measurement days from November to February over the Southern Indian Ocean (IND) sector; (ii) 63 measurement days from December to April over the Southern Atlantic Ocean (ATL) sector; and (iii) on 49 measurement days from October to April over the coastal area surrounding the Antarctic Peninsula (APE sector).

and the 25th and 75th percentiles differing by less than 0.01, while the RFH of  $\alpha$  showed a rather broad shape over the 0.5–2.4 range, with a mean value of 1.39 and the 25th and 75th percentiles differing by about 0.30, thus being similar to that determined for the Pacific Ocean coastal data-set.

### 3.2.4. Around the Antarctic Peninsula

Numerous aerosol optical data were collected in coastal areas surrounding the Antarctic Peninsula during the seven AERONET/MAN cruises conducted from 2007/2008 to 2012/2013, as reported in Table 4, collecting an overall number of 49 measurement days, not far from the coasts. The time-patterns of monthly mean values of  $\tau(0.50 \mu\text{m})$  and  $\alpha$  obtained from these measurements are shown in Fig. 15b. A very high value of  $\tau(0.50 \mu\text{m})$  close to 0.12 was obtained in October, followed by decreasing monthly mean values equal to 0.08 in November and lower than 0.06 in December, and then varying from 0.04 to 0.06 over the January–March period, with  $\sigma_\tau = 0.02$  on average. The monthly mean values of  $\alpha$  were all rather low, varying from 0.50 to 1.00 over the October–February period, with  $\sigma_\alpha = 0.20$  on average. The

exceptionally high monthly mean values of  $\tau(0.50 \mu\text{m})$  were determined in October and November for measurement days giving values of  $\alpha$  varying from 0.24 to 0.69, and presenting prevailing transport of air masses from the off-shore areas of the Drake Passage. Similar aerosol optical characteristics were observed by Posyniak and Markowicz (2009) for flows from the North-Eastern quadrant, accompanied by low visibility conditions because of the transport of large amounts of sea-salt particles from the Drake Passage, with wind speed  $> 10$  m/s. Relatively low daily mean values of  $\alpha$  were measured on these days, ranging from 0.43 to 0.73, due to maritime aerosols generated by the strong winds, which dominated extinction. For southerly wind circulation, considerably lower values of  $\tau(0.50 \mu\text{m})$  were measured in this coastal area. Therefore, because of the large variability of wind directions, the RFH of  $\tau(0.50 \mu\text{m})$  determined over the October–March period exhibited rather dispersed features, with a mean value of  $\sim 0.05$  and the 25th and 75th percentiles differing by less than 0.02. These evaluations are higher by about a factor 2 than those obtained over the coastal areas of the Indian and Atlantic Oceans, because of the more significant contribution of sea-salt accumulation and coarse mode particles generated by



stronger winds. The RFH of  $\alpha$  shows a rather broad shape over the range  $\alpha < 1.5$ , with a mean value close to 0.70, which is about half of that measured over the Indian and Atlantic Ocean coastal areas, and the 25th and 75th percentiles differing by no more than 0.30, due to the predominant extinction by maritime particles.

The above results obtained from the coastal and off-shore data recorded over the four sectors of the Southern Antarctic Ocean are characterised by features of  $\tau(0.50 \mu\text{m})$  and  $\alpha$  typical of sea-salt maritime particles, as can be clearly seen in Fig. 13b, in which the median values of  $\alpha$  are plotted versus the median values of  $\tau(0.50 \mu\text{m})$ , separately for the coastal and off-shore data. The comparison between these results and the scatter plot shown in Fig. 13a shows that they are very similar to those derived from the sun-photometer measurements conducted at the coastal Antarctic stations, since the cluster derived from the AERONET/MAN measurements of  $\alpha$  and  $\tau(0.50 \mu\text{m})$  essentially covers the same domain of the ground-based measurements recorded at Marambio, Novolazarevskaya, Syowa, Neumayer, and Mario Zucchelli, although exhibiting slightly lower values of  $\alpha$ .

#### 4. Aerosol backscattering coefficient profiles from lidar measurements

Lidar sends a light pulse through the atmosphere and the telescope collects the backscattered lidar return signal. As the speed of light is known, one can easily calculate the exact atmospheric position, from which the lidar signal has originated. Therefore, the determination of aerosol vertical structure is possible, at least over the altitude range in which the image of the laser is completely within the field-of-view of the recording telescope. Lidar pulses can be generated at several wavelengths and polarisation elements can also be used at the point of light entrance to the telescope. This enables a determination of the shape of scatterers because spherical particles do not depolarise light, while non-spherical particles normally do.

Overcoming the considerable operational and logistic difficulties, various lidar systems have been deployed in the polar regions to measure: (i) the vertical profiles of backscatter and extinction coefficients of the various aerosols, cloud droplets and ice-crystals, as well as their microphysical and radiative characteristics; (ii) the vertical distribution of temperature and water vapour mixing ratio; and (iii) the ozone concentration at stratospheric levels, to more thoroughly investigate the role of Polar Stratospheric Clouds in destroying ozone molecules at polar latitudes. Actually, most of these measurements were conducted to study the dynamic features of the ozone hole in Antarctica and ozone depletion in the Arctic region associated with the polar vortex occurrences, and the physical characteristics of tropospheric clouds, while relatively few measurement campaigns were specifically conducted with lidar techniques to investigate the optical characteristics of tropospheric aerosols at polar latitudes. An exhaustive description of the lidar measurements conducted in polar regions over the past few decades was recently made (Nott and Duck, 2011). Lidar activities were conducted in the Arctic at the following sites:

- (i) Barrow (Northern Alaska), where long-term lidar measurements were recorded and a micropulse lidar is currently used to carry out cloud climatology studies that have evaluated average seasonal cloud occurrences of 65% in winter, 68% in spring, 83% in summer, and 89% in autumn, with an annual mean decrease of  $-4.8\%$  per year over the past 10 years (Dong et al., 2010).
- (ii) Eureka (Nunavut, Canada), where an elastic lidar was used from 1993 to 1997 to carry out winter-time aerosol measurements for studying the occurrences of clouds and Arctic haze. Backscatter peaks due to haze particle layers were frequently observed at altitudes lower than 3 km, and more occasionally at altitudes of 3–5 km, for relative humidity  $< 60\%$  over ice, while clouds dominate at  $> 80\%$  over ice. Spectral measurements of the aerosol backscatter coefficient  $\beta_{bs}(\lambda)$  and depolarisation ratio  $\delta_V(\lambda)$

were regularly conducted from 2005 to 2010, over the height range from 70 m up to approximately 15 km, using a High Spectral Resolution Lidar (HSRL) of the University of Wisconsin (USA), at the wavelengths 0.532 and 1.064  $\mu\text{m}$ , for the aerosol backscatter coefficient  $\beta_{bs}(\lambda)$ , and 0.532  $\mu\text{m}$  only for  $\delta_V(\lambda)$  and  $\beta_{ext}(\lambda)$ . This lidar system was used together with a millimetre cloud radar to classify the various cloud particle types. Since 2008, a troposphere ozone DIAL (Differential Absorption Lidar) and a Raman lidar have been operated simultaneously, equipped with aerosol channels in the visible and ultraviolet light and water vapour and rotational Raman temperature channels.

- (iii) Alert (Nunavut, Canada), where an elastic lidar was operated in 1984–1986 to measure the vertical profiles of aerosol backscatter coefficient.
- (iv) Summit (Central Greenland), where a depolarisation lidar and a micropulse lidar were used since 2010, to characterise the aerosol types suspended over the Greenland ice sheet.
- (v) Ny-Ålesund (Spitsbergen, Svalbard), where various lidar models were used, such as: (a) a stratospheric lidar since 1988; (b) the KARL (Koldewey-Aerosol-Raman Lidar) since 1999, this system being equipped with aerosol channels, depolarisation and ultraviolet and visible water vapour channels, and subsequently rebuilt in 2008 with enhanced multi-wavelength aerosol channels to cover the 0.45–30 km altitude range; and (c) an automated micropulse lidar (Hoffmann et al., 2009) since 2003, as a part of the MPLNET and NDACC networks, which provided cloud and aerosol measurements in March and April 2007, useful to characterise air masses as a function of depolarisation and backscatter ratios.
- (vi) Hornsund (Spitsbergen, Svalbard), where an automated lidar has been operated since 2009, to measure the vertical profiles of volume extinction coefficient  $\beta_{ext}(0.532 \mu\text{m})$  produced by aerosols during transport episodes of unpolluted air masses from the Greenland Sea and Norwegian Sea areas; and
- (vi) Andøya Rocket Range (Arctic Lidar Observatory for Middle Atmosphere Research, ALOMAR), near Andenes (Northern Norway), where a tropospheric lidar was installed in 2005 and a polarisation-sensitive bistatic lidar system has been used since 2006 to study the vertical distribution features of polar aerosols and their optical characteristics.

The above-mentioned field measurements provided vertical profiles of the most significant aerosol scattering parameters, illustrating that the Arctic haze particles are in general present below the 3 km level during severe haze events, and occasionally at 3–5 km altitudes, as shown by the measurements conducted at Eureka (Nott and Duck, 2011). During the dense haze episode observed with the KARL lidar at Ny-Ålesund on May 2, 2006, strong extinction features were recorded from the ground up to 2.5 km altitude, which showed multi-layered profiles of the aerosol backscattering coefficient  $\beta_{bs}(0.532 \mu\text{m})$  decreasing on average from  $3.5 \text{ km}^{-1}$  near the ground to below  $0.5 \text{ km}^{-1}$  at 2.5 km altitude. Conversely, for unpolluted air conditions, the scale height of  $\beta_{bs}(0.532 \mu\text{m})$  was often found to vary from 1.0 to 1.3 km at Ny-Ålesund, as estimated for instance by Hoffmann et al. (2012) who examined the backscatter ratio measurements conducted with the KARL lidar over the whole of 2007.

However, so far our knowledge of Arctic haze from a lidar point of view is still incomplete, because the majority of published results are based on case studies. Therefore, the yearly cycle of aerosols has been studied in this paper on the basis of the lidar measurements conducted at Ny-Ålesund over the period from 1 November, 2012, to 31 October, 2013, examining the overall set of KARL lidar measurements taken without cloud interferences and with resolutions of 60 m in height and 10 min in time, according to Ansmann et al. (1992). To guarantee a homogeneous data-set, only lidar profiles with identical technical settings have been considered. Moreover, cloud screening was conducted

and the lowest 800 m were removed from the analysis due to overlap (Weitkamp, 2005). Finally, the data derived from the Vaisala RS-92 radiosonde data collected at the site have been used to subtract the Rayleigh backscatter coefficient from the lidar data. The fact that the time of the lidar observation does not coincide with the launch of the radiosonde should cause errors no higher than 5% in evaluating the aerosol backscatter coefficient. This is probably even an upper bound, since Rogers et al. (2011) only estimated a 3% bias for the CALIOP (Cloud-Aerosol Lidar with Orthogonal Polarization) lidar on board the CALIPSO satellite. Fig. 16 shows the monthly averaged profiles of the aerosol volumetric backscatter coefficient  $\beta_{bs}(0.532 \mu\text{m})$  from January to May and the three bi-monthly averaged profiles from June to December, providing evidence of significant variations in this optical parameter throughout the year. A clear annual cycle of the aerosol backscatter coefficient can be seen, which increased in February mainly in the low troposphere and reached its maximum values during March and April in the whole troposphere, subsequently decreasing appreciably in May. The months June to January were relatively clear, always showing appreciably lower values at all altitudes. Another view of the same data is shown in Fig. 17, where the monthly averaged values of  $\beta_{bs}(0.532 \mu\text{m})$  were integrated over five partial height-intervals and the total range from 0.8 to 7.0 km. The results show that the Arctic haze layer starts to form at low altitudes early in the season and lasts until May not only in the low troposphere but also at high altitudes. In fact, the maximum values below 2.5 km altitude have been found in March, while the largest values of  $\beta_{bs}(0.532 \mu\text{m})$  occur in April at 1.5–2.5 km altitudes. It can be also noted in Fig. 17 that the haze season starts more rapidly than it disappears, since the increase in backscatter observed between January and March is steeper, whereas the decline lasts from April till August.

The annual cycle of the lidar ratio  $S_a(0.532 \mu\text{m})$  between the aerosol extinction coefficient  $\beta_{ext}(0.532 \mu\text{m})$  and the aerosol backscatter coefficient  $\beta_{bs}(0.532 \mu\text{m})$  is presented in Fig. 18, separately calculated over the altitude sub-ranges  $z < 3.5 \text{ km}$  and  $z > 3.5 \text{ km}$  and over the whole altitude range, for the KARL lidar measurements conducted from early November 2012 to late October 2013. It shows that  $S_a(0.532 \mu\text{m})$  takes the highest values in June–July and generally increases with altitude. However, its annual cycle is not very pronounced below 3.5 km altitude, where most of the aerosol is located, presenting values varying from 30 to 35 sr. This is typical of clean continental aerosol (Winker et al., 2009). Conversely, the monthly mean values of  $S_a(0.532 \mu\text{m})$  calculated above

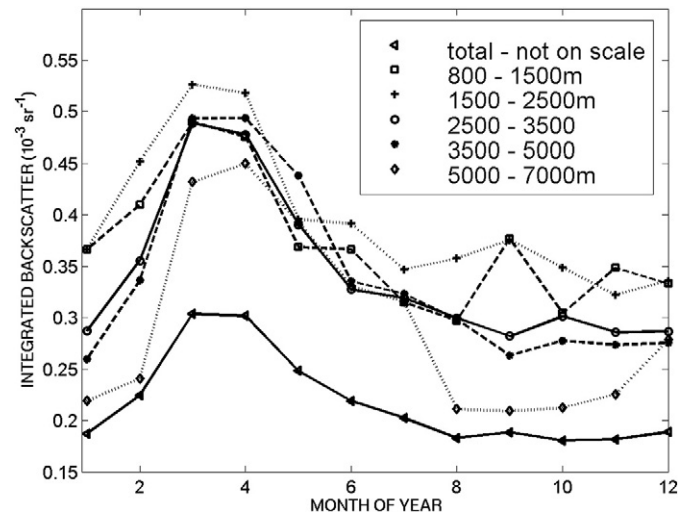


Fig. 17. Time-patterns of the monthly average values of the aerosol volume backscatter coefficient  $\beta_{bs}(0.532 \mu\text{m})$  integrated over the different altitude ranges reported in the legend, as obtained from the KARL lidar measurements performed at Ny-Ålesund (AWIPEV station) from 1 November, 2012, to 31 October, 2013.

3.5 km were estimated to vary from 30 to 40 sr in winter, i.e. assuming values typical of clean continental aerosol and dust, and to increase until reaching surprisingly high values of 60–70 sr in summer, which are normally typical of BFF smoke and polluted continental aerosol. However, one has to keep in mind that the lidar ratio depends not only on the chemical composition but also on the shape and size-distribution of aerosols. It also agrees well with the evaluations of  $S_a(0.532 \mu\text{m})$  made by Ackermann (1998) for different aerosol types suspended in air for relative humidity conditions ranging from 40% to 50%, estimated to be of 27 sr for maritime aerosols and around 55 sr for continental aerosol suspended in relatively dry air masses, like those frequently observed in the polar atmosphere over land (which probably indicate a decrease in the influence of marine air masses with altitude). Due to the contributions of both low and high tropospheric regions, the overall values of  $S_a(0.532 \mu\text{m})$  were estimated to range mainly from 30 to 50 sr.

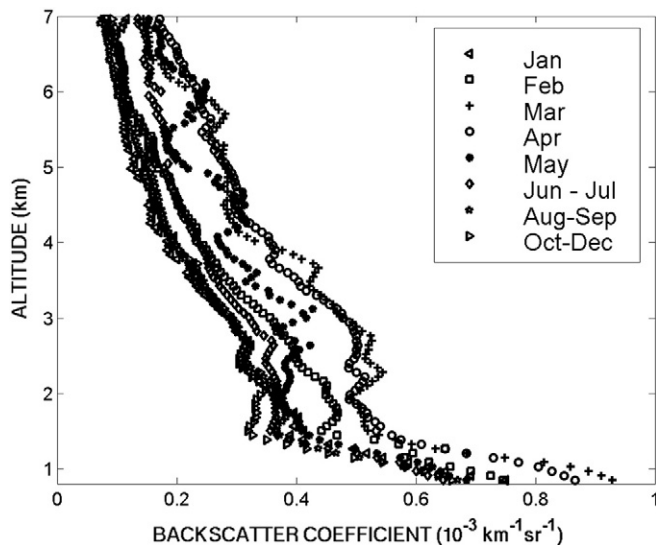


Fig. 16. Monthly and bi-monthly averaged vertical profiles of aerosol volume backscatter coefficient  $\beta_{bs}(0.532 \mu\text{m})$  obtained from the KARL lidar measurements conducted at Ny-Ålesund (AWIPEV station) from 1 November, 2012, to 31 October, 2013.

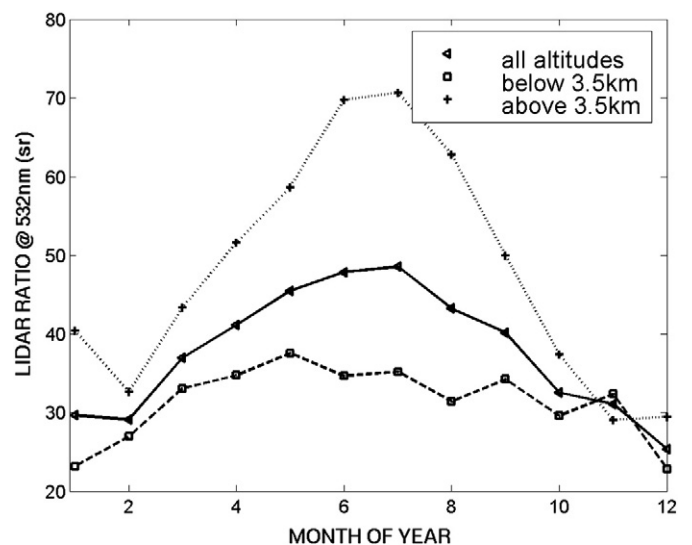


Fig. 18. Time-patterns of the monthly average values of the lidar ratio  $S_a(0.532 \mu\text{m}) = \beta_{ext}(0.532 \mu\text{m})/\beta_{bs}(0.532 \mu\text{m})$  calculated over the whole altitude range (triangles) and the altitude sub-ranges  $z < 3.5 \text{ km}$  (squares) and  $z > 3.5 \text{ km}$  (+), as obtained from the KARL lidar measurements conducted at Ny-Ålesund (AWIPEV station) from 1 November, 2012, to 31 October, 2013.

To quantify the direct radiative forcing of Arctic haze, it is very important to know the morphological and optical features of atmospheric aerosols, as well as the multimodal size-distribution, the refractive index and the particle shape. The ratio of the perpendicular to parallel polarised backscatter returns from aerosols at a certain wavelength  $\lambda$  gives the volume depolarisation ratio  $\delta_v(\lambda)$ , which provides an effective range-resolved method of determining whether the laser pulse has been backscattered by spherical or non-spherical aerosols (Winker et al., 2009). Bearing in mind that spherical particles do not depolarise the incoming solar radiation, the scatter plot of the monthly (from January to May) and bi-monthly (from June to December) averaged values of depolarisation ratio percentage are shown in Fig. 19 versus the aerosol backscatter coefficient  $\beta_{bs}(0.532 \mu\text{m})$ , as obtained from the KARL lidar measurements conducted from early November 2012 to late October 2013. Generally quite low values of aerosol depolarisation ratio  $\delta_v(0.532 \mu\text{m})$  have been found (appreciably lower for instance than those of desert dust), with the lowest values in January, and values ranging from 2.0% to 2.6% in October–December, over the range of  $\beta_{bs}(0.532 \mu\text{m}) < 4.5 \times 10^{-4} \text{ km}^{-1} \text{ sr}^{-1}$ . Remarkably higher depolarisation values, greater than 2.6%, have been found during the maximum of the haze season, in March and April, for values of  $\beta_{bs}(0.532 \mu\text{m})$  ranging from  $4.0 \times 10^{-4}$  to  $5.5 \times 10^{-4} \text{ km}^{-1} \text{ sr}^{-1}$ . This means that the Mie theory, while being a fair assumption to model the forcing of Arctic aerosol during most of the year, is less accurate during spring time.

Lidar measurements were taken at the coastal Antarctic stations of Syowa, Mario Zucchelli, McMurdo and Dumont d'Urville ( $66^\circ 40' \text{ S}$ ,  $140^\circ 01' \text{ E}$ ), and at the Antarctic Plateau sites of Dome Concordia and South Pole over the past decades (see the Antarctic map in Fig. 2), to monitor the microphysical parameters of clouds at various altitudes (for cloud climatology studies), and only occasionally to measure the vertical profile of the tropospheric aerosol scattering coefficient  $\beta_{ext}(0.532 \mu\text{m})$ . It was found in general that the cloud-free vertical profile of aerosol scattering does not exhibit particularly dense layers near the surface, but shows that  $\beta_{ext}(0.532 \mu\text{m})$  decreases rapidly with height, to reach the free troposphere “background aerosol” conditions immediately above the marine PBL. The first lidar measurements were conducted during the 1974/1975 austral summer at South Pole, where regular measurements have also been carried out with a micropulse system since 1999, mainly to study the microphysical characteristics

of diamond dust and blowing snow events. Ground-based lidar measurements have also been regularly conducted at Dome Concordia since 2007, by using the elastic-backscatter and depolarisation lidar system of the IFAC-CNR Institute (Florence, Italy). Analysis of these data revealed that “diamond dust” ice-crystals are often present during windy conditions at this remote site, within the boundary layer of 100–200 m depth, while aerosols contribute to yield slowly decreasing values of  $\beta_{sca}(0.532 \mu\text{m})$  with height, until rapidly reaching the background conditions of the free troposphere.

Diamond dust episodes were also frequently observed over the Arctic Ocean. Ground-based lidar and radar were used for this purpose during the Surface Heat Budget of the Arctic Ocean (SHEBA) programme, determining the physical characteristics of diamond dust ice-crystals and assessing the surface radiative effects induced by such particles under cloud-free sky conditions. Examining a set of 188 diamond dust or ice-crystals episodes over the western Arctic Ocean between November 1997 and May 1998, Intrieri and Shupe (2004) found that diamond dust episodes covered about 13% of the time between November and mid-May over the Arctic Ocean and were never observed from mid-May to October. Lidar measurements highlighted that the diamond dust vertical depth varied from 100 m to 1000 m on the various cloud-free sky days, although it was most frequently observed to involve the lower 250 m of the troposphere on average, thus contributing to induce only small radiative effects on the sea ice surface.

Airborne lidar measurements of vertical profiles of aerosol extinction and backscatter coefficients were conducted in the Arctic, over the Svalbard area in spring 2000, 2004 and 2007, during the ASTAR (Arctic Study of Aerosol Clouds and Radiation) campaigns, together with complementary ground-based lidar measurements at Ny-Ålesund (Spitsbergen). The ASTAR 2000 campaign ran from 12 March until 25 April 2000 with extensive flight operations over the Svalbard region using the AWI aircraft POLAR 4. Simultaneous ground-based measurements were conducted at Ny-Ålesund (at both German Koldewey and Japanese Rabben stations as well as at the Zeppelin station). Vertical profiles of various aerosol parameters were measured during the campaign and provided evidence of the strong temporal variability of the Arctic spring aerosol with height. A strong haze event occurred between 21 and 25 March, in which AOT measured from ground-based observation was 0.18, i.e. largely greater than the aerosol background value measured in summer. The airborne measurements made on 23 March showed a high aerosol layer with an extinction coefficient of  $0.03 \text{ km}^{-1}$  or more up to 3 km. The chemical analyses of airborne measurements showed that such an aerosol transported from anthropogenic sources mainly consisted of sulphate, soot and sea-salt particles (Yamanouchi et al., 2005). Lidar measurements of 532/355 nm colour ratio were obtained by Lampert et al. (2009) during the ASTAR 2007 experiment, indicating the presence of particles with an effective diameter  $< 5 \mu\text{m}$ . However, Lampert et al. (2010) found rather low Arctic haze levels in spring 2007, examining lidar measurements of cloud and aerosol layers. As pointed out by Hoffmann et al. (2009), the Arctic haze optical thickness  $\tau(0.50 \mu\text{m})$  measured during such a seasonal period was evaluated to vary mainly from 0.05 to 0.08, compared to a 14-year average value of 0.10. The PBL extended up to 2.5 km altitude and predominantly contained well-hydrated particles, such as local sea-spray derived sulphates.

Various airborne lidar measurements were conducted as part of the POLARCAT programme during the 2007–2008 International Polar Year, to define the aerosol radiative characteristics. In particular, analysing the backscatter measurements provided by the LEANDRE multi-channel lidar mounted on the ATR-42 aircraft, cases of aerosol transport from Europe and Eastern Asia were monitored in April 2008 by de Villiers et al. (2010). These studies showed that anthropogenic aerosols originating in Europe exhibited in general smaller sizes than Asian particles within the PBL below a height of 0.8 km and within layers at heights ranging from 2.8 to 4.5 km, consisting mainly of biomass burning substances and urban/industrial particulate matter, with aerosol

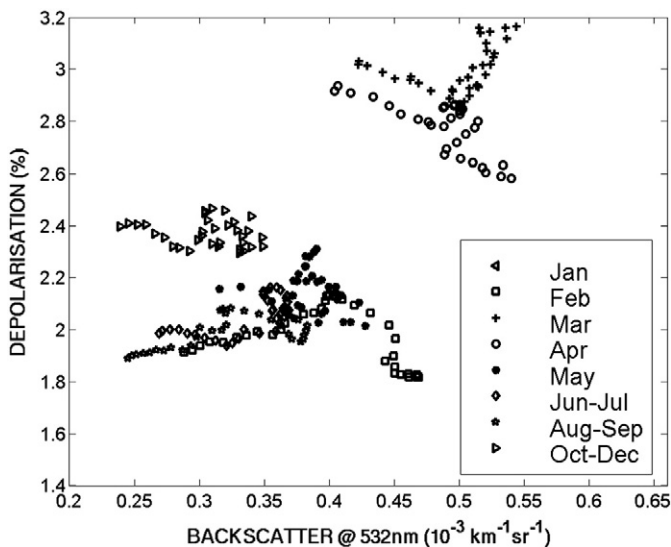


Fig. 19. Scatter plots of the monthly and bi-monthly averaged values of the depolarisation ratio (%) versus the aerosol backscatter coefficient  $\beta_{bs}(0.532 \mu\text{m})$ , as obtained from the KARL lidar measurements conducted at Ny-Ålesund (AWIPEV station) from 1 November, 2012, to 31 October, 2013.



backscatter coefficient  $\beta_{bs}(0.532 \mu\text{m})$  ranging from  $1.2 \times 10^{-3}$  to  $2.2 \times 10^{-3} \text{ km}^{-1} \text{ sr}^{-1}$ , and depolarisation ratio varying from 1.6% to 2.1% (with standard deviations of 0.3% on average). Conversely, the Asian dust plume observed in April 2008 was estimated to contain larger particles, presenting some well-defined aerosol layers at altitudes from 1.7 to 5.6 km, with  $\beta_{bs}(0.532 \mu\text{m})$  varying from  $1.6 \times 10^{-3}$  to  $3.9 \times 10^{-3} \text{ km}^{-1} \text{ sr}^{-1}$ , and depolarisation ratio values equal to 2.0% (smoke particles), 3.0–5.0% (clean continental aerosol), 8.0% (dust), and 4.0–10.0% (polluted dust).

The above results were obtained using also the Level 2.0 products given by the CALIOP lidar mounted on the CALIPSO satellite, which was launched in April 2006 (Winker et al., 2009, 2010) as a part of the A-train constellation of satellites, and has an orbit inclination of  $98.2^\circ$ , thus providing coverage to  $82^\circ$  latitude. This wide coverage has proven immensely important in polar regions, where ground-based installations are few and far between. The CALIOP lidar operates at wavelengths of 0.532 and 1.064  $\mu\text{m}$ , with a depolarisation ratio measured at 0.532  $\mu\text{m}$ , and was used to characterise the various aerosol types by assuming in such an approach a set of values of lidar ratios  $S_a(0.532 \mu\text{m})$  and  $S_a(1.064 \mu\text{m})$  equal to 20 and 45 sr for clean marine aerosol, 35 and 30 sr for clean continental aerosol, 40 and 30 sr for dust, 65 and 30 sr for polluted dust, 70 and 30 sr for polluted continental aerosol, and 70 and 40 sr for combustion smoke particles, respectively (Winker et al., 2009).

A first airborne campaign referred to as the Polar Airborne Measurements and Arctic Regional Climate Model Simulation Project (PAMARCMiP) took place during April 2009 in the Arctic, using a pair of downward-looking lidars, a depolarisation aerosol lidar and a tropospheric ozone DIAL mounted onboard the Polar 5 research aircraft of the Alfred Wegener Institute (AWI) for Polar and Marine Research (Germany). On the basis of the evaluations made by Rogers et al. (2011), it can be assumed that a relative 3% bias of aerosol backscatter coefficient  $\beta_{bs}(0.532 \mu\text{m})$  was made on average, due to a wrong assumption of the Rayleigh backscatter coefficient used to correct the overall lidar backscatter coefficient. A series of flights was conducted from Longyearbyen (Svalbard) across the western Arctic to Barrow (Alaska), reaching Station Nord (Greenland), Alert, NP-36 (at  $88^\circ 40' \text{ N}$  latitude), Eureka, Resolute Bay, Sachs Harbor, Inuvik, and Fairbanks, while complementary ground-based lidar measurements were regularly conducted at Ny-Ålesund, Eureka and Barrow (Stone et al., 2010). Significant aerosol backscatter and extinction effects were measured over the entire region, mainly caused by haze particles with diameters ranging from 0.13 to 0.20  $\mu\text{m}$ . The PAMARCMiP lidar measurements showed that the aerosol extinction coefficient decreased in general with height from the surface to the top-level of the thermal inversion layer, found to be on average equal to 4 km, and often presented a secondary peak above. A second PAMARCMiP airborne campaign was conducted with the Polar 5 aircraft during April 2011, following the route from Longyearbyen to Barrow, flying over Station Nord, Alert, Eureka, Resolute Bay and Inuvik (Herber et al., 2012). During both campaigns, black carbon was observed at all altitudes sampled but at relatively low concentrations compared with historical values.

A climatological study of Arctic aerosols was made by Devasthale et al. (2011) examining the CALIOP measurements recorded from June 2006 to May 2010. The study showed that the bulk of the aerosol particles are confined within the first 1000 m of the troposphere, from about 65% of cases in winter to 45% in summer, while the rest is mainly suspended within the middle troposphere, at altitudes ranging from 3 to 5 km, especially in spring. The relative occurrences of aerosol types in the vertical profiles show that clean continental aerosol is the largest contributor in all seasons except in summer, while polluted continental aerosols are the second largest contributor to the total number of observed aerosol layers in winter and spring, and clean marine aerosol is the second largest contributor in summer and autumn. The average vertical profile of aerosol extinction coefficient was found to exhibit a pronounced peak at heights of about 0.4–0.7 km. Associated with the

intrusions from mid-latitudes, polluted continental and smoke aerosols presented much broader distributions of optical and geometrical thicknesses, appearing to be more often optically thicker and higher up in the troposphere.

## 5. Airborne and satellite measurements

### 5.1. Basic remarks

Airborne sun-photometry employs ground-based techniques adapted to the special requirements (notably solar tracking) of an aircraft environment. Relatively frequent measurements can be made during ascending or descending profiles to achieve vertically stratified AOT measurements, which are sensitive to the aerosol vertical structure and can be converted to volume extinction coefficient profiles, which are analogous to the aerosol backscatter coefficient profiles derived from lidar measurements and shown in Fig. 16 (see Section 4). It is also possible to carry out measurements onboard airplanes flying above and below pollution plumes. These aircraft measurements offer the possibility of surveying large areas in relatively short time-periods, which is not possible, e.g., for ship-borne measurements. In particular, airborne measurements of this kind were made during the PAMARCMiP airborne campaign of April 2009 (Stone et al., 2010), in which various airborne lidar systems and a multi-wavelength sun-photometer were mounted onboard the AWI Polar 5 research aircraft to perform numerous measurements of volume aerosol scattering and extinction coefficients were conducted over the wide area from Svalbard across the western Arctic to Barrow, from the European to the Alaskan Arctic, and from sub-Arctic latitudes to near the Pole. The sun-photometer measurements were performed using a 8-channel sun-photometer system manufactured by NOAA/GMD (Boulder, Colorado, USA) in cooperation with ISAC-CNR (Bologna, Italy), and equipped with narrow-band visible and near-IR channels centred at wavelengths ranging from 0.355 to 1.064  $\mu\text{m}$ , while the lidar measurements were conducted using a pair of downward-looking lidars, a depolarisation aerosol lidar and a tropospheric ozone DIAL. Additional independent in-situ measurements of particle size-distribution were also made onboard the AWI Polar 5 aircraft, and light extinction data were derived from the airborne lidar measurements to investigate the spectral effects produced by haze particles.

The measurements revealed that the spatial variations in  $\tau(\lambda)$  observed during the most turbid period of the 2009 haze season were closely related to the atmospheric circulation patterns regulated by a dominant airflow from Eurasian anthropogenic sources. In addition, lidar observations showed the presence of elevated aerosol layers, as shown at Ny-Ålesund by Treffeisen et al. (2007) in early May 2006 during a transport event of biomass burning aerosols from agricultural fires in eastern Europe, and by Stock et al. (2012) in March 2008 during a BFF smoke pollution event over the European Arctic region.

Background values of  $\tau(0.50 \mu\text{m})$  not exceeding 0.06 were determined in the most remote areas, while haze values of  $\tau(0.50 \mu\text{m})$  varying from 0.12 to around 0.35 were measured, with the highest values found in the Beaufort Sea region towards the end of April. Such values of  $\tau(\lambda)$  were anomalously high compared with those measured in the previous three years, because of the transport of haze particles from the industrial regions in Europe and Northern Asia. Arctic haze particles were frequently found to be concentrated within and just above the surface-based temperature inversion layer, showing in general bimodal size-distribution features, consisting of an accumulation mode of moderately small (water-soluble) particles and an additional mode mainly composed of insoluble coarse particles. In addition, the in-situ sampling and optical measurements revealed a marked decrease in the mean particle size with increasing altitude from the surface to 4 km, yielding values of the Ångström exponent  $\alpha(0.412\text{--}0.675 \mu\text{m})$  varying from 1.40 to 1.70. The airborne measurements showed that black carbon (BC) was highest near the North Pole, suggesting long-range transport

from combustion sources. However, the BC concentration measurements performed near the surface were nearly an order of magnitude lower than those reported from similar campaigns in the 1980s. Enhanced opacity at higher altitudes during the campaign was attributed to an accumulation of industrial pollutants in the upper troposphere, consisting of residual aged aerosol and soot particles originating from coal burning in China, in combination with volcanic aerosol resulting from the March–April 2009 eruptions of Mount Redoubt in Alaska and perhaps minor contributions from aircraft emissions. The Arctic haze particles observed during April 2009 were estimated to have reduced the net short-wave irradiance by  $-2$  to  $-5 \text{ W m}^{-2}$ , resulting in a slight cooling of the surface. Examining the data recorded during the second PAMARCMiP airborne campaign in April 2011, and some aerosol measurements coordinated with satellite flyovers of NASA's CALIPSO mission, Herber et al. (2012) found that such satellite-borne data can be useful to validate aerosol retrievals from the lidar and sun-photometer measurements made onboard the Polar 5 aircraft.

Even larger areas than those covered by airborne sun-photometer campaigns can be monitored by means of satellite observations. The retrieval of aerosol properties from satellite-based measurements is an ill-posed problem. The satellite retrieved aerosol optical thickness over bright surfaces such as snow and ice is often biased and leads to errors when estimating aerosol-radiation interactions (IPCC, 2013). Polar-orbit satellite-mounted sensors like MODIS (Moderate Resolution Imaging Spectroradiometer) and MERIS (Medium Resolution Imaging Spectrometer) utilise multi-spectral information to characterise surface properties. The NASA/MODIS “dark-target” (DT) approach developed for the retrieval of aerosol properties uses the  $2.1 \mu\text{m}$  band to estimate the reflectance in visible bands (Kaufman et al., 1997). The empirical relationships between the surface reflectance of visible channels and  $2.1 \mu\text{m}$  channel were improved by considering the effect of geometry and surface types (Levy et al., 2007), while information on global aerosol properties was determined as a function of location and season by performing cluster analysis of in-situ measurements (Levy et al., 2010). The major limitation of the MODIS DT algorithm is that no retrievals are performed when the surface reflectance of the  $2.1 \mu\text{m}$  channel is higher than 0.25 (Levy et al., 2007). For the retrieval over bright surfaces, such as desert and urban regions, Hsu et al. (2004) developed the Deep Blue (DB) algorithm utilizing the fact that the surface is much darker in the short blue spectral channels compared with longer wavelengths. The second generation of DB algorithm, the so-called Enhanced Deep Blue algorithm, improved estimates of the surface reflectance, aerosol model selection and cloud-screening schemes (Sayer et al., 2012; Hsu et al., 2013). The current MODIS Collection 6.0 AOT product is created from three separate retrieval algorithms for different surface types (Levy et al., 2013): they are two DT algorithms for dark ocean surface as well as the vegetated/dark-soiled land and a DB algorithm over desert/arid land. MODIS Collection 6 also provides a 3 km AOT product compared to Collection 5 (Remer et al., 2013). The Bremen AErosol Retrieval (BAER) algorithm for MERIS (von Hoyningen-Huene et al., 2003, 2011) utilises the Normalized Difference Vegetation Index (NDVI). Polar-orbit satellites with multi-view observations such as AATSR (Advanced Along Track Scanning Radiometer) (Curier et al., 2009) and MISR (Multi-angle Imaging Spectroradiometer) (Diner et al., 2005a) make use of the Bidirectional Reflectance Distribution Function (hereinafter referred to as BRDF) surface properties to constrain the ill-posed inverse problem. A time series method is the most popular aerosol retrieval method for geostationary satellite based on the assumption that the surface reflectance does not change significantly during a short period of time (Knapp et al., 2002; Govaerts et al., 2010; Mei et al., 2012). The retrievals based on POLDER (Polarization and Directionality of the Earth's Reflectances) (Deuzé et al., 2001; Dubovik et al., 2011) intensity and degree of polarisation measurements provide more accurate AOT products with the advantage that the contribution of land surfaces to the degree of polarisation at the TOA is generally smaller in the visible as compared

to the contribution of the underlying surface to the light intensity as measured on a satellite.

Among the various satellite-based observations, those provided by MODIS (Justice et al., 1998) mounted on the Terra and Aqua platforms are particularly useful for evaluating the AOT features in the polar regions, over the ocean and ice-free land surfaces, and studying aerosol climatology associated with the sources, transport and sinks of specific aerosol types (e.g., sulphates and biomass burning smoke particles). The twin MODIS sensors have been flying on the Terra platform since 2000 and on the Aqua platform since 2002, giving a large data-set of aerosol products using a number of algorithms over the past decades to retrieve columnar aerosol parameters over sea and land (Kaufman et al., 1997; Tanré et al., 1997; Hsu et al., 2004; Remer et al., 2005; Levy et al., 2013; Xue et al., 2014). To define the average seasonal maps of  $\tau(0.55 \mu\text{m})$ , we downloaded data-sets of MODIS/Terra and MODIS/Aqua monthly Level-3 data (Atmosphere Monthly Global  $1 \times 1$  Degrees Products MOD08\_M3.051 and MYD08\_M3.051, for the Terra and Aqua platforms, respectively) from the Giovanni website (<http://disc.sci.gsfc.nasa.gov/giovanni>). These had been collected for cloud-free atmospheric conditions over the eight years from January 2005 to December 2012, at Arctic latitudes  $\geq 67^\circ \text{ N}$  and Antarctic latitudes  $\geq 62^\circ \text{ S}$ . The cloud-screened Arctic AOT data-set was divided into seasonal sub-sets of  $\tau(0.55 \mu\text{m})$  for spring (March to May) and summer (June to August), separately for Terra and Aqua observations. The seasonal average maps of Level-3 AOT  $\tau(0.55 \mu\text{m})$  derived from MODIS/Aqua and MODIS/Terra are separately shown in Fig. 20, for  $1^\circ \times 1^\circ$  pixels over oceans and land areas not covered by snow and ice. The values of  $\tau(0.55 \mu\text{m})$  in the summer months are mainly lower than 0.15, with some areas characterised by average values ranging from 0.15 to 0.30 over the Central and Western Siberian Sea, and the Chukchi Sea, as well as over the Beaufort Sea, presumably due to the transport of BFF aerosol from Siberia and North America, respectively. The spring average values of  $\tau(0.55 \mu\text{m})$  range mainly from 0.10 to 0.25, with peaks of more than 0.30 in the Siberian, North American and North European sectors, associated with dense Arctic haze transported from the anthropogenic mid-latitude sources. These findings closely agree with the results obtained from the ground-based sun-photometer measurements conducted at coastal sites (Fig. 8a) and from the ship-borne AERONET/MAN measurements (Fig. 8b). Fig. 20 also shows that AOT cannot be retrieved from the MODIS data using the operational MODIS algorithm over Greenland and the North Pole in both spring and summer, and over large regions of Northern America and Siberia in spring, because of the high reflectance of the surfaces covered by sea ice and snow and also because of generally small values of AOT in these areas.

Reliable maps of exponent  $\alpha$  cannot be retrieved from MODIS data over both land and ocean surfaces because of the low values of AOT in the polar regions and the relevant uncertainties affecting the MODIS aerosol products (Mishchenko et al., 2010; Kahn et al., 2011). In particular, Levy et al. (2013) determined the Collection 6 MODIS aerosol products to retrieve AOT and aerosol size-parameters from MODIS-observed spectral reflectance data and found that the Ångström exponent product over land cannot be reliably used. These findings were confirmed by Mielonen et al. (2011) who stated that MODIS data do not provide quantitative information about aerosol size and parameter  $\alpha$  over land. Similarly, as a result of a validation study of Collection 5 MODIS Level-2 Aqua and Terra AOT and  $\alpha$  products over ocean, Schutgens et al. (2013) found that these products exhibit significant biases due to wind speed and cloudiness of the observed scene, being significantly affected by AOT and  $\alpha$  random errors due to cloud fraction contributions.

On the basis of these results, we have decided to examine here only the MODIS AOT data and exclude from the present analysis the MODIS  $\alpha$  products obtained over snow- and ice-free land and ocean regions, since they were presumably affected by considerable uncertainties arising from: (i) the presence of cloud-fractions within the  $1^\circ \times 1^\circ$  pixels that cannot be correctly evaluated, and (ii) the variability of AOT at visible



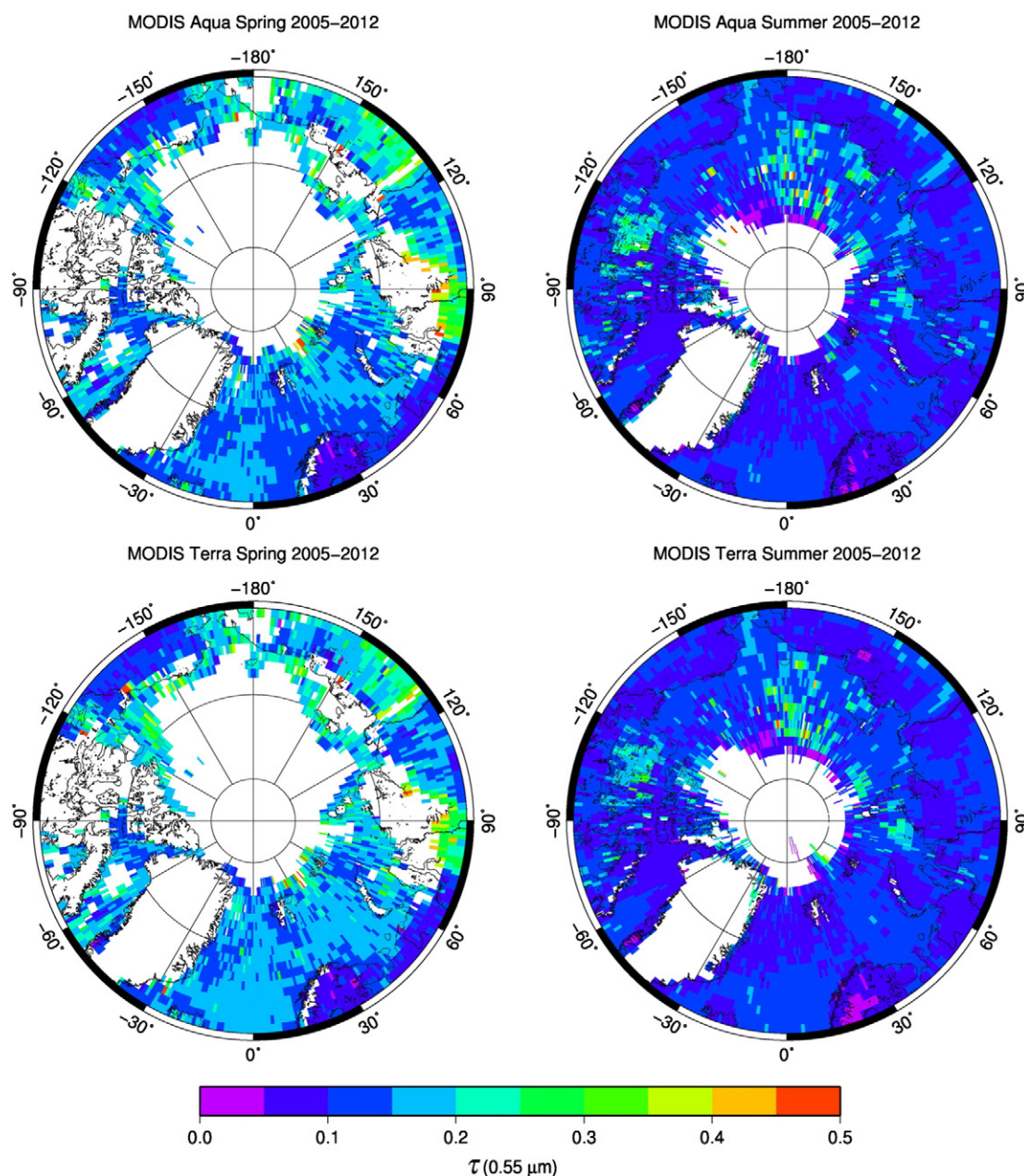


**Fig. 20.** Arctic maps of the seasonal average Level-3 aerosol optical thickness  $\tau(0.55 \mu\text{m})$  derived from MODIS/Aqua (upper part) and MODIS/Terra (lower part) satellite data recorded from 2005 to 2012 during the spring (left-hand side) and summer (right-hand side) 3-month periods.

and near-infrared wavelengths, due to cloud extinction effects, which may efficiently contribute to lower exponent  $\alpha$ . On the basis of the AERONET/MAN measurements, this parameter was evaluated to range from less than 1.00 to around 1.75 over the Arctic Ocean sectors in spring and summer, and from less than 0.50 to about 2.00 in Antarctica, with in general lower values over the off-shore areas far from the Antarctic coasts.

The Antarctic aerosol data-set downloaded from the Giovanni website over the latitude range  $\geq 62^\circ \text{S}$  covers not only the land region of the Antarctic continent but also the off-shore ocean areas no further than 1000 km from the coasts. Only the MODIS/Aqua and MODIS/Terra data collected from December to February were separately examined to determine the maps of average  $\tau(0.55 \mu\text{m})$ , limited in practice to the oceanic areas only (Fig. 21). The results indicate that such seasonal average values of  $\tau(0.55 \mu\text{m})$  are lower than 0.10 over all ocean areas close to the Antarctic coasts and sometimes can exceed 0.10 over the off-shore areas, in close agreement with the values derived from

ground-based sun-photometer measurements at coastal Antarctic sites (Fig. 13a) and from AERONET/MAN measurements (Fig. 13b).

Fig. 21 also shows that no useful information is available from MODIS observations over the interior of Antarctica when using the traditional retrieval procedures. The retrieval of  $\tau(\lambda)$  over a bright surface is indeed a very difficult task, because it is hard to separate the radiance contributions by the reflecting surface and atmospheric aerosol back-scattering to the overall radiance observed by a satellite-borne sensor at the TOA-level, especially for the very large solar zenith angles typical of polar latitudes. Mei et al. (2013a) overcame the above difficulties by following a synergetic approach based on the use of both MODIS/Terra and MODIS/Aqua data, together with: (i) the a-priori assumption of aerosol optical parameters retrieved over snow made with the Aerosol Properties Retrieval over Snow (APRS) algorithm, and (ii) an appropriate model of the BRDF reflectance representing snow-covered surfaces. The APRS algorithm was based on the operational bi-angle approach proposed by Xue and Cracknell (1995) to retrieve non-absorbing



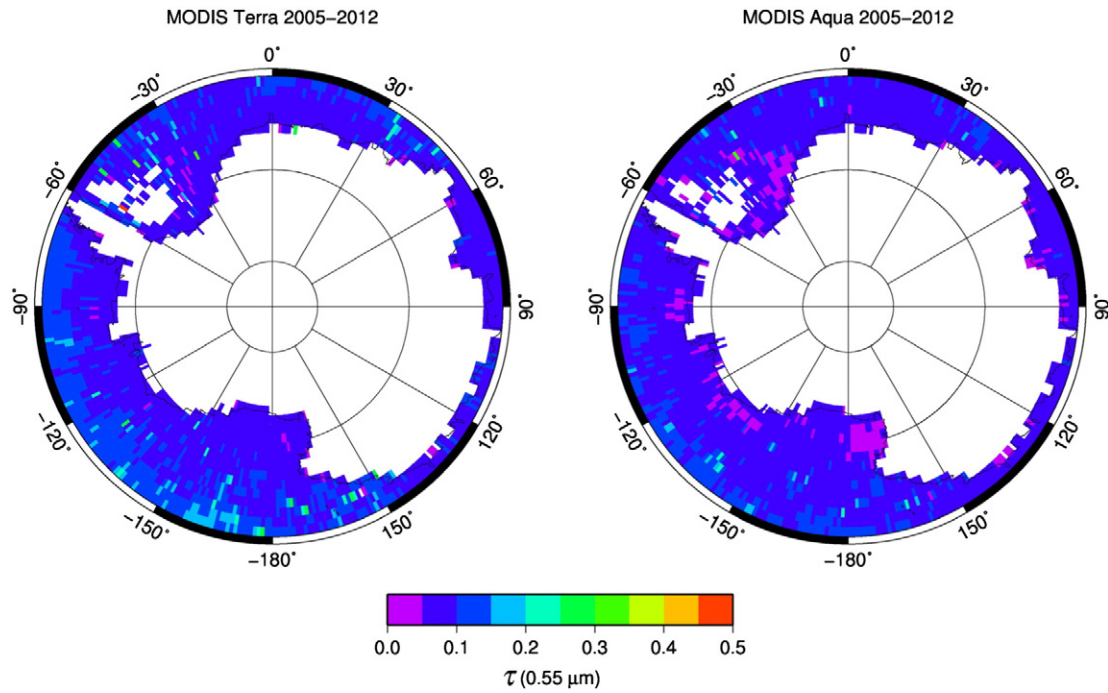


**Fig. 21.** Antarctic maps of the austral summer Level-3 aerosol optical thickness  $\tau(0.55 \mu\text{m})$  derived from the MODIS/Terra (left-hand side) and MODIS/Aqua (right-hand side) satellite data recorded over the 2005–2012 period.

aerosol extinction parameters over land surfaces (Tang et al., 2005; Wang et al., 2012), in which particulate absorption was considered, and a two-stream approximation was adopted. This new algorithm was found reliable by Mei et al. (2013a) by means of an extended comparison between the values of  $\tau(0.55 \mu\text{m})$  retrieved from MODIS data and simultaneous AERONET measurements made at six high-latitude Arctic stations (Andenes, Barrow, Ittoqqortoormiit, OPAL, Thule, and PEARL) in April 2010 and April 2011 (i.e., during periods in which Arctic haze frequently occurs). A regression line with slope coefficient equal to +0.764 was found by applying the least squares method to a set of 70 MODIS retrieved values of  $\tau(0.55 \mu\text{m})$  obtained with a  $10 \text{ km} \times 10 \text{ km}$  resolution plotted versus the corresponding AERONET measurements,

with a regression coefficient equal to +0.81 and a root mean square error  $\text{RMSE} = 0.079$ . In particular, comparing the MODIS retrieved values of  $\tau(0.55 \mu\text{m})$  with the AERONET measured values at the above stations, Mei et al. (2013a) found relative discrepancies between them ranging from a few percent to more than 30% in cases with  $\tau(0.55 \mu\text{m}) > 0.20$ , presumably associated with strong Arctic haze extinction.

These results demonstrate the considerable potential of the APRS algorithm to retrieve  $\tau(\lambda)$  at visible wavelengths over the Arctic, for highly reflective snow/ice surfaces and large solar zenith angles, as can be seen in the maps of  $\tau(0.55 \mu\text{m})$  derived from the MODIS/Aqua observations made on 29 March and 3 May in 2006 (Fig. 22), using the method of Mei et al. (2013a).

MODIS/AQUA AOT [550nm] 29 March, 2006

MODIS/AQUA AOT [550nm] 3 May, 2006

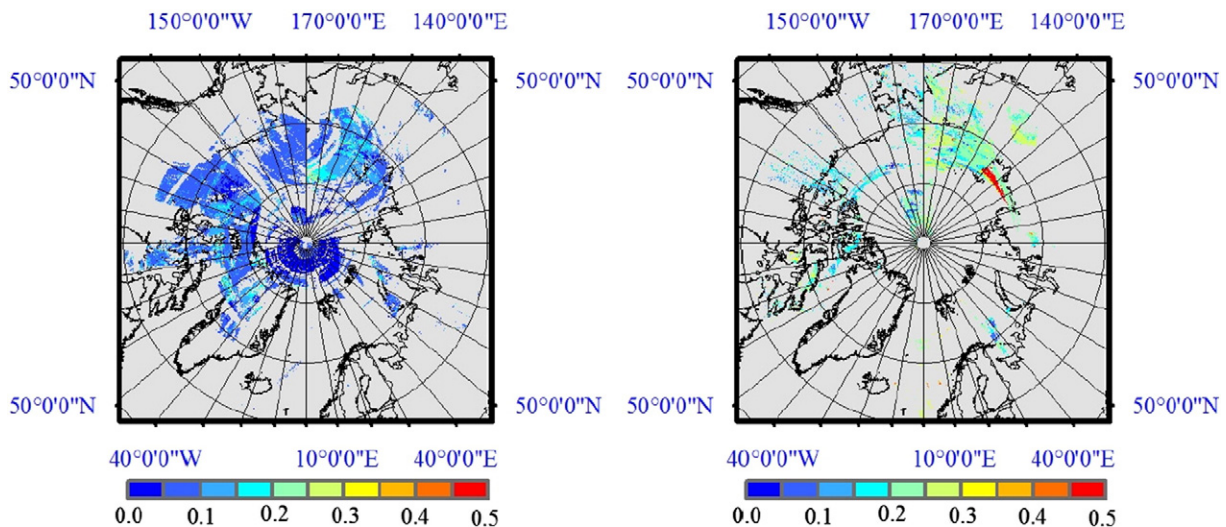


**Fig. 22.** Maps of aerosol optical thickness  $\tau(0.55 \mu\text{m})$  derived over the Arctic region from the MODIS/Aqua observations made on 29 March, 2006 (left-hand side) and 3 May, 2006 (right-hand side) using the method of Mei et al. (2013a).

## 5.2. Aerosol optical thickness retrievals over snow and ice using backscattered solar light

Of particular relevance for remote sensing applications in polar regions, are the multiple-view (MISR) and double-view (AATSR) sensors. The measurements made with these instruments allow the contribution from underlying bright surfaces (e.g., snow and ice) to be removed, assuming that the atmosphere is the same for observations made at different angles, in all cases where the atmosphere is not filled with broken clouds. MISR is a sensor built by the Jet Propulsion Laboratory (JPL) and hosted on the NASA Terra platform, which was launched on 18 December 1999, and became operational in February 2000. It was designed to measure the intensity of solar radiation reflected by the surface-atmosphere system in various directions and spectral bands, with the main mission of measuring the intensity of solar radiation reflected and absorbed by the Earth. The device is composed of nine separate digital cameras, each with four spectral bands (blue, green, red, and near-infrared), that view the Earth at nine different angles (Diner et al., 1998). The algorithms for AOT retrieval from the MISR observations are discussed in Martonchik et al. (1998a,b) and Diner et al. (2005a), and further assessed by Martonchik et al. (2002) and Kahn et al. (2005, 2010). Examining the MISR monthly Level-3 data (Monthly Global  $0.5^\circ \times 0.5^\circ$  Aerosol Product, MIL3MAE.004) recorded during the 2005–2012 period, the regional maps of monthly average AOT were determined in the present study, over the Arctic region for latitudes  $\geq 67^\circ$  N, and the Antarctic region for latitudes  $\geq 62^\circ$  S. The monthly average values of  $\tau(0.55 \mu\text{m})$  collected over the Arctic region under cloudless sky conditions were separated into a pair of seasonal subsets for spring (March–April–May) and summer (June–July–August), from which the seasonal average maps of  $\tau(0.55 \mu\text{m})$  shown in Fig. 23 were obtained. It can be seen that these results are very similar to those retrieved from the MODIS data in Fig. 20, with spring average values of  $\tau(0.55 \mu\text{m})$  varying mainly from 0.10 to 0.25, and being higher than 0.20 (and sometimes exceeding 0.30) over large areas of Central and Eastern Siberia as in the North American sector, presumably associated with dense Arctic haze transport episodes. The average summer values of  $\tau(0.55 \mu\text{m})$  were found to mainly range from 0.05 to 0.15, showing similar features to those detected by MODIS observations. With regard to this, it is worth mentioning that Campbell et al. (2012) examined (i) MODIS and MISR observations made over the Arctic regions in 2007, obtaining estimates of  $\tau(0.55 \mu\text{m})$  all lower than 0.10, and (ii) a CALIOP data-set collected in 2007, determining mean day-time and night-time values of  $\tau(0.532 \mu\text{m})$  all lower than 0.15. In addition, examining the CALIOP data recorded over the Arctic in 2008, Winker et al. (2013) obtained mean cloud-free day-time values of  $\tau(0.532 \mu\text{m})$  mainly lower than 0.05 and mean cloud-free night-time values of  $\tau(0.532 \mu\text{m})$  not exceeding 0.10 in March–May and September–February. In particular, they determined average values of  $\tau(0.532 \mu\text{m})$  from the CALIOP observations made from 2007 to 2011 that were lower than: (i) 0.02 over inner Greenland, (ii) 0.08 over the GNS sector surrounding the Svalbard region, (iii) 0.12 over the Scandinavian area, (iv) 0.12 over the Western Siberian Sea sector, (v) 0.05 over the Eastern Siberian Sea sector, and (vi) 0.06 over the North American sector of the Arctic Ocean. These data are in good agreement with ground-based sun-photometer measurements (Figs. 3–8) and AERONET/MAN ship-borne measurements (Figs. 8b and 14), which showed that  $\tau(0.50 \mu\text{m})$  mainly varies from 0.08 to 0.16 in spring and from 0.04 to 0.10 in summer.

The same procedure was also followed in the analysis of MISR data recorded over Antarctica during the austral summer from 2005 to 2012 (Fig. 23), which indicates that the seasonal average values of  $\tau(0.55 \mu\text{m})$  are lower than 0.10 over the greater part of the coastal ocean areas around Antarctica and vary mainly from 0.10 to 0.25 over the off-shore areas very far from the coasts, due to effective sea-salt production by strong winds. These features are very similar to those obtained from MODIS observations (Fig. 21) and those derived from the

AERONET/MAN measurements carried out in the coastal and off-shore ocean areas surrounding the Antarctic continent (Fig. 13b).

The AATSR sensor is a dual-view (nadir and  $55^\circ$  forward) radiometer on board the European Space Agency (ESA) Environmental Satellite (ENVISAT), which was launched in March 2002 and is one of the satellite instruments designed for providing a well-calibrated long-term global data-set of satellite data for climate research (Grey and North, 2009). ENVISAT was on a sun-synchronous orbit with an equator passing time of about 10 am. AATSR has a ground pixel resolution which is equal to  $1 \times 1 \text{ km}^2$  at nadir and a swath width of 500 km, thus taking about six days to achieve full global coverage (three days at mid-latitudes). Observations in both views are made at seven wavelengths:  $0.55 \mu\text{m}$ ,  $0.66 \mu\text{m}$ ,  $0.87 \mu\text{m}$ ,  $1.6 \mu\text{m}$ ,  $3.7 \mu\text{m}$ ,  $11 \mu\text{m}$  and  $12 \mu\text{m}$ , the spectral resolution of visible channels is approximately 20 nm, which avoids atmospheric water vapour absorption regions in the electromagnetic spectrum. Contact was lost with ENVISAT on April 2012 after 10 years of service. The follow-up SLSTR mission as currently foreseen on Sentinel-3 will ensure the continuity of the multi-view-angle method into the future.

The reflectance at the TOA-level can be described as the sum of the atmospheric path reflectance (black surface reflectance) and the atmosphere–surface interaction (Kaufman et al., 1997). With the use of AATSR dual-view observations, the ratio between observations in the forward and nadir directions can be determined by calculating the difference between TOA reflectance and atmospheric path reflectance in both directions and taking features of the total atmospheric transmission into account (Istomina et al., 2010; Mei et al., 2013b). It is worth mentioning that the ratio of both AATSR directional observations is not sensitive to the snow albedo, which reduces the high snow albedo effect on AOT retrieval over the Arctic region. For pure snow, Istomina et al. (2009) used an analytical snow BRDF model to estimate the ratio of both directional observations with a correction for TOA reflectance, where this approach was affected by the shape of the BRDF and not by its magnitude (Vermote et al., 1997a). Mei and Xue (2013) used an equivalent snow and ice mixture pixel for the spectral surface reflectance: it is constructed using a linear mixing model of snow and ice spectra tuned by the Normalized Difference Snow Index (NDSI) as an indicator of snow cover. Before calculating NDSI, cloud and free water were masked and a Look-Up-Table method was used to retrieve AOT.

Current operational AOT retrieval algorithms, such as MODIS DT (Levy et al., 2013), MISR algorithm (Diner et al., 2005b; Kahn et al., 2010) and AATSR (Holzer-Popp et al., 2013), can determine AOT over the Arctic Ocean (Glantz et al., 2014). Evaluation of the MODIS/Aqua AOT product over Svalbard using a 9-year set of AERONET observations gives an accuracy of  $\pm 0.03 \pm 0.05$  AOT (Glantz et al., 2014). The AOT maps defined by Holzer-Popp et al. (2013) in September 2008 qualitatively show an overestimation over the Arctic Ocean compared with the 9-year mean values from the MODIS Aqua product, AERONET and Alfred Wegener Institute (AWI) observations, which have been separately estimated, giving values of AOT equal to  $\pm 0.031 \pm 0.021$ ,  $\pm 0.031 \pm 0.022$ , and  $\pm 0.024 \pm 0.052$ , respectively (Glantz et al., 2014). However, due to the high reflectance of surface encountered for large solar zenith angles in the Arctic (Mei et al., 2013a; Macdonald et al., 2014), it is very difficult to quantitatively retrieve AOT over snow and ice. Stamnes et al. (2004) pointed out that the TOA reflectance is sensitive to AOT over both very bright and dark surfaces, demonstrating the possibility of retrieving AOT over Arctic regions. Recent publications (Istomina et al., 2011; Mei et al., 2013a,b) show promising AOT results over snow/ice-covered regions, as described below.

Preliminary attempts based on the above concepts were tried by Istomina et al. (2010) to individualise cloud-free snow-covered areas using AATSR measurements, and to discriminate clear snow fields for the retrieval of AOT. In addition to the aerosol retrieval method at the above-mentioned visible and near-infrared wavelengths (Istomina et al., 2009), the AATSR measurements in the  $3.7 \mu\text{m}$  channel were also utilised to retrieve AOT (Istomina et al., 2011). Radiative transfer

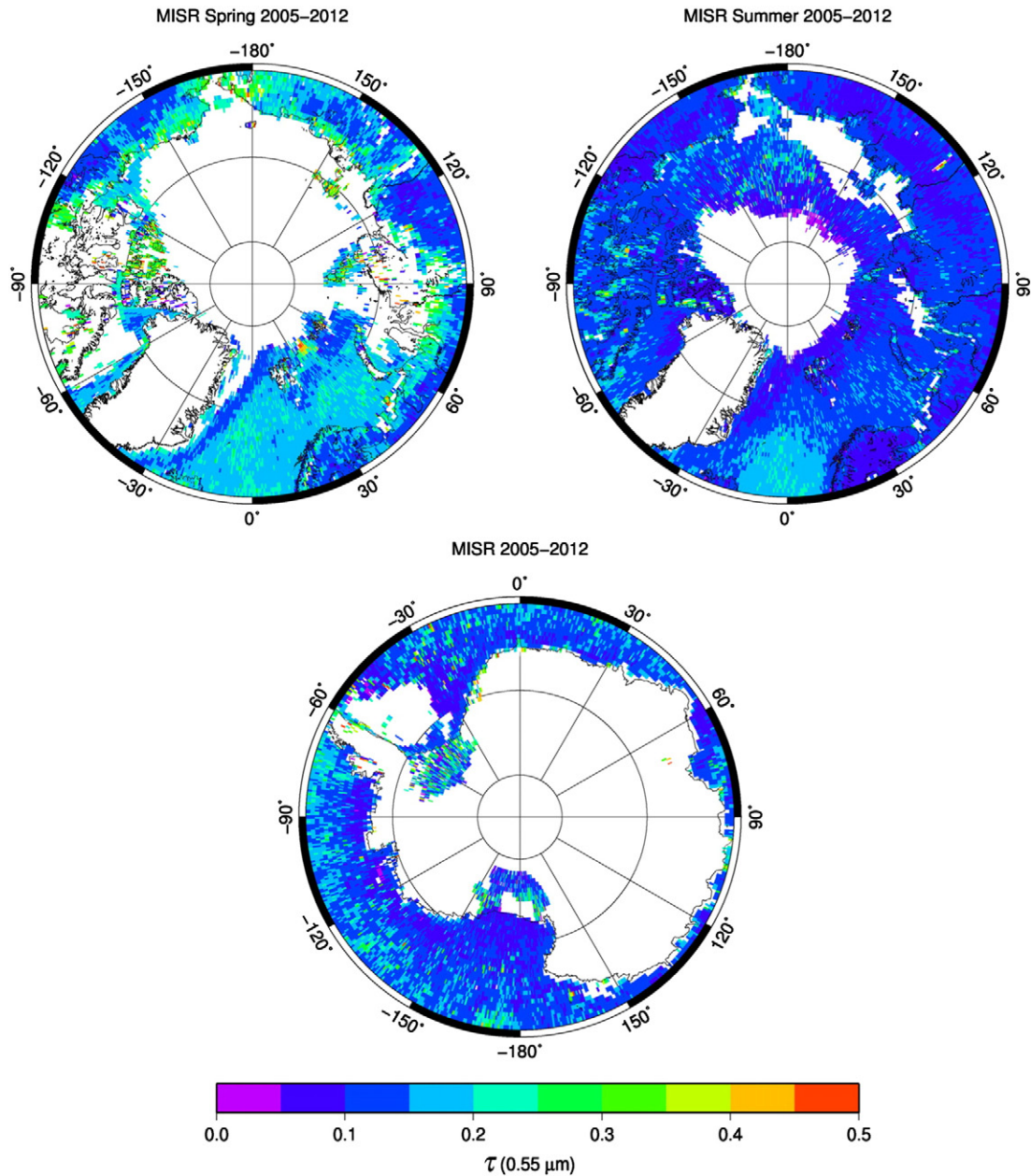


**Fig. 23.** Upper part: Arctic maps of the seasonal average Level-3 aerosol optical thickness  $\tau(0.55 \mu\text{m})$  derived from the MISR satellite data recorded from 2005 to 2012 during the spring (left-hand side) and summer (right-hand side) 3-month periods. Lower part: As in the upper part, for the austral summer average Level-3 aerosol optical thickness  $\tau(0.55 \mu\text{m})$  derived from MISR satellite data recorded from 2005 to 2012 over oceans and land areas not covered by snow and ice.

simulations for the accumulation and coarse particle modes of four main aerosol components were conducted in order to represent the retrieved  $\tau(\lambda)$  in the visible region of the spectrum. The advantage of this algorithm is that it can be used over any blackbody-like surface (open ocean, sea ice, snow-covered land). An example of its usage is shown in Fig. 24.

Improved results were obtained by Mei et al. (2013b) using the Dual-View Multi-Spectral (DVMS) approach, in which the dual view is used to separately evaluate the contributions made by atmospheric aerosols and underlying surfaces to the reflectance measured by this satellite sensor at the TOA-level. The algorithm uses an analytical snow BRDF model to estimate the ratio of snow reflectances in the nadir and forward views, and the atmospheric contribution to the TOA-level reflectance, obtained using the dark pixel method over the adjacent ocean surface, by assuming that this value applies over nearby land surfaces in the absence of significant sources across the

coastline. An iteration involving all four AATSR spectral channels in the visible and near-infrared is used to retrieve the most relevant  $\tau(0.55 \mu\text{m})$  information. The method was illustrated for AATSR overpasses over Greenland in April 2009, during cloud-free sky periods.

Some examples of the results achieved by Mei et al. (2013b) in Fig. 25 show the daily maps of  $\tau(0.55 \mu\text{m})$  retrieved from AATSR data recorded on four days in April 2009 with  $1 \text{ km} \times 1 \text{ km}$  resolution over the western part of Greenland, under cloud-free sky conditions. It can be seen that  $\tau(0.55 \mu\text{m})$  had very low values smaller than 0.10, with little spatial variation for moderate contributions of sea spray aerosol associated with the very low wind speeds at the surface, as observed on the chosen days.

A comparison test between the values of  $\tau(0.55 \mu\text{m})$  retrieved using the DVMS approach for high-quality AATSR observations and the corresponding AERONET values measured at Thule (North-western Greenland) during April 2009 exhibited a good correlation, with a



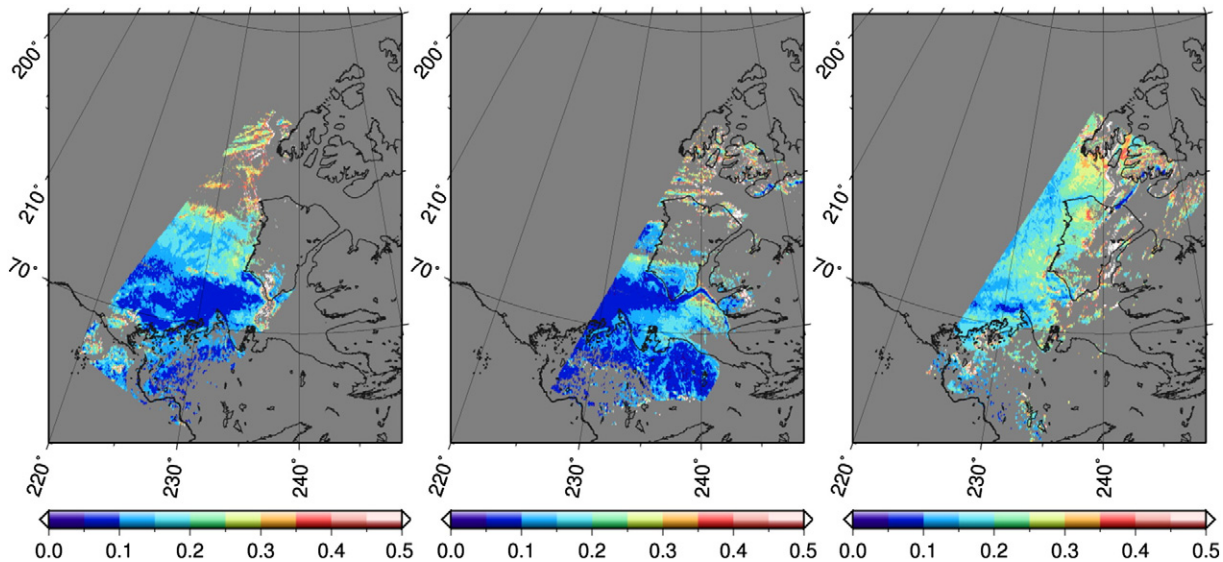


**Fig. 24.** Time sequence of aerosol optical thickness  $\tau(0.55 \mu\text{m})$  retrieved using AATSR data over sea ice and snow-covered land surfaces with the algorithm described by Istomina et al. (2011). Left panel refers to orbit No. 31673 on 21 March, 2008; middle panel to orbit No. 31687 on 22 March, 2008; and right panel to orbit No. 31773 on 28 March, 2008. The increase in  $\tau(0.55 \mu\text{m})$  might be connected to ozone depletion/bromine explosions observed during March 2008 in the region (Nghiem et al., 2012; Moore et al., 2014).

regression coefficient equal to +0.76 (Mei et al., 2013b). However, it should be mentioned that such good results were obtained for a selected set of measurements, containing a high number of cases with  $\tau(0.55 \mu\text{m}) > 0.12$ , due to the frequent occurrence of Arctic haze episodes in April. A synergetic approach to retrieve aerosol optical characteristics over the Arctic, using data from the MODIS sensor mounted onboard the Terra and Aqua platforms and prior knowledge of aerosol optical parameters retrieved over snow (as assumed in the APRS procedure), was presented by Mei et al. (2013a). Bearing in mind that cloud contamination can cause abnormally high retrieved values of AOT, the analysis of MODIS data was limited to only clear-sky pixels selected through MODIS cloud products and visual inspection. In applying the APRS procedure, it was realistically assumed that the aerosol optical parameters do not change during the time between the overpasses of Terra and Aqua platforms. A comparison was also made between the values of  $\tau(0.55 \mu\text{m})$  retrieved over Greenland from MODIS observations following the APRS procedure and those derived from AATSR data with the DVMS method. This comparison showed that the APRS values of  $\tau(0.55 \mu\text{m})$  ranged from 0.07 to 0.09 over the monitored areas, while the DVMS ones were mainly ~0.09, and exhibited a maximum value just 0.6% lower than that derived from MODIS data.

It has to be mentioned that the global application of the above-cited AOT retrieval algorithms for both MODIS and AATSR is still very much limited due to several challenges which are listed below. For instance, one of the major issues is the cloud masking over snow and ice. Cloud screening for AOT retrieval in the Arctic is a challenge due to the similarity of snow/ice and cloud reflective properties in the visible region of the spectrum. The sensitivity of AOT retrievals over snow to atmospheric particulate matter implies a potentially high contamination of the aerosol product with eventually unscreened clouds. It is for these two reasons that many cloud masking algorithms developed for a general case of multiple surface types, such as open water, vegetation and various soils, are of questionable quality over snow and ice. An example of this is the operational AATSR cloud mask provided with the level 1b AATSR product (Istomina et al., 2010). The main approach to distinguishing clouds from the underlying surface is that clouds are generally brighter and colder than the underlying surface. However, this is not always the case over snow/ice-covered regions such as the Arctic. A prominent spectral signature of snow and ice makes it possible to discriminate clouds using NIR and TIR channels. At the same time, not all sensors have such channels. Therefore, cloud-screening algorithms

over snow differ from sensor to sensor in order to most effectively utilise the available features (which are not only the spectral and spatial resolution, but also different observation directions and polarisation measurements). The resulting cloud mask over snow and ice obtained from different sensors also differs in quality. Employing absolute or relative thresholds (e.g. NDSI or NDVI) in the available VIS, NIR and IR channels to separate clouds from snow and ice is a commonly used approach which gives a robust cloud mask over snow for common applications (MERIS, AATSR, SCIAMACHY) (Allen et al., 1990; Istomina et al., 2010; Schlundt et al., 2011). However, as the thresholds are often empirically derived and based on a limited data-set, this approach might have drawbacks when it comes to particular surface or cloud types, e.g. ice clouds over snow. Possible mis-classification here could be: (1) mistaking heavy aerosol loads for clouds, as e.g. might be the case of MODIS test BT11–BT3.9 (Ackerman et al., 2010), or (2) mistaking snow surfaces for clouds as in MODIS test BT11–BT12, which is used to detect cirrus over many surface types also covered by snow and ice (Ackerman et al., 2010). Mis-classification may occur due to snow emissivity being sensitive to grain size at these wavelengths, and creating a difference between the brightness temperatures BTs recorded in the 11 and 12  $\mu\text{m}$  channels (Hori et al., 2006).

A snow BRDF model can also be used to derive the threshold value for the NIR spectral channel, as shown by Spangenberg et al. (2001) and Trepte et al. (2001). This approach might have difficulties in distinguishing cloudy conditions from cloud-free but aerosol-polluted scenarios. The best results can be obtained by combining the various approaches such as thresholding, image clustering, supervised and unsupervised classification, usage of oxygen and water vapour absorption bands if available (e.g. MERIS) (Gomez-Chova et al., 2007) together with usage of external topography data, land/water masks, ecosystem maps and daily operational snow/ice products (MODIS, MISR) (Ackerman et al., 1998; Shi et al., 2002, 2007; Liu et al., 2004). The MODIS cloud mask product with confidence cloudy flag generally works well for thick warm clouds over the Arctic by using 19 channels and auxiliary inputs such as the topography, but will have difficulties with optically thin cold clouds such as cirrus due to the similarity of both cloud types. A comprehensive combined cloud mask is also available for AVHRR (Saunders and Kriebel, 1988; Gesell, 1989; Key and Barry, 1989; Han et al., 1999; Mei et al., 2014). However, the challenge of applying a cloud mask over snow is still current even for radiometers equipped with IR and NIR bands.

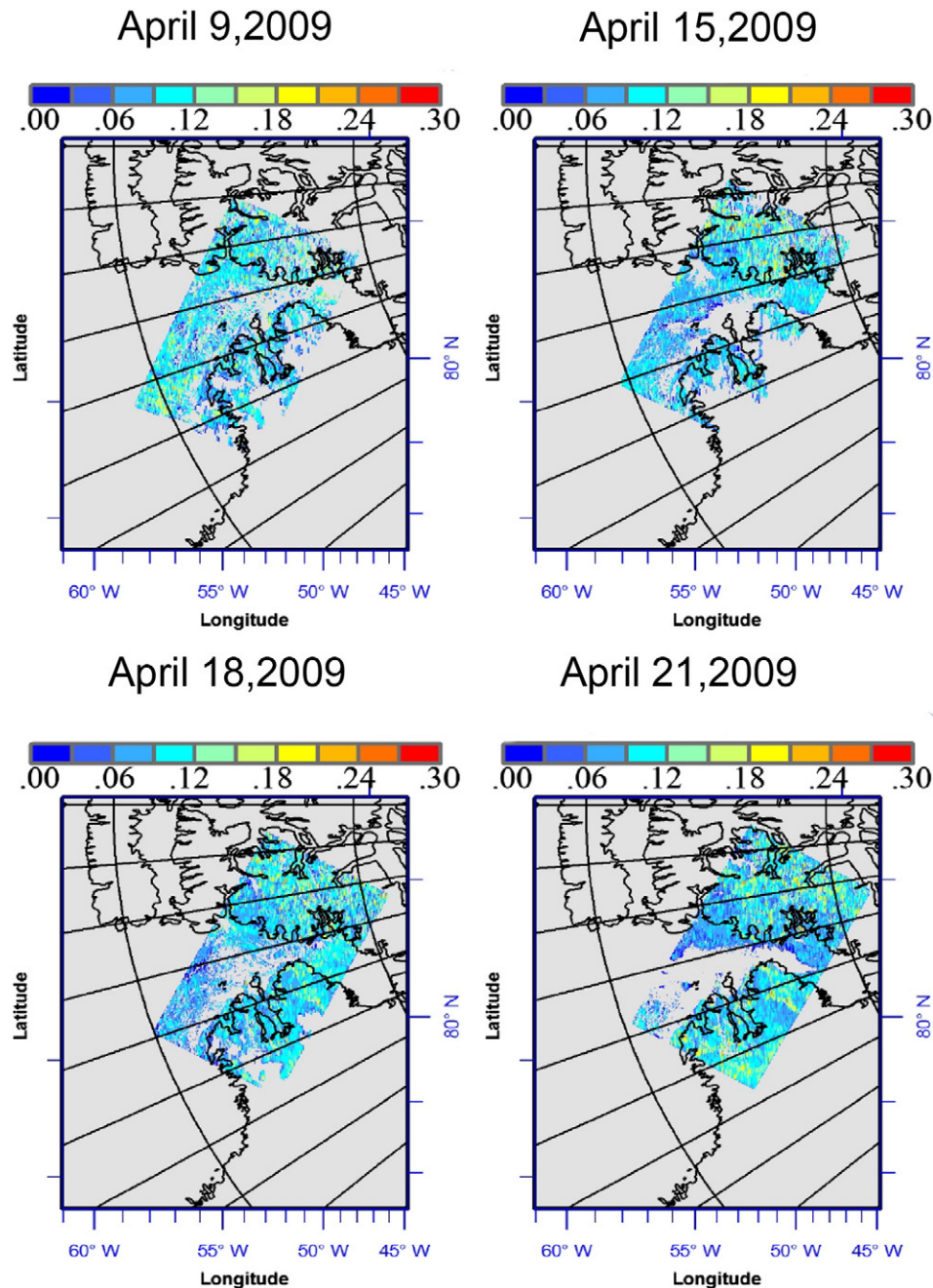


**Fig. 25.** Maps of aerosol optical thickness  $\tau(0.55 \mu\text{m})$  retrieved from AATSR data taken with  $1 \text{ km} \times 1 \text{ km}$  resolution on 9, 15, 18, and 21 April, 2009, over snow-covered surfaces in west Greenland using the method of Mei et al. (2013b).

Another challenge of any AOT retrieval over snow is the variability of snow and sea ice types in the field, the effect of surface melt or ageing, pollution, and regarding sea ice the effect of varying sea ice concentrations. All these effects make it difficult to reliably account for the surface signal contribution to AOT for retrievals over snow surfaces even when double-viewing observational techniques (e.g. AATSR or simultaneous MODIS Terra and Aqua usage) are used. At the same time, as the AOT in the Arctic is rather low (background values  $\sim 0.05$ , up to  $0.1$ – $0.3$  during haze events with occasionally higher peaks), the surface signal is responsible for the greatest part of the TOA signal measured by satellites. Multi-spectral AOT retrievals are in addition challenged by a high variability in ice and snow surface types, depending on grain size, pollution, density, etc. (Warren and Wiscombe, 1980; Negi et al., 2010). The variability of the aerosol types, which includes a varying scattering

phase function shape, spectral behaviour and particle size-distribution, makes it even more challenging to reliably retrieve the AOT, especially when spectral information on both the surface and atmosphere is used simultaneously. The sensitivity to complex polar atmospheric conditions and temperature inversions (especially for IR channels used for the retrieval or the cloud mask) are currently not taken into account and also need to be investigated. The satellite-retrieval algorithms proposed by Istomina et al. (2011); Mei et al. (2013a) and Mei et al. (2013b) can only be used for an initial qualitative evaluation of the atmospheric aerosol load and only for selected apparently cloud-free scenes. They are able to give a correct impression of spatial and temporal AOT distributions on a regional scale under the assumption that the surface and aerosol properties do not change, but need to be further improved with more flexibility regarding surface types, their extensive

validation and specifically developed cloud masking being the first priorities. Due to the above listed issues and challenges, application on a global basis is currently not possible.

## 6. Optical characteristics of Arctic and Antarctic aerosols

To obtain a realistic representation of the optical properties of atmospheric aerosol derived from ground-based and ship-borne sun-photometer measurements, a set of aerosol extinction models has been defined here by taking into account the evaluations of aerosol radiative parameters determined from sun-photometric and in-situ optical measurements made at various Arctic and Antarctic sites. The main results obtained for the nuclei, accumulation and coarse particles are presented in the following two sub-sections for four Arctic and four Antarctic aerosol types.

### 6.1. Arctic aerosol particle size-distributions and optical characteristics

Multi-year measurements of aerosol chemical composition and light scattering and absorption coefficients were conducted at Barrow by Quinn et al. (2002), separately for the sub-micron and super-micron particle modes, showing that: (i) extinction effects are dominated by sulphate fine particles during the spring-time Arctic haze episodes, and by sea-salt accumulation mode particles formed from wind-driven sea spray in winter, and (ii) sub-micron sulphate and sea-salt particles efficiently contribute during summer to attenuate the incoming solar radiation. Both sulphate and sea-salt particle concentrations followed well-defined annual cycles at Barrow, Alert and Arctic EMEP sites (Quinn et al., 2007). Bimodal features of the aerosol size-distribution were reported at Barrow by Delene and Ogren (2002), who found that the overall visible light scattering and absorption at the ground-level is given over the entire year by two particle modes: (i) an accumulation mode (with mode diameter  $D_c < 1 \mu\text{m}$ ) yielding annual mean values of volume scattering coefficient  $\beta_{\text{sca}} = 6.17 \pm 3.61 \text{ Mm}^{-1}$ , volume absorption coefficient  $\beta_{\text{abs}} = 0.36 \pm 0.38 \text{ Mm}^{-1}$ , ground-level Ångström exponent  $\alpha_o = 1.67 \pm 0.36$ , and ground-level single scattering albedo  $\omega_o = 0.954 \pm 0.028$ ; and (ii) a coarse mode (with  $D_c < 10 \mu\text{m}$ ), giving annual mean values of  $\beta_{\text{sca}} = 9.76 \pm 5.20 \text{ Mm}^{-1}$ ,  $\beta_{\text{abs}} = 0.39 \pm 0.41 \text{ Mm}^{-1}$ ,  $\alpha_o = 1.11 \pm 0.39$ , and  $\omega_o = 0.965 \pm 0.023$ .

Multimodal features of the fine particle size-distribution were also reported by Ström et al. (2003) on examining particulate matter sampled at the Zeppelin station (near Ny-Ålesund) with a Differential Mobility Particle Sizer (DMPS) over the  $D < 1 \mu\text{m}$  diameter range. For such multimodal characteristics of the sub-micron aerosols and considering that  $\alpha$  varies throughout the year from more than 1.8 (for prevailing extinction by fine particles) to less than 1 (for predominant attenuation by coarse particles), a set of particulate extinction models is proposed here, each given by a linear combination of a nuclei mode with an accumulation or coarse particle mode, to represent the optical properties of airborne aerosols. In this approach, the overall size-distribution can be defined for a certain value of  $\alpha$  by varying the percentage number density concentrations of both modes until the measured value of  $\alpha$  is fitted.

Each aerosol unimodal size-distribution curve was represented by a log-normal curve having the analytical form,

$$N(r) = \frac{dN(r)}{d(\text{Log } r)} = \frac{N_o}{\sqrt{2\pi} (\text{Log } \sigma)} \exp \left[ -\frac{1}{2} \left( \frac{\text{Log } r - \text{Log } r_c}{\text{Log } \sigma} \right)^2 \right], \quad (3)$$

where  $N_o$  is the total particle number concentration (measured in  $\text{cm}^{-3}$ ),  $\text{Ln } 10$  is a constant approximately equal to 2.3026,  $\text{Log}$  is the decadal logarithm (with base = 10),  $\sigma$  is the geometric standard deviation, and  $r_c$  is the mode radius (measured in  $\mu\text{m}$ ). Thus, the following

size-distribution curves were defined to represent four different Arctic aerosol types:

- (1) The size-distribution curve of winter–spring Arctic haze particles, consisting of: (i) a nuclei mode of dry-air Arctic water-soluble aerosol, and (ii) an accumulation particle mode of sea-salt particles, according to the Hess et al. (1998) OPAC models.
- (2) The average size-distribution of summer background aerosols, consisting of: (i) a fine particle mode predominantly composed of mineral dust nuclei and water-soluble substances, and (ii) a coarse particle mode of sea-salt particles, as defined by Hess et al. (1998).
- (3) The average size-distribution curve of Asian dust, consisting of: (i) a mineral dust nuclei mode, and (ii) a mineral coarse particle mode, having features similar to those represented by Hess et al. (1998) in the mineral dust OPAC models, and chosen to simulate an episode of Asian dust transport over a ground-layer of unpolluted aerosol observed by Stone et al. (2007) at Barrow.
- (4) The overall size-distribution curve of a summer background aerosol model containing BFF smoke, assumed to consist of: (i) a combustion nuclei mode, and (ii) an accumulation particle mode. Both modes were assumed to consist of a mixture of combustion dust and soot particles giving a ratio of 12.86 between the scattering and absorption coefficients, leading to a single scattering albedo value  $\omega = 0.928$ , as indicated by the in-situ measurements conducted by Mielonen et al. (2013) for Russian wildfire particles.

Each of the above eight modes was represented in terms of Eq. (3) for the values of shape-parameters  $r_c$  and  $\sigma$  given in Table 5, while the unimodal optical/chemical characteristics were represented assuming the mass percentages of the 6S dry-air components defined by Vermote et al. (1997a) and provided in Table 5 for each pair of modes, according to the chemical composition estimates made by Quinn et al. (2007) and Tomasi et al. (2012).

The spectral values of the real  $n(\lambda)$  and imaginary  $k(\lambda)$  parts of the particle refractive index obtained for the Arctic aerosol models given in Table 5 were found to decrease very slowly with wavelength over the 0.40–1.0  $\mu\text{m}$  spectral range. They are reported in Table 5 for  $\lambda = 0.55 \mu\text{m}$ , together with values of the single scattering albedo  $\omega(0.55 \mu\text{m})$ , asymmetry factor  $g(0.55 \mu\text{m})$ , volume extinction coefficient  $\beta_{\text{ext}}(0.55 \mu\text{m})$ , and exponent  $\alpha$ . It can be seen in Table 5 that the single scattering albedo  $\omega(0.55 \mu\text{m})$  of the Arctic haze nuclei mode is equal to 0.86 and that of the accumulation mode is equal to 0.937. Therefore, using the present bimodal model,  $\omega(0.55 \mu\text{m})$  is made to vary over the 0.86–0.94 range as a function of the mass fractions of nuclei and accumulation particles. The assumptions made for this optical parameter agree very well with ground-level measurements of  $\omega_o(0.55 \mu\text{m})$  obtained from in-situ nephelometer and aethalometer<sup>2</sup> measurements carried out by: (i) Bodhaine (1995), who estimated a monthly mean value of 0.928 in March at Barrow, (ii) Sharma et al. (2006), who determined an average value of 0.94 from February to May at Barrow, and (iii) Ström et al. (2003), who estimated a monthly mean value  $\omega_o(0.55 \mu\text{m}) = 0.94$  in spring at Zeppelin, and monthly mean values varying from 0.84 to 0.91 in late autumn and winter.

The calculations presented in Table 5 provide a single scattering albedo value  $\omega(0.55 \mu\text{m}) = 0.93$  for the Arctic summer background fine particle mode, and 0.81 for the corresponding coarse particle mode, suggesting that  $\omega(0.55 \mu\text{m})$  varies mainly over the 0.81–0.93 range during the Arctic summer. The results do not differ considerably from those of: (i) Ström et al. (2003), who found that  $\omega_o(0.55 \mu\text{m})$  assumes values varying mainly from 0.94 to 0.98 in spring and summer

<sup>2</sup> for detailed technical characteristics of the two instruments, see Bodhaine (1995) and Anderson and Ogren (1998).



**Table 5**

Values of shape-parameters  $\sigma$  and  $r_c$  of the log-normal curves adopted to represent the nuclei, accumulation and coarse particle modes determined at Arctic and Antarctic sites, all normalised to give the value of overall particle number concentration  $N_o = 1000 \text{ cm}^{-3}$ . They are given together with the spectral values of real part  $n$  and imaginary part  $k$  of the complex refractive index at the  $0.55 \text{ }\mu\text{m}$  wavelength, single scattering albedo  $\omega(0.55 \text{ }\mu\text{m})$ , asymmetry factor  $g(0.55 \text{ }\mu\text{m})$ , volume extinction coefficient  $\beta_{\text{ext}}(0.55 \text{ }\mu\text{m})$  and Ångström's exponent  $\alpha$  calculated over the  $0.40\text{--}0.87 \text{ }\mu\text{m}$  wavelength range for the spectral evaluations of  $\beta_{\text{ext}}(\lambda)$  made using the 6S radiative transfer code of Vermote et al. (1997a). The 6S aerosol components are labelled according to Vermote et al. (1997 b): oceanic (OC), water-soluble (WS), dust-like (DL) and soot (SO).

Aerosol type	Log-normal mode	Mass percentages of the basic 6S dry-air components				Geometric standard deviation $\sigma$	Mode radius $r_c$ ( $\mu\text{m}$ )	Particulate matter refractive index parts		$\omega$ (0.55 $\mu\text{m}$ )	$g$ (0.55 $\mu\text{m}$ )	$\beta_{\text{ext}}$ (0.55 $\mu\text{m}$ ) ( $\text{km}^{-1}$ )	Exponent $\alpha$
		OC	WS	DL	SO			$n$ (0.55 $\mu\text{m}$ )	$k$ (0.55 $\mu\text{m}$ )				
Winter-spring (Arctic haze) aerosol	Nuclei	35	39	22	4	2.24	$2.1 \cdot 10^{-2}$	1.487	$2.17 \cdot 10^{-2}$	0.864	0.637	$1.221 \cdot 10^{-8}$	1.581
	Accum.	58	4	38	—	2.03	$3.0 \cdot 10^{-1}$	1.444	$3.28 \cdot 10^{-3}$	0.937	0.745	$4.088 \cdot 10^{-3}$	−0.117
Arctic summer background aerosol	Fine	18	35	45.8	1.2	1.95	$3.5 \cdot 10^{-2}$	1.506	$1.10 \cdot 10^{-2}$	0.930	0.605	$4.353 \cdot 10^{-8}$	1.871
	Coarse	71	1	28	—	2.03	1.75	1.424	$2.30 \cdot 10^{-3}$	0.813	0.846	3.200	−0.054
Asian dust	Fine	—	24	76	—	1.95	$7.0 \cdot 10^{-2}$	1.530	$7.52 \cdot 10^{-3}$	0.956	0.666	$5.094 \cdot 10^{-6}$	1.039
	Coarse	4	6	90	—	2.15	1.30	1.552	$7.56 \cdot 10^{-3}$	0.673	0.860	1.385	−0.058
Boreal forest fire smoke	Nuclei	—	—	97.9	2.1	2.00	$3.9 \cdot 10^{-2}$	1.535	$7.71 \cdot 10^{-2}$	0.906	0.627	$1.698 \cdot 10^{-7}$	1.556
	Accum.	—	—	98.4	1.6	2.00	$1.2 \cdot 10^{-1}$	1.534	$1.49 \cdot 10^{-2}$	0.892	0.700	$9.878 \cdot 10^{-5}$	0.345
Antarctic austral summer coastal aerosol	Fine	52	40	7.5	0.5	2.03	$7.0 \cdot 10^{-2}$	1.454	$6.30 \cdot 10^{-3}$	0.958	0.712	$5.811 \cdot 10^{-6}$	0.997
	Coarse	61	16.5	22.5	—	2.10	1.50	1.439	$2.79 \cdot 10^{-3}$	0.795	0.844	2.117	−0.058
Austral summer	Fine	11.2	86.4	2.2	0.2	2.24	$2.1 \cdot 10^{-2}$	1.514	$6.24 \cdot 10^{-3}$	0.959	0.620	$1.320 \cdot 10^{-8}$	1.603
Antarctic Plateau aerosol	Coarse	86	6	8	—	2.03	1.75	1.402	$1.00 \cdot 10^{-3}$	0.900	0.831	3.204	−0.056
Antarctic austral winter aerosol (*)	Nuclei	—	90	10	—	2.03	$7.0 \cdot 10^{-2}$	1.530	$6.20 \cdot 10^{-3}$	0.960	0.671	$7.477 \cdot 10^{-6}$	0.857
	Accum.	95	—	5	—	2.03	$5.0 \cdot 10^{-1}$	1.388	$4.00 \cdot 10^{-4}$	0.986	0.774	$2.724 \cdot 10^{-2}$	−0.157

(\*) for its use at both Antarctic coastal and high-altitude sites.

at Zeppelin, and (ii) Tomasi et al. (2012), who obtained monthly mean values of  $\omega_o(0.55 \text{ }\mu\text{m})$  equal to  $0.93 \pm 0.04$  in June,  $0.86 \pm 0.09$  in July,  $0.91 \pm 0.08$  in August, and  $0.89 \pm 0.09$  in September, yielding a seasonal average value of  $0.90 \pm 0.07$  at Ny-Ålesund during summer 2010. The values of  $\omega(0.55 \text{ }\mu\text{m})$  assumed in Table 5 for the Asian dust are close to 0.96 for the fine particle mode and 0.67 for the coarse particle mode, indicating that this parameter is presumably subject to decrease gradually as  $\alpha$  assumes lower values as a result of the increase in the relative super-micron dust content. The nuclei and accumulation particle components of the BFF smoke were both found to yield values of  $\omega(0.55 \text{ }\mu\text{m})$  close to 0.90, according to Mielonen et al. (2013).

The angular distribution curves of phase function  $P(\theta)$  determined for the eight unimodal size-distribution curves defined in Table 5 to represent the four Arctic aerosol types are shown on the left-hand side of Fig. 26. The calculations clearly show that the most pronounced

forward scattering lobe is produced by the Asian dust coarse mode and, to a lesser extent, by the coarse mode of Arctic summer background aerosol, which yields the lowest lateral scattering (at  $\theta = 90^\circ$ ) and the strongest backward scattering (at  $\theta = 180^\circ$ ).

The linear combinations of nuclei and accumulation or coarse particle modes considered in Table 5 for the four Arctic aerosol types were made to vary until best-fit values of  $\alpha$  were obtained from field sun-photometer measurements, which provide the unimodal column particle number concentrations for each field-measured value of  $\tau(0.50 \text{ }\mu\text{m})$ . The following four cases were examined: (a) the winter-spring aerosol case recorded at Eureka during the Arctic haze periods of 2007 and 2008, with average values of  $\tau(0.50 \text{ }\mu\text{m}) = 0.12$  and  $\alpha = 1.48$ , (b) the summer background aerosol case determined at Tiksi, giving mean values of  $\tau(0.50 \text{ }\mu\text{m}) = 0.08$  and  $\alpha = 1.60$ , (c) the Asian dust transport episode observed at Barrow on 16 April, 2002, yielding average daily

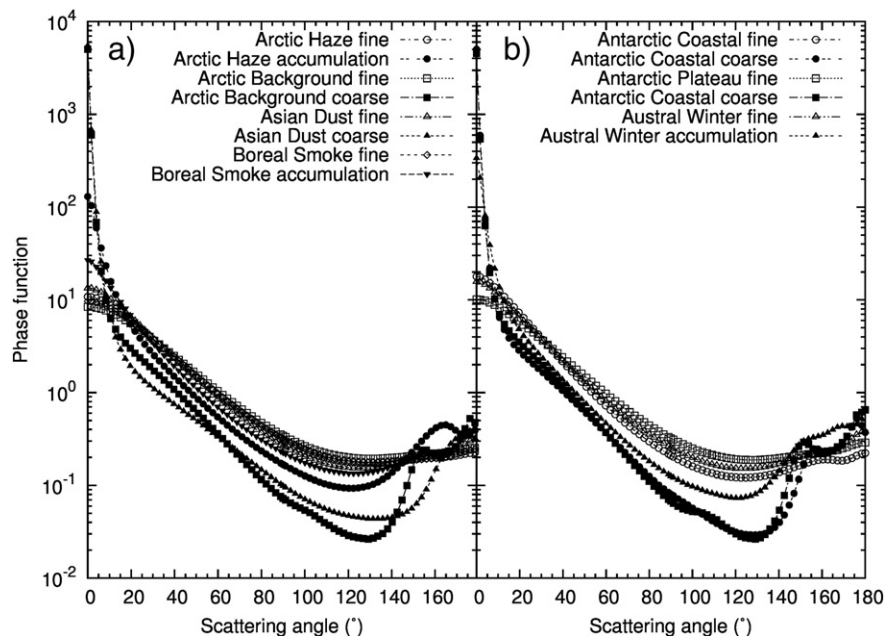


**Fig. 26.** Angular distribution curves of phase function  $P(\theta)$  as a function of the scattering angle  $\theta$  for the 8 unimodal Arctic aerosol extinction models (left) and the 6 unimodal Antarctic aerosol extinction models defined in Table 5.

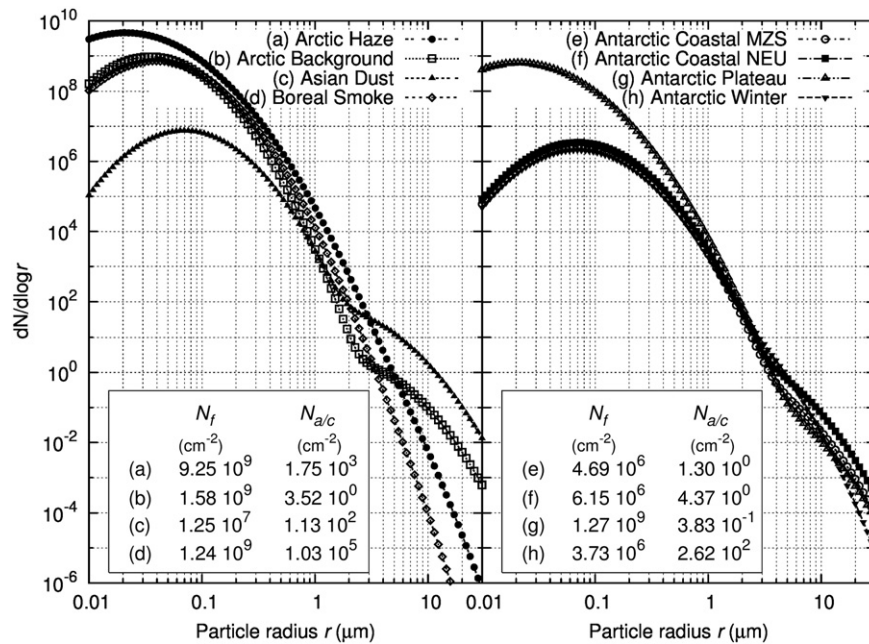


**Fig. 27.** Left-hand side: examples of bimodal particle size-distribution curves obtained as best-fit linear combinations of aerosol unimodal models for nuclei and accumulation or coarse particles defined in Table 3 in the following four case studies: (a) the average winter–spring aerosol case determined at Eureka (Nunavut, Northern Canada) for the mean values  $\tau(0.50 \mu\text{m}) = 0.12$  and  $\alpha = 1.48$ ; (b) the summer background aerosol case determined at Tiksi (Russia) in North-central Siberia for the mean values  $\tau(0.50 \mu\text{m}) = 0.08$  and  $\alpha = 1.60$ ; (c) the Asian dust episode observed at Barrow on 16 April, 2002, giving the mean daily values  $\tau(0.50 \mu\text{m}) = 0.22$  and  $\alpha = 0.26$ ; and (d) the BFF smoke episode observed by Stock et al. (2012) at Ny-Ålesund on 23 March, 2008, for the daily mean values  $\tau(0.50 \mu\text{m}) = 0.22$  and  $\alpha = 1.50$ . Right-hand side: as on the left, for the following four case studies: (e) the austral summer coastal aerosol case determined at Mario Zucchelli (MZS) for the mean values  $\tau(0.50 \mu\text{m}) = 0.03$  and  $\alpha = 0.90$ ; (f) the austral summer coastal aerosol case determined at Neumayer (NEU) for the mean values of  $\tau(0.50 \mu\text{m}) = 0.045$  and  $\alpha = 0.78$ ; (g) the austral summer Antarctic Plateau aerosol case determined at South Pole for the mean values  $\tau(0.50 \mu\text{m}) = 0.018$  and  $\alpha = 1.49$ ; and (h) the austral winter aerosol case assumed at Neumayer for the seasonal average values  $\tau(0.50 \mu\text{m}) = 0.035$  and  $\alpha = 0.65$ .

values of  $\tau(0.50 \mu\text{m}) = 0.22$  and  $\alpha = 0.26$ , and (d) the BFF smoke case observed by Stock et al. (2012) at Ny-Ålesund on 23 March, 2008, giving average daily values of  $\tau(0.50 \mu\text{m}) = 0.22$  and  $\alpha = 1.50$ . The best-fit bimodal size-distribution curves determined for the four cases are presented on the left-hand side of Fig. 27, together with the corresponding column particle number concentration of the nuclei/fine mode ( $N_f$ ) and accumulation or coarse mode ( $N_{a/c}$ ). The bimodal size-distribution curves obtained for the winter–spring case (a) and the BFF smoke case (d) exhibit in practice a nearly unimodal shape, since  $N_{a/c}$  is lower than  $N_f$  by about 7 orders of magnitude in case (a) and by more than 4 orders of magnitude in case (d). Conversely, the bimodal size-distribution curves obtained in cases (b) and (c), each using one of the coarse particle modes defined in Table 5, exhibit rapidly decreasing right-hand wings of the columnar number content over the whole super-micron radius range, associated with sea-salt and dust particle loads.

## 6.2. Antarctic aerosol particle size-distributions and optical properties

Multimodal characteristics of the aerosol size-distribution curves were also reported at Antarctic coastal and high-altitude sites. Analysing a set of size-segregated particle samples collected at Mario Zucchelli (Terra Nova Bay) in austral summer 1995, over the  $0.035\text{--}16 \mu\text{m}$  aerodynamic diameter range, Hillamo et al. (1998) found that the particle size-distribution usually consists of four modes: (i) a fine particle mode, with peak diameter  $D_c = 0.07 \mu\text{m}$ , which contributes  $\sim 1\%$  to the total particulate mass content, (ii) an accumulation particle mode with  $D_c \approx 0.30 \mu\text{m}$ , contributing 14%, (iii) a coarse particle mode with  $D_c \sim 2 \mu\text{m}$  (22%), and (iv) a coarse particle mode with  $D_c \approx 6.5 \mu\text{m}$  (63%). Similar results were obtained by Weller and Lampert (2008) at Neumayer, revealing a seasonal cycle characterised by nss sulphate particles in austral summer, which dominated optical effects, and prevailing extinction by sea-salt aerosol in the other seasons. They found an average aerosol mass concentration at ground-level

close to  $1.1 \mu\text{g m}^{-3}$  in austral winter and  $1.3 \mu\text{g m}^{-3}$  in austral summer. The average chemical composition of particulate mass consisted of: (i) 48% sea-salt, 33% nss sulphate, 12% MSA, and  $\sim 7\%$  nitrates mixed with mineral dust and ammonium during the austral summer, and (ii) 93% sea-salt particles, with a few percent of nss sulphate, nitrate, MSA, ammonium and mineral dust in the austral winter. Minikin et al. (1998) found that the nss sulphate and MSA concentrations measured in the austral summer at the coastal stations of Neumayer, Halley and Dumont d'Urville are closely correlated, showing a regular sequence of pronounced peaks of both such biogenic sulphur aerosol components, mainly formed from dimethyl sulphide (DMS).

The aerosol chemical composition was investigated at the Finnish station of Aboa, about 150 km from the Atlantic Ocean coast in Queen Maud Land, by Kerminen et al. (2000); Teinilä et al. (2000) and Koponen et al. (2003), who analysed sets of regular aerosol sampling measurements conducted from December 1997 to February 1998. The sea-salt particle concentration was estimated to be considerably lower than those measured at Mario Zucchelli and Neumayer. Multimodal features of the particle size-distribution curve were detected in most cases over the  $0.045 \leq D \leq 15 \mu\text{m}$  range, with five principal modes: (i) a first mode of nuclei, over the  $0.03\text{--}0.10 \mu\text{m}$  range, consisting of 63% nss sulphate, 29% ammonium, and 8% MSA mass percentages, (ii) two accumulation particle modes, with average values of  $D_c$  close to  $0.30$  and  $0.65 \mu\text{m}$ , both consisting on average of 61% nss sulphate, 22% MSA, and  $\sim 14\%$  ammonium, besides a few percents of sea-salt particles, (iii) a coarse particle mode, with  $D_c$  varying from  $1.4$  to  $1.9 \mu\text{m}$ , and consisting of 52% sea-salt, 27% nss sulphate, 12% MSA, and minor percentages of nitrates and ammonium ions, and (iv) a coarse particle mode, with daily mean values of  $D_c$  varying from  $2$  to  $5 \mu\text{m}$ , and containing on average 63% sea-salt, 16% nitrate, 14% nss sulphate, 5% MSA and 2% ammonium. These compositional characteristics indicate that biogenic sulphur compounds constitute on average more than 90% of the aerosol mass concentration of sub-micron particles,  $\sim 50\%$  of the accumulation mode particle mass, and  $\sim 30\%$  of the coarse mode particle

mass. Correspondingly, sea-salt particles were found to mainly contribute to the super-micron aerosol mode by more than 60% on average. The above results were substantively confirmed by Virkkula et al. (2006), who analysed a large set of particulate samples collected in January 2000 using a 12-stage low-pressure impactor, and observed a pair of sea-salt particle modes centred at  $D_c \approx 0.8 \mu\text{m}$  and  $D_c \approx 3 \mu\text{m}$ , respectively, and a pair of nitrate particle modes centred at diameters  $D_c$  of  $\sim 1.2 \mu\text{m}$  and  $\sim 3 \mu\text{m}$ .

The Antarctic Plateau aerosol size-distribution was found to consist of a fine particle mode mainly composed of nss sulphate and MSA substances at South Pole during the austral summer (Hara et al., 2004), when aerosols are predominantly due to strong subsidence effects from the free troposphere. However, sea-salt accumulation and coarse particles can be often transported over the Antarctic Plateau in air masses with relatively high mass concentrations on days characterised by intense advection of oceanic air masses over the interior of Antarctic continent, associated with large storm systems (Shaw, 1988). Therefore, in the particular cases yielding values of  $\alpha$  appreciably lower than 1.8, the overall particle size-distribution was represented using a bimodal size-distribution model consisting of a fine particle mode mainly containing nss sulphates and a sea-salt coarse particle mode.

On the basis of the above measurements, the following size-distribution curves were considered:

- The average size-distribution of Antarctic austral summer coastal aerosol was assumed to be bimodal, since the extinction effects produced by the two Aitken nuclei modes reported by Hillamo et al. (1998) were neglected. It was represented by the linear combination of: (i) a first particle mode consisting of fine nss sulphate and sea-salt accumulation particles, with low contents of mineral nuclei and soot particles, and (ii) a coarse mode mainly composed of sea-salt particles. The composition of both modes was defined using the 6S (Vermote et al., 1997b) mass percentages reported in Table 5, according to the composition data calculated by Tomasi et al. (2012) at Mario Zucchelli and Neumayer. In both particle modes, the soot mass concentration was assumed taking into account the low values of BC mass concentration measured by Wolff and Cachier (1998) at Halley during the austral summer, ranging in general from 1.0 to 2.0  $\text{ng m}^{-3}$ .
- The average size-distribution of austral summer background aerosol over the Antarctic Plateau was represented by: (i) a fine particle mode mainly containing nss sulphates and minor percentages of sea-salt and dust particles, with a soot content equal to 40% of that estimated by Wolff and Cachier (1998) at a coastal site, and (ii) a coarse particle mode composed mainly of sea-salt particles, and containing lower mass percentages of water-soluble and dust-like 6S (Vermote et al., 1997b) components, as given in Table 5.
- The average size-distribution of Antarctic austral winter aerosol at coastal sites was not based on sun-photometer measurements, as such measurements have neither been conducted during the austral winter at coastal sites (for  $66^\circ$ – $75^\circ$  S latitudes) nor at Antarctic Plateau stations. In order to achieve reliable evaluations of complex refractive index  $n(\lambda)$ – $k(\lambda)$  and the other radiative parameters during the austral winter, the chemical composition data determined by Minikin et al. (1998) at Neumayer and other Antarctic coastal sites over the 14-year period from 1983 to 1996 were taken into account. These in-situ measurements showed a regular sequence of pronounced mass concentration minima of biogenic sulphur aerosol components originating from DMS in austral winter and some marked peaks in summer. In particular, they found that: (i) the nss sulphate mass concentration decreased on average from 50 to 4  $\text{ng m}^{-3}$  (i.e. by 92%) from austral summer to winter, and (ii) MSA mass concentration decreased from 17 to 2  $\text{ng m}^{-3}$  (i.e. by more than 88%), because of a strong reduction in biogenic sources of both chemical species

during the local winter. Conversely, the sea-salt particle mass concentration was estimated by Weller and Lampert (2008) to increase at Neumayer by more than 40%, passing from an average summer value of  $597 \pm 830 \text{ ng m}^{-3}$  to an average winter value of  $844 \pm 1100 \text{ ng m}^{-3}$ . Despite the plausible strong decrease in sea-salt particle concentration caused by the ice coverage of the ocean areas near the Antarctic continent, the observed austral winter increase in the sea-salt concentration was probably due to the more intense transport of maritime particles from the lower latitude oceanic ice-free areas characterised by higher wind speed conditions at the sea-surface.

On the basis of these remarks, it was decided to use a bimodal model to represent the austral winter aerosol at coastal sites, consisting of: (i) a water-soluble nuclei mode, and (ii) an accumulation particle mode composed mainly of sea-salt particles transported from remote ocean areas. Each mode of the three Antarctic bimodal size-distribution curves was assumed to have an analytical form given by Eq. (3) for the values of shape-parameters  $r_c$  and  $\sigma$  reported in Table 5, and to consist of the mass percentages defined in Table 5 for the four 6S (Vermote et al., 1997b) basic components.

Because of the predominant mass fractions of nss sulphate in the nuclei/fine particle mode and of sea-salt in the accumulation or coarse mode, the three bimodal size-distributions of Antarctic particles considered above provided the unimodal average values of refractive index parts  $n(0.55 \mu\text{m})$  and  $k(0.55 \mu\text{m})$  given in Table 5. For these aerosol extinction models, values of  $\omega(0.55 \mu\text{m})$  ranging from  $\sim 0.80$  (for the coarse mode of coastal aerosols) to 0.99 (for the accumulation mode of austral winter aerosol) were obtained (see Table 5). These estimates of  $\omega(0.55 \mu\text{m})$  agree very well with the in-situ evaluations made by: (i) Virkkula et al. (2006a,b) at Aboa, who obtained values of  $\omega_o(0.55 \mu\text{m}) > 0.95$  for about 93% of in-situ measurements, and  $< 0.90$  for only 3.5% of cases, (ii) Weller and Lampert (2008) at Neumayer, who estimated that  $\omega_o(0.55 \mu\text{m})$  varied from 0.97 to 1.00 in more than 95% of samples, and (iii) Tomasi et al. (2012), who found values of  $\omega_o(0.55 \mu\text{m})$  mainly ranging from 0.95 to 0.98 for the particulate chemical composition measurements made by Hillamo et al. (1998) and Fattori et al. (2005) at Mario Zucchelli, and those conducted by Weller and Wagenbach (2007); Weller et al. (2008) and Weller and Lampert (2008) at Neumayer. These findings are in good agreement with the in-situ evaluations made by: (i) Bodhaine (1995), who obtained monthly mean values of  $\omega_o(0.55 \mu\text{m})$  at South Pole, varying from 0.942 to 0.972 during the austral summer, and an annual mean value of  $\omega_o(0.55 \mu\text{m}) = 0.97$ , (ii) Heintzenberg et al. (1997), who determined an annual average value of  $\omega_o = 0.965$  in the visible at South Pole; and (iii) Tuncel et al. (1989) and Arimoto et al. (2004) at South Pole, and Piel et al. (2006) at Kohnen, who obtained values of  $\omega_o(0.55 \mu\text{m})$  ranging from 0.95 to 0.98.

The daily mean values of  $\tau(0.55 \mu\text{m})$  retrieved by Campbell et al. (2012) from the 2007 MODIS and MISR satellite observations recorded over Antarctica were all lower than 0.10 throughout the whole year. Reliable measurements of AOT were not retrieved by Winker et al. (2010) from the CALIOP lidar observations during the Antarctic “polar night”, since they were lower than the lidar detection limit. This was confirmed by Winker et al. (2013), who showed that the CALIPSO mean cloud-free day-time and night-time values of  $\tau(0.532 \mu\text{m})$  were all lower than 0.05 over the Antarctic continent and the peri-Antarctic regions during the long austral winter, from March to November. Therefore, the AOT contribution exhibited by nuclei is in general  $< 0.01$  in the austral winter months, while that of sea-salt accumulation particles increases appreciably yielding daily values of  $\tau(0.50 \mu\text{m})$  varying from 0.02 to 0.05 during the coldest season, and values of  $\alpha$  mainly ranging from 0.50 to 0.70 over the peri-Antarctic regions (Winker et al., 2013).

The angular diagrams of phase function  $P(\theta)$  obtained for the unimodal size-distribution curves defined in Table 5 for the three



Antarctic aerosol types are presented on the right-hand side of Fig. 26 as a function of scattering angle  $\theta$ . The most pronounced forward scattering lobe is given by the coarse particle mode of the austral summer coastal aerosol, while the austral summer coarse particle mode of the Antarctic Plateau size-distribution yields a slightly lower forward scattering lobe and the most marked backward and lateral (at  $\theta = 90^\circ$ ) scattering intensities. As a result, four case studies of Antarctic aerosol were analysed to determine the corresponding best-fit linear combinations of a fine particle mode and an accumulation or coarse particle mode, for the following sets of  $\tau(0.50 \mu\text{m})$  and  $\alpha$ : (i) the austral summer coastal aerosol case (e) obtained at Mario Zucchelli for the mean values of  $\tau(0.50 \mu\text{m}) = 0.030$  and  $\alpha = 0.90$ , (ii) the austral summer coastal aerosol case (f) determined at Neumayer for the mean values of  $\tau(0.50 \mu\text{m}) = 0.043$  and  $\alpha = 0.68$ , (iii) the austral summer Antarctic Plateau aerosol case (g) defined at South Pole for the mean values of  $\tau(0.50 \mu\text{m}) = 0.018$  and  $\alpha = 1.49$ , and (iv) the austral winter aerosol case (h) defined on the basis of in-situ aerosol measurements conducted during the austral winter months at Neumayer and evaluated to give the average seasonal values of  $\tau(0.50 \mu\text{m}) = 0.035 \pm 0.015$  and  $\alpha = 0.65 \pm 0.10$ . The bimodal size-distribution curves obtained by applying the best-fit procedure for the four values of  $\alpha$  given above are shown on the right-hand side of Fig. 27, where the columnar number contents  $N_f$  and  $N_{a/c}$  are also given. The size-distribution curves obtained in cases (e), (f) and (g) by assuming the presence of a coarse mode are characterised by robust right-hand wings over the super-micron radius range. In fact, in the two coastal cases (e) and (f), the columnar number content  $N_{a/c}$  is lower than  $N_f$  by more than 6 and 5 orders of magnitude, respectively. Fig. 27 also shows that the relative contribution of sea-salt coarse mode particles is appreciably higher at Neumayer than at Mario Zucchelli, according to the results shown in Figs. 9 and 11, respectively. Considerably different values of  $N_f$  and  $N_{a/c}$  by at least nine orders of magnitude were found in case (g) for the Antarctic Plateau aerosol, giving a measure of the large differences characterising the atmospheric concentrations of nss sulphate nuclei mode and sea-salt coarse mode. By contrast, the accumulation mode used in case (h) to represent the sea-salt particles during the austral winter seems to contribute more weakly (by only 4 orders of magnitude) to enhance  $N_{a/c}$ , with respect to  $N_f$ .

### 6.3. Evaluations of direct aerosol-induced radiative forcing effects in polar regions

Atmospheric aerosols are known to affect the radiation balance of the surface–atmosphere system (i) directly through interaction with solar (short-wave) radiation (Haywood and Boucher, 2000) and terrestrial (long-wave) radiation (Lubin et al., 2002), and (ii) indirectly, by acting as cloud condensation nuclei and modifying cloud albedo characteristics (Schwartz and Andreae, 1996). They can considerably modify the horizontal and vertical distribution of radiant energy passing through the atmosphere (Stone et al., 2008), generally causing more intense changes in the outgoing flux of solar radiation at TOA-level than those affecting the long-wave radiation, as clearly indicated by Mie (1908) theory. For this reason, the direct aerosol-induced radiative forcing (hereinafter referred to as DARF) is commonly evaluated by only considering variations induced by airborne aerosols on the short-wave radiation flux and by neglecting those affecting long-wave radiation. Instantaneous DARF effects can vary on a diurnal basis as a function of solar zenith angle  $\theta_0$ , and closely depend on: (a) aerosol scattering and absorption characteristics (represented in terms of parameters  $\tau(\lambda)$ ,  $\alpha$ ,  $n(\lambda)$ ,  $k(\lambda)$ ,  $P(\theta)$ ,  $g(\lambda)$ , and  $\omega(\lambda)$  at solar wavelengths), and (b) the spectral and geometrical features of surface reflectance. Three different instantaneous DARF terms are usually considered in these calculations: (i) at the TOA-level, as the difference  $\Delta F_{TOA}(t)$  estimated at a certain time  $t$  between the upward solar radiation fluxes emerging from the real atmosphere with aerosols and from the pristine atmosphere without aerosols (Hänel et al., 1999), (ii) at the bottom-of-

atmosphere (BOA) level (i.e. at the surface), as the difference  $\Delta F_{BOA}(t)$  estimated at a certain time  $t$  between the net short-wave fluxes determined at surface-level in the atmosphere with aerosols and in the same atmosphere assumed without aerosols (Satheesh and Ramanathan, 2000) and (iii) within the atmosphere, as the difference  $\Delta F_{ATM}(t)$  between terms  $\Delta F_{TOA}(t)$  and  $\Delta F_{BOA}(t)$  (Ramanathan et al., 2001). To give an average measure of the daily DARF effects, the instantaneous terms  $\Delta F_{TOA}(t)$ ,  $\Delta F_{BOA}(t)$  and  $\Delta F_{ATM}(t)$  are generally evaluated at pre-fixed hours of the day, and then integrated over the entire period from sunrise to sunset, and divided by the 24-hour period. The corresponding diurnally averaged DARF terms  $\Delta F_{TOA}$ ,  $\Delta F_{BOA}$  and  $\Delta F_{ATM}$  were calculated by following such a procedure, based on the Bush and Valero (2003) criteria. Negative values of  $\Delta F_{TOA}$  indicate that aerosols cause an increase in the radiation budget of the surface–atmosphere system at TOA-level, producing direct cooling effects on the climate system, while positive values of  $\Delta F_{TOA}$  indicate the occurrence of a warming effect during the day. Term  $\Delta F_{BOA}$  at the surface gives a measure of the perturbation induced by airborne aerosols in the net flux reaching the surface, which may be positive (warming) or negative (cooling), while term  $\Delta F_{ATM} = \Delta F_{TOA} - \Delta F_{BOA}$  defines the radiation surplus (or deficit) induced by aerosols within the atmosphere. In practice,  $\Delta F_{ATM}$  is the amount of latent heat released in the atmosphere by aerosols and internally redistributed with the effects of modifying both temperature gradients and atmospheric circulation.

Calculations of  $\Delta F_{TOA}$ ,  $\Delta F_{BOA}$  and  $\Delta F_{ATM}$  have been made by Tomasi et al. (2014) using the radiative transfer 6S code of Vermote et al. (1997a) for the aerosol loads and composition, and optical characteristics defined in Table 6, pertaining to 11 Arctic aerosol types and 4 Antarctic background austral summer aerosol types. The calculation procedure consisted of the following seven steps:

- (i) Determination of the columnar aerosol extinction parameters  $\tau(\lambda)$  and  $\alpha$  from the field sun-photometer measurements collected at Barrow, Ny-Ålesund, Summit, Sodankylä, Tiksi, Mario Zucchelli, Neumayer, Dome Concordia and South Pole, from which the average values of  $\tau(0.50 \mu\text{m})$  and  $\alpha(0.40\text{--}0.87 \mu\text{m})$  given in Table 6 were obtained.
- (ii) Calculation of the spectral values of parameters  $n(\lambda)$  and  $k(\lambda)$  for the chemical composition data based on the OPAC mass percentages of fine and coarse particles defined by Hess et al. (1998) for the six OPAC basic components reported in Table 6 at 50% relative humidity of air.
- (iii) Definition of the multimodal linear combinations of the size-distribution curves for the 15 aerosol types considered in Table 6 to fit the values of  $\alpha(0.40\text{--}0.87 \mu\text{m})$  given in Table 6.
- (iv) Calculation of the aerosol single scattering albedo  $\omega(0.55 \mu\text{m})$  reported in Table 6 for the 15 multimodal size-distribution curves defined at the previous step.
- (v) Selection of the BRDF surface reflectance models of Tomasi et al. (2013) to represent the surface reflectance characteristics of the land surfaces described in terms of MODIS Level 3.0 MCD43C3 products around the principal sun-photometer stations, and those of Arctic and Antarctic oceanic surfaces. The analysis of such observational data suggested that the following models were suitable in the present calculations: (a) the BRDF ocean surface reflectance model OS1, defined for surface wind velocity  $V_w = 2 \text{ m s}^{-1}$  and giving a value of broadband albedo  $A_b(\theta_0 = 60^\circ) = 0.193$ , (b) the BRDF surface reflectance model VS1, yielding a value of  $A_b(\theta_0 = 60^\circ) = 0.155$ , and used to represent a land area covered by tundra and conifer forests in the surroundings of Barrow, Sodankylä and Tiksi, (c) the BRDF land surface reflectance model PS1 for land surfaces covered by snow fields and glaciers, giving a value of  $A_b(\theta_0 = 60^\circ) = 0.854$ , and used to represent the surface reflectance characteristics observed around Summit in the Arctic and Neumayer, Dome Concordia and South Pole in Antarctica for fresh snow conditions, (d) the BRDF surface

**Table 6**  
Multimodal aerosol extinction models based on the OPAC (Hess et al., 1998) components used to represent 4 Arctic and 4 Antarctic columnar contents of polar aerosol, with (i) the mass percentages of the OPAC components of fine and accumulation/coarse particle modes in the atmospheric column; (ii) the values of real part  $n$  and imaginary part  $k$  of complex refractive index at the 0.55  $\mu\text{m}$  wavelength, (iii) the values of aerosol optical thickness  $\tau(0.50 \mu\text{m})$  and Ångström's exponent  $\alpha$  calculated over the 0.40–0.87  $\mu\text{m}$  wavelength range, and (iv) the values of columnar aerosol single scattering albedo  $\omega(0.55 \mu\text{m})$ . The last three columns provide the values of diurnal average aerosol radiative forcing terms at the TOA-level ( $\Delta F_{\text{TOA}}$ ), at the surface ( $\Delta F_{\text{BOA}}$ ) and within the atmosphere ( $\Delta F_{\text{ATM}}$ ), estimated for the BRDF surface reflectance models OS1 (oceanic), VS1 (vegetation-covered) and PS1, PS2, PS3 and PS4 (polar ice- and snow-covered) determined by Tomasi et al. (2014). The acronym BG stands for “background”. The OPAC aerosol components are indicated by the acronyms WASO (water-soluble), SSAM (sea-salt accumulation mode), SSCM (sea-salt coarse mode), INSO (insoluble), SOOT (soot), and MITR (mineral-transported).

Aerosol type	Mass percentages of the basic OPAC components calculated for relative humidity = 50% to give form to the fine and accumulation/coarse particle modes						Particulate matter refractive index parts		Aerosol optical thickness $\tau(0.50\text{ }\mu\text{m})$	Exponent $\alpha$	$\omega$ (0.55 $\mu\text{m}$ )	BRDF surface reflectance model	Diurnal average aerosol radiative forcing ( $\text{W m}^{-2}$ )		
	Fine particle modes		Accumulation/coarse particle modes												
	WASO	SOOT	SSAM	SSCM	INSO	MITR	$n(0.50\text{ }\mu\text{m})$	$k(0.50\text{ }\mu\text{m})$					$\Delta F_{TOA}$	$\Delta F_{BOA}$	$\Delta F_{ATM}$
Winter–spring Arctic haze (Barrow)	95.8	4.2	22.9	37.7	39.4	–	1.399	$3.3\text{ }10^{-3}$	0.116	1.28	0.840	OS1 PS1 PS2	–5.5 +9.0 +8.8	+6.5 +0.0 +0.1	–12.0 +8.9 +8.7
Winter–spring Arctic haze (Ny-Ålesund)	98.0	2.0	–	90.9	9.1	–	1.424	$7.3\text{ }10^{-3}$	0.080	1.29	0.949	OS1 PS3	–5.3 +1.0	–0.6 –0.4	–4.7 +1.4
Winter–spring Arctic haze (Sodankylä)	95.3	4.7	94.8	5.2	–	–	1.399	$3.9\text{ }10^{-3}$	0.066	1.25	0.840	OS1 VS1 PS2	–7.7 –3.5 +2.2	–1.1 –5.3 –0.3	–6.6 +1.8 +2.5
Background summer aerosol (Barrow)	96.8	3.2	11.0	43.6	45.4	–	1.444	$9.2\text{ }10^{-3}$	0.078	1.40	0.978	OS1 VS1	–9.2 –4.2	–1.9 –6.5	–7.3 +2.3
Background summer aerosol (Ny-Ålesund)	98.0	2.0	–	50.0	50.0	–	1.461	$7.9\text{ }10^{-3}$	0.041	1.20	0.966	OS1 PS4	–7.2 +1.0	+1.5 –2.3	–8.6 +3.4
Arctic dense summer aerosol (Ny-Ålesund)	97.6	2.4	6.3	59.7	34.0	–	1.437	$3.7\text{ }10^{-3}$	0.120	1.00	0.852	OS1 PS4	–10.4 +13.0	+4.2 –5.2	–14.6 +18.2
Background summer aerosol (Summit)	98.0	2.0	–	50.0	50.0	–	1.449	$8.8\text{ }10^{-3}$	0.039	1.48	0.969	PS1	+2.2	–0.2	+2.5
Background summer aerosol (Sodankylä)	98.0	2.0	–	50.0	50.0	–	1.452	$8.6\text{ }10^{-3}$	0.060	1.42	0.965	OS1 VS1 PS2	–6.5 –3.0 +3.0	–1.6 –5.5 –0.4	–4.9 +2.4 +3.4
Background summer aerosol (Tiksi)	98.0	2.0	–	50.0	50.0	–	1.444	$9.2\text{ }10^{-3}$	0.085	1.60	0.977	OS1 VS1	–10.3 –5.6	–1.6 –9.0	–8.7 +3.3
Asian dust (Barrow)	100.0	–	5.8	2.4	56.5	35.3	1.527	$6.3\text{ }10^{-3}$	0.200	0.80	0.858	OS1 PS2	–9.3 +18.5	+16.0 +0.3	–25.3 +18.2
Boreal forest fire smoke (Barrow)	95.5	4.5	21.7	26.1	52.2	–	1.469	$2.5\text{ }10^{-3}$	0.300	1.20	0.758	OS1 VS1	–32.9 –20.2	–6.7 –28.6	–26.2 +8.3
Background austral summer aerosol (Mario Zucchelli)	99.5	0.5	–	73.9	26.1	–	1.468	$2.3\text{ }10^{-3}$	0.030	0.90	0.964	OS1 PS2	–6.2 +2.0	+0.9 –0.1	–7.1 +2.1
Background austral summer aerosol (Neumayer)	99.7	0.3	–	85.6	14.4	–	1.457	$1.3\text{ }10^{-3}$	0.043	0.68	0.975	OS1 PS1 PS2	–8.2 +1.9 +2.1	+1.4 –0.2 +0.0	–9.6 +2.1 +2.1
Background austral summer aerosol (Dome Concordia)	100.0	–	4.5	–	–	95.5	1.441	$2.0\text{ }10^{-3}$	0.019	1.77	0.999	PS1 PS2	+0.4 +0.6	+0.2 +0.4	+0.2 +0.2
Background austral summer aerosol (South Pole)	99.6	0.4	–	83.6	16.4	–	1.445	$3.2\text{ }10^{-3}$	0.018	1.49	0.988	PS1 PS2	+0.6 +0.7	–0.1 –0.1	+0.7 +0.8

albedo model PS2, yielding a value of  $A_b(\theta_0 = 60^\circ) = 0.775$ , which was adopted to represent the surface reflectance characteristics for land areas covered by slightly polluted snow (at Sodankylä) and not entirely snow-covered areas (Mario Zucchelli, Neumayer, and other coastal sites), (e) the BRDF model PS3, giving  $A_b(\theta_0 = 60^\circ) = 0.564$ , which was chosen to represent the surface albedo characteristics observed over Spitsbergen in late winter and early spring, and (f) the BRDF model PS4, yielding  $A_b(\theta_0 = 60^\circ) = 0.329$ , which realistically represents the mixed ice-covered and ice-free land areas around Ny-Ålesund in late spring and summer.

- (vi) Calculations of the daily time-patterns of instantaneous and diurnally averaged DARFs were made using the 6S (Vermote et al., 1997a) radiative transfer code for: (a) the values of  $\tau(0.50 \mu\text{m})$  and  $\alpha(0.40\text{--}0.87 \mu\text{m})$  defined in Table 6 for the various aerosol types and assumed to be stable from sunrise to sunset, (b) the values of angle  $\theta_0$  calculated at the various hours of the day, for the above stations and seasonal periods, (c) the multimodal size-distribution curves determined at step (iii), (d) the spectral values of  $\omega(\lambda)$  for each of the multimodal size-distribution curves determined at step (iv), and (e) the surface albedo models chosen at step (v) for the various Arctic and Antarctic sites. The time-patterns of  $\Delta F_{TOA}(t)$ ,  $\Delta F_{BOA}(t)$  and  $\Delta F_{ATM}(t)$  were then integrated to calculate the daily values of  $\Delta F_{TOA}$ ,  $\Delta F_{BOA}$  and  $\Delta F_{ATM}$  given in Table 6 for the various aerosol types and BRDF surface albedo models.

Examining the results given in Table 6, it can be seen that  $\Delta F_{TOA}$  varies appreciably at Barrow as one passes from the OS1 to VS1 model in the Asian dust (AD) case, and from the OS1 to PS2 model in the BFF smoke case, while only limited variations of  $\Delta F_{TOA}$  from about  $-10 \text{ W m}^{-2}$  to no more than  $+10 \text{ W m}^{-2}$  were obtained for the background summer aerosol and Arctic haze cases considered at the 5 above-chosen Arctic sites. Similar features were also noted for  $\Delta F_{BOA}$ , illustrating larger variations in the AD and BFF aerosol cases monitored at Barrow, and mainly ranging from  $-5$  to  $+5 \text{ W m}^{-2}$  in all the background summer aerosol and Arctic haze cases. Correspondingly, rather large variations in  $\Delta F_{ATM}$  were obtained not only for the Barrow AD and BFF cases but also for the Arctic haze cases observed at Barrow and Ny-Ålesund for  $\tau(0.50 \mu\text{m}) > 0.10$ . In particular, we have estimated an Asian dust value of  $\Delta F_{TOA} \approx 9 \text{ W m}^{-2}$  for  $\tau(0.50 \mu\text{m}) = 0.20$  measured at Barrow.

The diurnally averaged DARF terms  $\Delta F_{TOA}$ ,  $\Delta F_{BOA}$  and  $\Delta F_{ATM}$  given in Table 6 for four Antarctic background austral summer aerosol cases indicate that larger variations have been estimated at Mario Zucchelli and Neumayer, passing from the low surface reflectance oceanic model OS1 to the land surface albedo model PS2 characterised by highly reflecting and snow-covered surfaces. Conversely, very limited variations in the three DARF terms have been obtained at the four Antarctic sites, when passing from one PS land surface albedo model to another, since they all pertain to land surfaces covered by glaciers and snow fields that do not exhibit marked differences in their reflectance characteristics. Actually, it is important to mention that the above DARF evaluations may be affected by large uncertainties, associated with the numerous approximations made in the above calculations when: (a) assuming constant time-patterns of AOT and stable aerosol optical parameters throughout the day, (b) neglecting the occurrence of variations in the scattering, absorption and extinction properties of aerosol with height, and assuming that the vertical profiles of such optical parameters did not exhibit multi-layered features, (c) using simplified radiative transfer codes in a cloud-free atmosphere, which can lead to significant errors in estimating the DARF effects, as pointed out by Bush and Valero (2003), and (d) choosing inappropriate surface reflectance models to represent the surface albedo characteristics, as would especially be the case for the VS1 and OS1 models, which may differ

considerably in some cases from the real surface conditions, as pointed out by Stone et al. (2008). With regard to this, calculations of the DARF effects made by Tomasi et al. (2014) using the sets of four oceanic surface (OS) and four vegetation-covered (VS) BRDF models indicate that changes varying from 10% to 50% may affect the calculations of  $\Delta F_{TOA}$  and  $\Delta F_{BOA}$ , and consequently even greater differences can be found in evaluating  $\Delta F_{ATM}$ . Therefore, it is fair to highlight that the present evaluations of  $\Delta F_{TOA}$ ,  $\Delta F_{BOA}$  and  $\Delta F_{ATM}$  obtained using the OS1 calm-wind ocean model could differ appreciably from those occurring for stronger winds causing higher surface reflectance conditions in sea areas.

Calculations of the DARF efficiency parameters  $E_{TOA}$ ,  $E_{BOA}$  and  $E_{ATM}$  were finally made by dividing the values of  $\Delta F_{TOA}$ ,  $\Delta F_{BOA}$  and  $\Delta F_{ATM}$  given in Table 6 for the various polar aerosol types by the corresponding mean values of  $\tau(0.50 \mu\text{m})$ . The evaluations of  $E_{TOA}$ ,  $E_{BOA}$  and  $E_{ATM}$  are shown in Fig. 28 as a function of the broadband albedo  $A_b(\theta_0 = 60^\circ)$  determined for the various BRDF surface reflectance models chosen above. The values of  $E_{TOA}$ ,  $E_{BOA}$  and  $E_{ATM}$  obtained at the five Arctic sites for various aerosol types indicate that DARF efficiencies are subject to large variations when passing from the low surface albedo characteristics of the VS1 and OS1 models to the high reflectance surfaces of the PS models. The results shown in Fig. 28 indicate that:

- (a)  $E_{TOA}$  increases from less than  $-100 \text{ W m}^{-2}$  over the VS1 surface (for BG summer aerosol over sea, at Ny-Ålesund) to more than  $+100 \text{ W m}^{-2}$  over the PS4 surface (for Arctic dense summer aerosol at Ny-Ålesund), and assumes slightly positive values as the broadband albedo increases from 0.56 to 0.85, ranging from about  $+30 \text{ W m}^{-2}$  (over the PS2 surface for Arctic haze at Sodankylä and for BG summer aerosol at Dome Concordia) to no more than  $+92 \text{ W m}^{-2}$  (over the PS2 surface, for Asian dust at Barrow). These estimates had relative standard deviations varying on average from 10% over the PS4 surface to 50% over the VS1 and OS1 surfaces (i.e. from 6 to  $26 \text{ W m}^{-2}$ ).
- (b)  $E_{BOA}$  varies from less than  $-100 \text{ W m}^{-2}$  over the VS1 surface (for BG summer aerosol at Tiksi) to around  $+80 \text{ W m}^{-2}$  over the OS1 surface (for Arctic haze at Barrow). The estimates of  $E_{BOA}$  obtained for the high-reflectance PS surface reflectance models did not vary by much with the aerosol type, ranging from  $-57 \text{ W m}^{-2}$  (for Arctic BG aerosol at Ny-Ålesund) to  $+20 \text{ W m}^{-2}$  (for Antarctic BG summer aerosol at Dome Concordia).
- (c)  $E_{ATM}$  varies from about  $-240 \text{ W m}^{-2}$  over the OS1 surface (for Antarctic BG summer aerosol at Mario Zucchelli) to more than  $+150 \text{ W m}^{-2}$  over the PS4 surface (for Arctic dense summer aerosol at Ny-Ålesund). Fig. 28 shows that  $E_{ATM}$  exhibits a large range over the VS1 and OS1 surfaces, and then assumes stable and positive values over the PS surfaces, varying from  $+10 \text{ W m}^{-2}$  (for Antarctic BG summer aerosol at Dome Concordia) to  $+151 \text{ W m}^{-2}$  over the PS4 surface (for dense Arctic haze at Ny-Ålesund).

The present DARF efficiency evaluations are affected by considerable uncertainties, since they were determined with relative standard deviations varying from about  $\pm 10\%$  (over the PS4 surface) to around  $\pm 50\%$  (over the VS1 and OS1 surfaces).

The results shown in Fig. 28 have been obtained for various Arctic and Antarctic aerosol types with values of  $\omega(0.55 \mu\text{m})$  ranging from about 0.76 (for BFF smoke at Barrow) to nearly 1.00 (for Antarctic background aerosol at Dome Concordia). The value of  $E_{TOA}$  for the BFF smoke load observed at Barrow was found to be of  $-68 \pm 27 \text{ W m}^{-2}$  over the tundra (VS1) surface, while Stone et al. (2008) estimated an average efficiency value of  $-20 \text{ W m}^{-2}$  in summer 2004. The corresponding value of  $E_{BOA}$  was estimated by us at  $-95 \pm 36 \text{ W m}^{-2}$ , while Stone et al. (2008) estimated a lower average efficiency of about  $-40 \text{ W m}^{-2}$ . Thus, we obtained a value of  $E_{ATM}$  equal to  $+27 \pm 63 \text{ W m}^{-2}$ , against an estimate of  $+20 \text{ W m}^{-2}$  by Stone et al. (2008), resulting in an atmospheric warming rate of about 1 K per day.



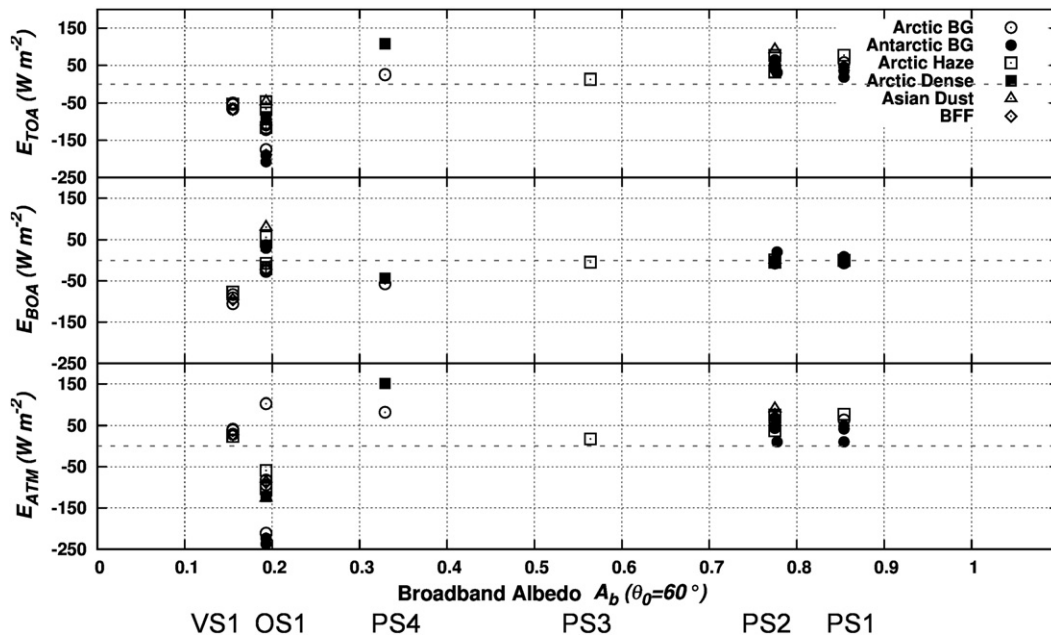


**Fig. 28.** Scatter plots of the daily mean values of DARF efficiencies  $E_{TOA}$  at the TOA-level (upper part),  $E_{BOA}$  at the BOA-level (middle part), and  $E_{ATM}$  in the atmosphere (lower part) shown versus the broadband albedo calculated by Tomasi et al. (2014) at solar zenith angle  $\theta_0 = 60^\circ$ , for the BRDF oceanic surface (OS1), vegetation-covered surface (VS1) and snow-covered polar surface (PS1, PS2, PS3 and PS4) models, and for the 15 polar aerosol types defined in Table 6 and represented using different symbols.

## 7. Conclusions

Monthly mean values of  $\tau(0.50 \mu\text{m})$  and Ångström exponent  $\alpha$  determined from multi-year sets of ground-based sun-photometer measurements at 21 polar sites, yielded a comprehensive picture of atmospheric turbidity conditions due to polar aerosols. The results are presented as a function of the winter–spring and summer periods over the whole Arctic region and include observations conducted in Alaska, Northern Canada, Greenland, Svalbard, Northern Scandinavia and Northern-Central Siberia. The analysis of the measurements acquired at the 12 Arctic sites listed in Table 1 highlighted the seasonality of columnar aerosol extinction parameters, showing that  $\alpha$  ranges mainly from 1.0 to 1.6 throughout the year at all stations, and  $\tau(0.50 \mu\text{m})$  values were mainly lower than 0.08 in summer (for background aerosol) and appreciably higher during the winter–spring period. The latter phenomenon is associated with the occurrence of dense Arctic haze episodes that are often observed at remote Arctic sites as the result of the transport of anthropogenic polluted aerosols from the industrialised and most densely populated areas of mid-latitude North America, Europe and Asia.

Sun-photometer measurements collected during the Antarctic summer were analysed for six coastal sites (Marambio, Neumayer, Novolazarevskaya, Mirny, Syowa, Mario Zucchelli), one mid-altitude station (Troll) and two high-altitude bases on the Antarctic Plateau (Dome Concordia and South Pole). Monthly mean  $\tau(0.50 \mu\text{m})$  values usually ranged from less than 0.02 on the Antarctic Plateau to no more than 0.06 at the coastal stations, with  $\alpha$  decreasing respectively from extremes of 1.8 (at South Pole and Dome Concordia, for aerosols dominated by nss sulphates), to around 0.6 at Mario Zucchelli, Neumayer and the other coastal sites (where aerosol light extinction is predominantly influenced by sea-salt particles).

Ship-borne sun-photometer measurements were conducted during 14 spring and summer AERONET/MAN cruises across the Greenland Sea and Norwegian Sea, the West Siberian Sea and the North American Arctic Ocean. The results yielded monthly mean estimates of  $\tau(0.50 \mu\text{m})$  and  $\alpha$  that were found to be comparable with results obtained from ground-based sun-photometer measurements taken at the stations located on the coasts of the same oceanic sectors during the March to September

period, thus confirming the covariance features of  $\tau(0.50 \mu\text{m})$  and  $\alpha$  determined at the ground-based sun-photometer sites. The analysis of ship-borne sun-photometer measurements performed during the 18 AERONET/MAN cruises conducted in the coastal and off-shore Antarctic areas of the Indian, Pacific and Atlantic Oceans and along the Antarctic Peninsula coasts showed that the monthly mean values of  $\tau(0.50 \mu\text{m})$  varied between the extremes of 0.02 and 0.06 from December to April, while decreasing from 0.12 in October to 0.07 in November for measurements acquired around the Antarctic Peninsula. The large magnitude AOTs in the latter case were likely the result of stronger winds from the northern and western quadrants producing more sea-salt particles, which are transported towards the continent, while the rapidly decreasing trend results from a rapid decrease in the amplitude of these winds (a contention that is further supported by the corresponding increase in  $\alpha$  values, between October and January, while  $\tau(0.50 \mu\text{m})$  systematically decreases). In more general terms we would argue that scattergrams of  $\alpha$  versus  $\tau(0.50 \mu\text{m})$  for the ensemble of both land-based and ship-borne based sun-photometry showed a roughly inverse relationship of high  $\alpha$ , small  $\tau(0.50 \mu\text{m})$  to low  $\alpha$ , high  $\tau(0.50 \mu\text{m})$  that was representative of a progressive transformation from nuclei dominated nss sulphates above the Antarctic Plateau to sea-salt dominated aerosols for coastal sites.

The vertical distribution of the aerosol extinction coefficient was investigated with ground-based lidars at Arctic and Antarctic sites. In particular, the monthly mean vertical profiles of backscatter coefficient, along with lidar ratio trends and depolarisation ratio covariance with backscattering coefficient were illustrated for tropospheric altitudes using data acquired at Ny-Ålesund by the AWI KARL lidar from 1 November, 2012, to 31 October, 2013. As part of this investigation, we illustrated the seasonal variations of integrated backscatter coefficient and lidar ratio, as influenced by Arctic haze episodes in late winter and spring, and the background aerosol in summer.

Evaluations of AOT in the visible have been obtained using the operational algorithms applied to MODIS (Levy et al., 2013; Glantz et al., 2014), MISR (Diner et al., 2005b; Kahn et al., 2010) and AATSR (Holzer-Popp et al., 2013) satellite observations, which were found to substantially agree with the values of AOT obtained from the ground-based and ship-borne sun-photometer measurements conducted in

the Arctic and Antarctic open-water regions. Reliable evaluations of  $\tau(0.55 \mu\text{m})$  have also been retrieved from the AATSR measurements recorded over the Arctic oceanic and land regions covered by sea ice, land ice and snow using observations taken in different spectral channels (Istomina et al., 2011), and by using the DVMS method (Mei et al., 2013b). These retrievals allow the aerosol spatial distribution (e.g., pollution events) to be analysed on short term scales, but may contain an AOT offset due to many challenges connected to virtually unknown surface types and aerosol optical properties. The global application of these procedures is at present a challenging problem because of the very high sensitivity of the retrievals to unscreened thin clouds. In fact, these data are already affected by large uncertainties and need to be further validated, to overcome the errors that may arise from cloud contamination and the complex picture of polar conditions (low values of AOT, various aerosol/cloud types, atmospheric inversions, variable features of snow- and ice-covered surface reflectance,...).

The main characteristics of multimodal particle size-distribution curves have been defined by: (i) taking into account the in-situ aerosol sampling measurements conducted at various Arctic sites (Barrow, Ny-Ålesund, Sodankylä) and Antarctic sites (Mario Zucchelli, Neumayer, Aboa, South Pole, Dome Concordia), and (ii) assuming that the overall size-distribution curves determined at the various sites consist in general of a nuclei mode and an accumulation or coarse particle mode, linearly combined to give a bimodal aerosol columnar load for each value of  $\alpha$  obtained from the field measurements. Eight log-normal curves were defined for the Arctic stations on the basis of in-situ particle samples collected for Arctic haze, summer background aerosol, Asian dust and BFF smoke. They can be used for each spectral set of sun-photometer  $\tau(\lambda)$  measurements to fit the derived value of  $\alpha$ . The radiative parameters of the eight unimodal curves were defined by taking into account the complex refractive index and single scattering albedo derived from in-situ measurements conducted with nephelometers and aethalometers and/or using the simulations of the aerosol optical properties made with the aerosol extinction models given by the 6S code. Six log-normal curves were defined to represent the unimodal size-distribution curves of Antarctic nuclei, accumulation and coarse particles, using field data obtained from the aerosol collected at coastal and high-altitude sites. The optical properties of particulate matter were defined according to the data provided by the in-situ active remote sensing measurements, and used to determine the optical characteristics of six Antarctic log-normal size-distribution curves shown in Table 5.

Assumptions about the aerosol optical properties are totally based on the particulate chemical composition measured at the ground and, therefore, may differ appreciably from airborne particles suspended within the upper layers of the atmosphere in all cases of aerosol transport from remote areas (like Arctic haze, Asian dust, and BFF smoke), as shown for instance by the PAMARCMiP airborne measurements conducted in April 2009 (Stone et al., 2010). However, the best-fit procedure combining the nuclei mode with the accumulation or coarse particle mode to fit the value of  $\alpha$  will have probably allowed us to evaluate the average spectral features of the column loading consisting of larger particles.

The bimodal size-distribution curves of Arctic and Antarctic aerosol obtained as linear combinations of the nuclei or fine particle modes and accumulation or coarse particle modes have been defined by varying their columnar number contents until a best-fit value of  $\alpha$  was obtained for each spectral series of  $\tau(\lambda)$ . All these bimodal models were assumed to exhibit the well-defined optical properties given in Table 5 and to represent the most relevant optical characteristics of Arctic and Antarctic columnar aerosol. Additional realistic multimodal extinction models of nuclei, accumulation and coarse particles have been defined as linear combinations of the OPAC components proposed by Hess et al. (1998), which fit the mean values of  $\alpha$  determined for different columnar aerosol types. Using these multimodal aerosol extinction models, instantaneous and diurnally averaged DARF effects induced by atmospheric aerosol at the TOA- and BOA-levels, and within the

atmosphere have been calculated over sea and land surfaces by using the sets of BRDF surface reflectance models determined by Tomasi et al. (2013) for vegetation-covered, oceanic, and polar snow-covered surfaces. The results indicate that the diurnally averaged DARF terms vary strongly as a function of  $\tau(0.50 \mu\text{m})$ , aerosol single scattering albedo and surface albedo. The corresponding efficiency at the TOA-level was found to increase appreciably as surface albedo over sea and land increases until higher and more stable values over the snow- and ice-covered surfaces are attained. Less variable values and a more limited dependence of the BOA-level DARF efficiency on surface albedo were found, so that the atmospheric DARF efficiency resulted in: (1) a stronger increase when passing from vegetation-covered and oceanic surfaces to surfaces covered only in part by snow, and (2) more stable positive values over the polar surfaces covered by fresh snow and clean glaciers in the Arctic and Antarctic regions.

## Acknowledgements

The present study was developed as a part of the CLIMSLIP (*Climate Impacts of Short-Lived Pollutants in the Polar Regions*) joint project, approved by the European Polar Consortium and coordinated by A. Stohl at NILU (Kjeller, Norway), and supported by the Italian Research Programme in Antarctica (PNRA). The authors gratefully acknowledge the Office of Antarctic Observation of the Japan Meteorological Agency (Tokyo, Japan), for supplying the data-set of EKO sun-photometer measurements carried out at Syowa (Antarctica) from 2000 to 2011. In general we acknowledge the support provided by the AERONET network in the Arctic and Antarctica and the AEROCAN/AERONET sub-network in the Canadian Arctic. The Cimel sun-photometer data at Barrow (Alaska) were collected by the U.S. Department of Energy as part of the Atmospheric Radiation Measurement Program Climate Research Facility (ARM) and processed by AERONET. James H. Butler (Global Monitoring Division, Earth System Research Laboratory (ERL), National Oceanic and Atmospheric Administration (NOAA), Boulder, Colorado, USA) is acknowledged for his effort in establishing and maintaining the activities at the AERONET South Pole Amundsen-Scott base. The colleagues D. G. Chernov, Yu. S. Turchinovich and Victor V. Polkin, (V. E. Zuev Institute of Atmospheric Optics (IAO), Siberian Branch, Russian Academy of Sciences, Tomsk, Russia) are also acknowledged for their participation to field measurements conducted at Barentsburg and in Antarctica. Author's acknowledgements are also due to the managerial and operational support given by M. Fily (LGGE, CNRS, Grenoble, France) at the AERONET Antarctic Dome Concordia station, and to the P.I.s of the AERONET/MAN cruises conducted in the Arctic and Antarctic Oceans, during which Microtops measurements of aerosol optical thickness were performed and examined in the present analysis: Patricia K. Quinn (NOAA Pacific Marine Environmental Laboratory, Seattle, Washington, USA), Andrey Proshutinsky (Woods Hole Oceanographic Institution, Woods Hole, Massachusetts, USA), Carlos Duarte (Instituto Mediterráneo de Estudios Avanzados, Esporles, Mallorca, Spain), Simon Bélanger (Université du Québec, Rimouski, Québec, Canada), Elizabeth A. Reid (Naval Research Laboratory, Monterey, California, USA), Gennadi Milinevsky (Space Physics Laboratory, Taras Shevchenko National University of Kyiv, Kyiv, Ukraine), and Heitor Evangelista (Rio de Janeiro State University, Brazil). The analyses and visualisations used in this paper to obtain the sets of MODIS and MISR daily aerosol optical thickness Level-3 data over the Arctic and Antarctic regions were produced with the Giovanni online data system, developed and maintained by the NASA GES DISC.

## References

- Aaltonen, V., Lihavainen, H., Kerminen, V.-M., Komppula, M., Hatakka, J., Eneroth, K., Kulmala, M., Viisanen, Y., 2006. Measurements of optical properties of atmospheric aerosols in Northern Finland. *Atmos. Chem. Phys.* 6, 1155–1164. <http://dx.doi.org/10.5194/acp-6-1155-2006>.

- Ackerman, S.A., Strabala, K.I., Menzel, W.P., Frey, R.A., Moeller, C.C., Gumley, L.E., 1998. Discriminating clear sky from clouds with MODIS. *J. Geophys. Res.* 103 (D24), 32141–32157. <http://dx.doi.org/10.1029/1998JD000032>.
- Ackerman, S.A., Frey, R., Strabala, K., Liu, Y., Gumley, L., Baum, B., Menzel, P., 2010. Discriminating clear-sky from cloud with MODIS – algorithm theoretical basis document. Products: MOD35. ATBD Reference Number: ATBD-MOD-06, ([http://modis-atmos.gsfc.nasa.gov/MOD35\\_L2/atbd.html](http://modis-atmos.gsfc.nasa.gov/MOD35_L2/atbd.html)).
- Ackermann, J., 1998. The extinction-to-backscatter ratio of tropospheric aerosol: a numerical study. *J. Atmos. Ocean. Technol.* 15 (4), 1043–1050. [http://dx.doi.org/10.1175/1520-0426\(1998\)015<1043:TETBRO>2.0.CO;2](http://dx.doi.org/10.1175/1520-0426(1998)015<1043:TETBRO>2.0.CO;2).
- Allen Jr., R.C., Durkee, P.A., Wash, C.H., 1990. Snow/cloud discrimination with multispectral satellite measurements. *J. Appl. Meteorol.* 29 (10), 994–1004. [http://dx.doi.org/10.1175/1520-0450\(1990\)029<0994:SDWMSM>2.0.CO;2](http://dx.doi.org/10.1175/1520-0450(1990)029<0994:SDWMSM>2.0.CO;2).
- Anderson, T.L., Ogren, J.A., 1998. Determining aerosol radiative properties using the TSI 3563 Integrating Nephelometer. *Aerosol Sci. Technol.* 29, 57–69. <http://dx.doi.org/10.1080/02786829808965551>.
- Ångström, A., 1964. The parameters of atmospheric turbidity. *Tellus* 16, 64–75. <http://dx.doi.org/10.1111/j.2153-3490.1964.tb00144.x>.
- Ansmann, A., Wandinger, U., Riebesell, M., Weikamp, C., Michaelis, W., 1992. Independent measurement of extinction and backscatter profiles in cirrus clouds by using a combined Raman elastic-backscatter lidar. *Appl. Opt.* 31 (33), 7113–7131. <http://dx.doi.org/10.1364/AO.31.007113>.
- Arimoto, R., Hogan, A., Grube, P., Davis, D., Webb, J., Schloesslin, C., Sage, S., Raccach, F., 2004. Major ions and radionuclides in aerosol particles from the South Pole during ISCAT-2000. *Atmos. Environ.* 38, 5473–5484. <http://dx.doi.org/10.1016/j.atmosenv.2004.01.049>.
- Barrie, L.A., Hoff, R.M., Daggupaty, S.M., 1981. The influence of mid-latitude pollution sources on haze in the Canadian Arctic. *Atmos. Environ.* 15 (8), 1407–1419. [http://dx.doi.org/10.1016/0004-6981\(81\)90347-4](http://dx.doi.org/10.1016/0004-6981(81)90347-4).
- Bodhaine, B.A., 1995. Aerosol absorption measurements at Barrow, Mauna Loa and South Pole. *J. Geophys. Res.* 100, 8967–8975. <http://dx.doi.org/10.1029/95JD00513>.
- Bourassa, A.E., Degenstein, D.A., Elash, B.J., Llewellyn, E.J., 2010. Evolution of the stratospheric aerosol enhancement following the eruptions of Okmok and Kasatochi: Odin-OSIRIS measurements. *J. Geophys. Res.* 115 (D2), D00L03. <http://dx.doi.org/10.1029/2009JD013274>.
- Brook, C.A., Cozic, J., Bahreini, R., Froyd, K.D., Middlebrook, A.M., McComiskey, A., Brioude, J., Cooper, O.R., Stohl, A., Aikin, K.C., de Gouw, J.A., Fahey, D.W., Ferrare, R.A., Gao, R.-S., Gore, W., Holloway, J.S., Huebner, G., Jefferson, A., Lack, D.A., Lance, S., Moore, R.H., Murphy, D.M., Nenes, A., Novelli, P.C., Nowak, J.B., Ogren, J.A., Peischl, J., Pierce, R.B., Pilewskie, P., Quinn, P.K., Ryerson, T.B., Schmidt, K.S., Schwarz, J.P., Sodemann, H., Spackman, J.R., Stark, H., Thomson, D.S., Thornberry, T., Veres, P., Watts, L.A., Warneke, C., Wollny, A.G., 2011. Characteristics, sources, and transport of aerosols measured in spring 2008 during the Aerosol, Radiation, and Cloud Processes Affecting Arctic Climate (ARCAP) project. *Atmos. Chem. Phys.* 11 (6), 2423–2453. <http://dx.doi.org/10.5194/acp-11-2423-2011>.
- Bush, B.C., Valero, F.P.J., 2003. Surface aerosol radiative forcing at Gosan during the ACE-Asia campaign. *J. Geophys. Res.* 108 (D23), 8660. <http://dx.doi.org/10.1029/2002JD003233>.
- Campbell, J.R., Tackett, J.L., Reid, J.S., Zhang, J., Curtis, C.A., Hyer, E.J., Sessions, W.R., Westphal, D.L., Prospero, J.M., Welton, E.J., Omar, A.H., Vaughan, M.A., Winker, D.M., 2012. Evaluating nighttime CALIOP 0.532  $\mu\text{m}$  aerosol optical depth and extinction coefficient retrievals. *Atmos. Meas. Tech.* 5 (9), 2143–2160.
- Curier, L., de Leeuw, G., Kolmonen, P., Sundstrom, A.-M., Sogacheva, L., Bennouna, Y., 2009. Aerosol retrieval over land using the (A)ATSR dual-view algorithm. In: Kokhanovsky, A., de Leeuw, G. (Eds.), "Satellite Aerosol Remote Sensing over Land" (A). Praxis Publishing, Chichester (UK), pp. 135–160.
- Damoah, R., Spichtinger, N., Forster, C., James, P., Mattis, I., Wandinger, U., Beirle, S., Wagner, T., Stohl, A., 2004. Around the world in 17 days – hemispheric-scale transport of forest fire smoke from Russia in May 2003. *Atmos. Chem. Phys.* 4, 1311–1321. <http://dx.doi.org/10.5194/acp-4-1311-2004>.
- de Villiers, R.A., Ancellet, G., Pelon, J., Quennehen, B., Schwarzenboeck, A., Gayet, J.F., Law, K.S., 2010. Airborne measurements of aerosol optical properties related to early spring transport of mid-latitude sources into the Arctic. *Atmos. Chem. Phys.* 10 (11), 5011–5030. <http://dx.doi.org/10.5194/acp-10-5011-2010>.
- Delene, D.J., Ogren, J.A., 2002. Variability of aerosol optical properties at four North American surface monitoring sites. *J. Atmos. Sci.* 59, 1135–1150. [http://dx.doi.org/10.1175/1520-0469\(2002\)059<1135:VOAOPA>2.0.CO;2](http://dx.doi.org/10.1175/1520-0469(2002)059<1135:VOAOPA>2.0.CO;2).
- Deuzé, J.L., Bréon, F.M., Devaux, C., Goloub, P., Herman, M., Lafrance, B., Maignan, F., Marchand, A., Nadal, F., Perry, G., Tanré, D., 2001. Remote sensing of aerosol over land surfaces from POLDER-ADEOS-1 polarized measurements. *J. Geophys. Res.* 106 (D5), 4913–4926. <http://dx.doi.org/10.1029/2000JD900364>.
- Devasthale, A., Tjernström, M., Omar, A.H., 2011. The vertical distribution of thin features over the Arctic analysed from CALIPSO observations. Part II: Aerosols. *Tellus* 63B (1), 86–95. <http://dx.doi.org/10.1111/j.1600-0889.2010.00517.x>.
- Di Carmine, C., Campanelli, M., Nakajima, T., Tomasi, C., Vitale, V., 2005. Retrievals of Antarctic aerosol characteristics using a Sun-sky radiometer during the 2001–2002 austral summer campaign. *J. Geophys. Res.* 110, D13202. <http://dx.doi.org/10.1029/2004JD005280>.
- Di Piero, M., Jaeglé, L., Anderson, T.L., 2011. Satellite observations of aerosol transport from East Asia to the Arctic: three case studies. *Atmos. Chem. Phys.* 11, 2225–2243. <http://dx.doi.org/10.5194/acp-11-2225-2011>.
- Diner, D.J., Beckert, J.C., Reilly, T.H., Bruegge, C.J., Conel, J.E., Kahn, R.A., Martonchik, J.V., Ackerman, T.P., Davies, R., Gerstl, S.A.W., Gordon, H.R., Müller, J.-P., Myrneni, R.B., Sellers, P.J., Pinty, B., Verstraete, M.M., 1998. Multi-angle Imaging SpectroRadiometer (MISR) instrument description and experiment overview. *IEEE Trans. Geosci. Remote Sens.* 36 (4), 1072–1087. <http://dx.doi.org/10.1109/36.700992>.
- Diner, D.J., Braswell, B.H., Davies, R., Gobron, N., Hu, J., Jin, Y., Kahn, R.A., Knyazikhin, Y., Loeb, N., Müller, J.-P., Nolin, A.W., Pinty, B., Schaaf, C.B., Seiz, G., Stroeve, J., 2005a. The value of multiangle measurements for retrieving structurally and radiatively consistent properties of clouds, aerosols, and surfaces. *Remote Sens. Environ.* 97 (4), 495–518. <http://dx.doi.org/10.1016/j.rse.2005.06.006>.
- Diner, D.J., Martonchik, J.V., Kahn, R.A., Pinty, B., Gobron, N., Nelson, D.L., Holben, B.N., 2005b. Using angular and spectral shape similarity constraints to improve MISR aerosol and surface retrievals over land. *Remote Sens. Environ.* 94 (2), 155–171. <http://dx.doi.org/10.1016/j.rse.2004.09.009>.
- Dong, X., Xi, B., Crosby, K., Long, C.N., Stone, R.S., Shupe, M.D., 2010. A 10 year climatology of Arctic cloud fraction and radiative forcing at Barrow, Alaska. *J. Geophys. Res.* 115, D17212. <http://dx.doi.org/10.1029/2009JD013489>.
- Dubovik, O., Herman, M., Holdak, A., Lapyonok, T., Tanré, D., Deuzé, J.L., Ducos, F., Sinyuk, A., Lopatin, A., 2011. Statistically optimized inversion algorithm for enhanced retrieval of aerosol properties from spectral multi-angle polarimetric satellite observations. *Atmos. Meas. Tech.* 4, 975–1018. <http://dx.doi.org/10.5194/amt-4-975-2011>.
- Eck, T.F., Holben, B.N., Reid, J.S., Dubovik, O., Smirnov, A., O'Neill, N.T., Slutsker, I., Kinne, S., 1999. Wavelength dependence of the optical depth of biomass burning, urban, and desert dust aerosols. *J. Geophys. Res.* 104 (D24), 31333–31349. <http://dx.doi.org/10.1029/1999JD900923>.
- Eckhardt, S., Hermansen, O., Grythe, H., Fiebig, M., Stebel, K., Cassiani, M., Baekklund, A., Stohl, A., 2013. The influence of cruise ship emissions on air pollution in Svalbard – a harbinger of a more polluted Arctic? *Atmos. Chem. Phys.* 13, 8401–8409. <http://dx.doi.org/10.5194/acp-13-8401-2013>.
- Fattori, I., Becagli, S., Bellandi, S., Castellano, E., Innocenti, M., Mannini, A., Severi, M., Vitale, V., Udidi, R., 2005. Chemical composition and physical features of summer aerosol at Terra Nova Bay and Dome C, Antarctica. *J. Environ. Monit.* 7, 1265–1274.
- Fiebig, M., Lunder, C.R., Stohl, A., 2009. Tracing biomass burning aerosol from South America to Troll Research Station, Antarctica. *Geophys. Res. Lett.* 36, L14815. <http://dx.doi.org/10.1029/2009GL038531>.
- Garrett, T.J., Verzella, L.L., 2008. Looking back: an evolving history of Arctic aerosols. *Bull. Am. Meteorol. Soc.* 89, 299–302. <http://dx.doi.org/10.1175/BAMS-89-3-299>.
- Gesell, G., 1989. An algorithm for snow and ice detection using AVHRR data. An extension to the APOLLO software package. *Int. J. Remote Sens.* 10 (4–5), 897–905. <http://dx.doi.org/10.1080/01431168908903929>.
- Glantz, P., Bourassa, A., Herber, A., Iversen, T., Karlsson, J., Kirkevåg, A., Maturilli, M., Seland, Ø., Stebel, K., Struthers, H., Tesche, M., Thomason, L., 2014. Remote sensing of aerosols in the Arctic for an evaluation of global climate model simulations. *J. Geophys. Res.* 119 (13), 8169–8188. <http://dx.doi.org/10.1002/2013JD021279>.
- Gobbi, G.P., Kaufman, Y.J., Koren, I., Eck, T.F., 2007. Classification of aerosol properties derived from AERONET direct sun data. *Atmos. Chem. Phys.* 7 (2), 453–458. <http://dx.doi.org/10.5194/acp-7-453-2007>.
- Gomez-Chova, L., Camps-Valls, G., Calpe-Maravilla, J., Guanter, L., Moreno, J., 2007. Cloud-screening algorithm for ENVISAT/MERIS multispectral images. *IEEE Trans. Geosci. Remote Sens.* 45 (12), 4105–4118. <http://dx.doi.org/10.1109/TGRS.2007.905312>.
- Govaerts, Y.M., Wagner, S., Lattanzio, A., Watts, P., 2010. Joint retrieval of surface reflectance and aerosol optical depth from MSG/SEVIRI observations with an optimal estimation approach: 1. Theory. *J. Geophys. Res.* 115, D2. <http://dx.doi.org/10.1029/2009JD011779>.
- Grey, W.M.F., North, P.R.J., 2009. Aerosol optical depth from dual-view (A)ATSR satellite observations. In: Kokhanovsky, A.A., de Leeuw, G. (Eds.), *Satellite Aerosol Remote Sensing Over Land*. Springer-Praxis, Berlin. ISBN: 978-3-540-69396-3 (388 pp.).
- Hagler, G.S.W., Bergin, M.H., Smith, E.A., Town, M., Dibb, J.E., 2008. Local anthropogenic impact on particulate elemental carbon concentrations at Summit, Greenland. *Atmos. Chem. Phys.* 8, 2485–2491. <http://dx.doi.org/10.5194/acp-8-2485-2008>.
- Han, W., Stamnes, K., Lubin, D., 1999. Remote sensing of surface and cloud properties in the Arctic from AVHRR measurements. *J. Appl. Meteorol.* 38 (7), 989–1012. [http://dx.doi.org/10.1175/1520-0450\(1999\)038<0989:RSOAC>2.0.CO;2](http://dx.doi.org/10.1175/1520-0450(1999)038<0989:RSOAC>2.0.CO;2).
- Hänel, G., Adam, W., Bundke, U., Komguem, L., Leiterer, U., 1999. Optical properties of boundary layer particles, columnar absorption and direct radiative forcing by particles in the solar spectral region. *J. Aerosol Sci.* 30 (Suppl. 1), S171–S172.
- Hara, K., Osada, K., Kido, M., Hayashi, M., Matsunaga, K., Iwasaka, Y., Yamanouchi, T., Hashida, G., Fukatsu, T., 2004. Chemistry of sea-salt particles and inorganic halogen species in Antarctic regions: compositional differences between coastal and inland stations. *J. Geophys. Res.* 109, D20208. <http://dx.doi.org/10.1029/2004JD004713>.
- Haywood, J., Boucher, O., 2000. Estimates of the direct and indirect radiative forcing due to tropospheric aerosols: a review. *Rev. Geophys.* 38 (4), 513–543. <http://dx.doi.org/10.1029/1999RG000078>.
- Heintzenberg, J., Charlson, R.J., Clarke, A.D., Liousse, C., Ramaswamy, V., Shine, K.P., Wendisch, M., Helas, G., 1997. Measurements and modelling of aerosol single scattering albedo: progress, problems and prospects. *Contrib. Atmos. Phys.* 70, 249–263.
- Herber, A., Thomason, L.W., Gernandt, H., Leiterer, U., Nagel, D., Schulz, K., Kaptur, J., Albrecht, T., Notholt, J., 2002. Continuous day and night aerosol optical depth observations in the Arctic between 1991 and 1999. *J. Geophys. Res.* 107 (D10), 4097. <http://dx.doi.org/10.1029/2001JD000536>.
- Herber, A.B., Haas, C., Stone, R.S., Bottenheim, J.W., Liu, P., Li, S.-M., Staebler, R.M., Strapp, J.W., Dethloff, K., 2012. Regular airborne surveys of Arctic sea ice and atmosphere. *Eos* 93 (4), 41–48. <http://dx.doi.org/10.1029/2012EO040001>.
- Hess, M., Koepke, P., Schult, I., 1998. Optical properties of aerosols and clouds: the software package OPAC. *Bull. Am. Meteorol. Soc.* 79 (5), 831–844. [http://dx.doi.org/10.1175/1520-0477\(1998\)079<0831:OPOAAC>2.0.CO;2](http://dx.doi.org/10.1175/1520-0477(1998)079<0831:OPOAAC>2.0.CO;2).
- Hillamo, R., Allegri, I., Sparapani, R., Kerminen, V.-M., 1998. Mass size distributions and precursors gas concentrations of major inorganic ions in Antarctic aerosol. *Int. J. Environ. Anal. Chem.* 71, 353–372. <http://dx.doi.org/10.1080/03067139808032638>.



- Hirdman, D., Sodemann, H., Eckhardt, S., Burkhardt, J.F., Jefferson, A., Mefford, T., Quinn, P.K., Sharma, S., Ström, J., Stohl, A., 2010. Source identification of short-lived air pollutants in the Arctic using statistical analysis of measurement data and particle dispersion model output. *Atmos. Chem. Phys.* 10, 669–693. <http://dx.doi.org/10.5194/acp-10-669-2010>.
- Hoffmann, A., Ritter, C., Stock, M., Shiobara, M., Lampert, A., Maturilli, M., Orgis, T., Neuber, R., Herber, A., 2009. Ground-based lidar measurements from Ny-Ålesund during ASTAR 2007. *Atmos. Chem. Phys.* 9 (22), 9059–9081. <http://dx.doi.org/10.5194/acp-9-9059-2009>.
- Hoffmann, A., Ritter, C., Stock, M., Maturilli, M., Eckhardt, S., Herber, A., Neuber, R., 2010. Lidar measurements of the Kasatochi aerosol plume in August and September 2008 in Ny-Ålesund, Spitsbergen. *J. Geophys. Res.* 115, D00L12. <http://dx.doi.org/10.1029/2009JD013039>.
- Hoffmann, A., Osterloh, L., Stone, R., Lampert, A., Ritter, C., Stock, M., Tunved, P., Hennig, T., Bockmann, C., Li, S.-M., Eleftheriadis, K., Maturilli, M., Orgis, T., Herber, A., Neuber, R., Dethloff, K., 2012. Remote sensing and in-situ measurements of tropospheric aerosol, a PAMARCMIP case study. *Atmos. Environ.* 52C, 56–66. <http://dx.doi.org/10.1016/j.atmosenv.2011.11.027>.
- Holben, B.N., Eck, T.F., Slutsker, I., Tanré, D., Buis, J.P., Setzer, A., Vermote, E., Reagan, J.A., Kaufman, Y.J., Nakajima, T., Lavenue, F., Jankowiak, I., Smirnov, A., 1998. *AERONET – a federated instrument network and data archive for aerosol characterization*. *Remote Sens. Environ.* 66 (1), 1–16 (doi: S0034-4257(98)00031-5).
- Holzer-Popp, T., de Leeuw, G., Griesfeller, J., Martynenko, D., Klüser, L., Bevan, S., Davies, W., Ducos, F., Deuzé, J.L., Grainger, R.G., Heckel, A., von Hoyningen-Huene, W., Kolmonen, P., Litvinov, P., North, P., Poulson, C.A., Ramon, D., Siddans, R., Sogacheva, L., Tanré, D., Thomas, G.E., Vountas, M., Desclotres, J., Griesfeller, J., Kinne, S., Schulz, M., Pinnock, S., 2013. Aerosol retrieval experiments in the ESA Aerosol\_cci project. *Atmos. Meas. Tech.* 6 (8), 1919–1957. <http://dx.doi.org/10.5194/amt-6-1919-2013>.
- Hori, M., Aoki, T., Tanikawa, T., Motoyoshi, H., Hachikubo, A., Sugiura, K., Yasunari, T.J., Eide, H., Storvold, R., Nakajima, Y., Takahashi, F., 2006. In-situ measured spectral directional emissivity of snow and ice in the 8–14  $\mu\text{m}$  atmospheric window. *Remote Sens. Environ.* 100 (4), 486–502. <http://dx.doi.org/10.1016/j.rse.2005.11.001>.
- Hsu, N.C., Tsay, S.C., King, M.D., Herman, J.R., 2004. Aerosol properties over bright reflecting source regions. *IEEE Trans. Geosci. Remote Sens.* 42 (3), 557–569. <http://dx.doi.org/10.1109/12.975846>.
- Hsu, N.C., Jeong, M.-J., Bettenhausen, C., Sayer, A.M., Hansell, R., Seftor, C.S., Huang, J., Tsay, S.-C., 2013. Enhanced Deep Blue aerosol retrieval algorithm: the second generation. *J. Geophys. Res. (Atmos.)* 118 (16), 9296–9315. <http://dx.doi.org/10.1002/jgrd.50712>.
- Intrieri, J.M., Shupe, M.D., 2004. Characteristics and radiative effects of diamond dust over the Western Arctic ocean region. *J. Clim.* 17 (15), 2953–2960. [http://dx.doi.org/10.1175/1520-0442\(2004\)017<2953:CAREOD>2.0.CO;2](http://dx.doi.org/10.1175/1520-0442(2004)017<2953:CAREOD>2.0.CO;2).
- IPCC, 2013. *Climate Change 2013: The Physical Science Basis, Fifth Assessment Report of the United Nations Intergovernmental Panel on Climate Change (IPCC), Chapter 7, Clouds and Aerosols*. Cambridge University Press, Cambridge (UK) ([http://www.climatechange2013.org/images/report/WG1AR5\\_Chapter07\\_FINAL.pdf](http://www.climatechange2013.org/images/report/WG1AR5_Chapter07_FINAL.pdf)).
- Iqbal, M., 1983. *An Introduction to Solar Radiation*. Academic Press, Toronto (390 pp., see Table 1.2.1 at pages 4–5).
- Istomina, L.G., von Hoyningen-Huene, W., Kokhanovsky, A.A., Burrows, J.P., 2009. Retrieval of aerosol optical thickness in Arctic region using dual-view AATSR observations. *Proceedings of ESA Atmospheric Science Conference, ESA SP-676, Barcelona (Spain), 7–11 September 2009*.
- Istomina, L.G., von Hoyningen-Huene, W., Kokhanovsky, A.A., Burrows, J.P., 2010. The detection of cloud-free snow-covered areas using AATSR measurements. *Atmos. Meas. Tech.* 3, 1005–1017. <http://dx.doi.org/10.5194/amt-3-1005-2010>.
- Istomina, L.G., von Hoyningen-Huene, W., Kokhanovsky, A.A., Schultz, E., Burrows, J.P., 2011. Remote sensing of aerosols over snow using infrared AATSR observations. *Atmos. Meas. Tech.* 4, 1133–1145. <http://dx.doi.org/10.5194/amt-4-1133-2011>.
- Justice, C.O., Vermote, E., Townshend, J.R.G., Defries, R., Roy, D.P., Hall, D.K., Salomonson, V.V., Privette, J.L., Riggs, G., Strahler, A., Lucht, W., Myneni, R.P., Knyazikhin, Y., Running, S.W., Nemani, R.R., Wan, Z., Huete, A.R., van Leeuwen, W., Wolfe, R.E., Giglio, L., Muller, J.-P., Lewis, P., Barnsley, M.J., 1998. The Moderate Resolution Imaging Spectroradiometer (MODIS): land remote sensing for global change research. *IEEE Trans. Geosci. Remote Sens.* 36 (4), 1228–1249. <http://dx.doi.org/10.1109/36.701075>.
- Kahn, R.A., Li, W.-H., Martonchik, J.V., Bruegge, C.J., Diner, D.J., Gaitley, B.J., Abdou, W., Dubovik, O., Holben, B., Smirnov, A., Jin, Z., Clark, D., 2005. MISR calibration and implications for low-light-level aerosol retrieval over dark water. *J. Atmos. Sci.* 62 (4), 1032–1052. <http://dx.doi.org/10.1175/JAS3390.1>.
- Kahn, R.A., Gaitley, B.J., Garay, M.J., Diner, D.J., Eck, T.F., Smirnov, A., Holben, B.N., 2010. Multiangle Imaging Spectroradiometer global aerosol product assessment by comparison with the Aerosol Robotic Network. *J. Geophys. Res.* 115, D23209. <http://dx.doi.org/10.1029/2010JD014601>.
- Kahn, R.A., Garay, M.J., Nelson, D.L., Levy, R.C., Bull, M.A., Diner, D.J., Martonchik, J.V., Hansen, E.G., Remer, L.A., Tanré, D., 2011. Response to “Toward unified satellite climatology of aerosol properties. 3. MODIS versus MISR versus AERONET”. *J. Quant. Spectrosc. Radiat. Transf.* 112 (5), 901–909. <http://dx.doi.org/10.1016/j.jqsrt.2009.11.003>.
- Kaufman, Y.J., Tanré, D., Remer, L., Vermote, E.F., Chu, A., Holben, B.N., 1997. Operational remote sensing of tropospheric aerosol over the land from EOS-MODIS. *J. Geophys. Res.* 102 (D14), 17051–17067. <http://dx.doi.org/10.1029/96JD03988>.
- Kerminen, V.-M., Teinilä, K., Hillamo, R., 2000. Chemistry of sea-salt particles in the summer Antarctic atmosphere. *Atmos. Environ.* 34, 2817–2825. [http://dx.doi.org/10.1016/S1352-2310\(00\)00089-3](http://dx.doi.org/10.1016/S1352-2310(00)00089-3).
- Key, J., Barry, R.G., 1989. Cloud cover analysis with Arctic AVHRR data. 1. Cloud detection. *J. Geophys. Res.* 94 (D15), 18521–18535. <http://dx.doi.org/10.1029/JD094iD15p18521>.
- King, M.D., Dubovik, O., 2013. Determination of aerosol optical properties from inverse methods. In: Lenoble, J., Remer, L., Tanré, D. (Eds.), *Aerosol Remote Sensing*. Springer-Verlag, pp. 101–136.
- Knapp, K.R., Vonder Haar, T.H., Kaufman, Y.J., 2002. Aerosol optical depth retrieval from GOES-8: uncertainty study and retrieval validation over South America. *J. Geophys. Res. (Atmos.)* 107 (D7). <http://dx.doi.org/10.1029/2001JD000505> (AAC 2-1-AAC 2-12).
- Koponen, I.K., Virkkula, A., Hillamo, R., Kerminen, V.-M., Kulmala, M., 2003. Number size distributions and concentrations of the continental summer aerosols in Queen Maud Land, Antarctica. *J. Geophys. Res.* 108 (D18), 4587. <http://dx.doi.org/10.1029/2003JD003614>.
- Lampert, A., Ehrlich, A., Dörnbrack, A., Jourdan, O., Gayet, J.-F., Mioche, G., Shcherbakov, V., Ritter, C., Wendisch, M., 2009. Microphysical and radiative characterization of a sub-visible midlevel Arctic ice cloud by airborne observations a case study. *Atmos. Chem. Phys.* 9 (8), 2647–2661. <http://dx.doi.org/10.5194/acp-9-2647-2009>.
- Lampert, A., Ritter, C., Hoffmann, A., Gayet, J.-F., Mioche, G., Ehrlich, A., Doernbrack, A., Wendisch, M., Shiobara, M., 2010. Lidar characterization of the Arctic atmosphere during ASTAR 2007: four cases studies of boundary layer, mixed-phase and multi-layer clouds. *Atmos. Chem. Phys.* 10 (6), 2847–2866. <http://dx.doi.org/10.5194/acp-10-2847-2010>.
- Law, K.S., Stohl, A., Quinn, P.K., Brock, C., Burkhardt, J., Paris, J.-D., Ancellet, G., Singh, H.B., Roiger, A., Schlager, H., Dibb, J., Jacob, D.J., Arnold, S.R., Pelon, J., Thomas, J.L., 2014. Arctic air pollution: 1 New insights from POLARCAT-IPY. *Bull. Am. Meteorol. Soc.* 95. <http://dx.doi.org/10.1175/BAMS-D-13-00017.1> (in press).
- Levy, R.C., Remer, L.A., Mattoo, S., Vermote, E.F., Kaufman, Y.J., 2007. Second-generation operational algorithm: Retrieval of aerosol properties over land from inversion of Moderate Resolution Imaging Spectroradiometer spectral reflectance. *J. Geophys. Res.* 112, D13211. <http://dx.doi.org/10.1029/2006JD007811>.
- Levy, R.C., Remer, L.A., Kleidman, R.G., Mattoo, S., Ichoku, C., Kahn, R., Eck, T.F., 2010. Global evaluation of the Collection 5 MODIS dark-target aerosol products over land. *Atmos. Chem. Phys.* 10, 10399–10420. <http://dx.doi.org/10.5194/acp-10-10399-2010>.
- Levy, R.C., Mattoo, S., Munchak, L.A., Remer, L.A., Sayer, A.M., Patadia, F., Hsu, N.C., 2013. The Collection 6 MODIS aerosol products over land and ocean. *Atmos. Meas. Tech.* 6, 2989–3034. <http://dx.doi.org/10.5194/amt-6-2989-2013>.
- Liu, Y., Key, J.R., Frey, R.A., Ackerman, S.A., Menzel, W.P., 2004. Nighttime polar cloud detection with MODIS. *Remote Sens. Environ.* 92 (2), 181–194. <http://dx.doi.org/10.1016/j.rse.2004.06.004>.
- Lubin, D., Satheesh, S., McFarquar, G., Heymsfield, A., 2002. Longwave radiative forcing of Indian Ocean tropospheric aerosol. *J. Geophys. Res.* 107 (D19), 8004. <http://dx.doi.org/10.1029/2001JD001183>.
- Macdonald, M., Anderson, P., Carrea, L., Dobke, B., Embury, O., Merchant, C., Bensi, P., 2014. Concepts for a geostationary-like polar missions. In: Meynart, R., Neeck, S.P., Shimoda, H. (Eds.), *Sensors, Systems and Next-Federation Satellites XVIII. Proceedings of the SPIE 2014 vol. 9421*. ISBN: 9781628413045.
- Martonchik, J.V., Diner, D.J., Kahn, R.A., Ackerman, T.P., Verstraete, M.M., Pinty, B., Gordon, H.R., 1998a. Techniques for the retrieval of aerosol properties over land and ocean using multi-angle imagery. *IEEE Trans. Geosci. Remote Sens.* 36 (4), 1212–1227. <http://dx.doi.org/10.1109/36.701027>.
- Martonchik, J.V., Diner, D.J., Pinty, B., Verstraete, M.M., Myneni, R.B., Knyazikhin, Y., Gordon, H.R., 1998b. Determination of land and ocean reflective, radiative, and biophysical properties using multiangle imaging. *IEEE Trans. Geosci. Remote Sens.* 36 (4), 1266–1281. <http://dx.doi.org/10.1109/36.701077>.
- Martonchik, J.V., Diner, D.J., Crean, K.A., Bull, M.A., 2002. Regional aerosol retrieval results from MISR. *IEEE Trans. Geosci. Remote Sens.* 40 (7), 1520–1531. <http://dx.doi.org/10.1109/TGRS.2002.801142>.
- Mazzola, M., Stone, R.S., Herber, A., Tomasi, C., Lupi, A., Vitale, V., Lanconelli, C., Toledano, C., Cachorro, V.E., O'Neill, N.T., Shiobara, M., Aaltonen, V., Stebel, K., Zielinski, T., Petelski, T., Ortiz de Galisteo, J.P., Torres, B., Berjon, A., Goloub, P., Li, Z., Blarel, L., Abboud, I., Cuevas, E., Stock, M., Schulz, K.-H., Virkkula, A., 2012. Evaluation of sun photometer capabilities for retrievals of aerosol optical depth at high latitudes: The POLAR-AOD intercomparison campaigns. *Atmos. Environ.* 52C, 1–14. <http://dx.doi.org/10.1016/j.atmosenv.2011.07.042>.
- Mei, L., Xue, Y., 2013. Aerosol optical thickness retrieval over snow-covered surface using AATSR data. *The 2013 IEEE International Geoscience and Remote Sensing Symposium (IGARSS)*, Melbourne, Australia, 21–26 July 2013.
- Mei, L., Xue, Y., de Leeuw, G., Holzer-Popp, T., Guang, J., Li, Y., Yang, L., Xu, H., Xu, X., Li, C., Wang, Y., Wu, C., Hou, T., He, X., Liu, J., Dong, J., Chen, Z., 2012. Retrieval of aerosol optical depth over land based on a time series technique using MSG/SEVIRI data. *Atmos. Chem. Phys.* 12, 9167–9185. <http://dx.doi.org/10.5194/acp-12-9167-2012>.
- Mei, L., Xue, Y., de Leeuw, G., von Hoyningen-Huene, W., Kokhanovsky, A.A., Istomina, L., Guang, J., Burrows, J.P., 2013a. Aerosol optical depth retrieval in the Arctic region using MODIS over snow. *Remote Sens. Environ.* 128, 234–245. <http://dx.doi.org/10.1016/j.rse.2012.10.009>.
- Mei, L., Xue, Y., Kokhanovsky, A.A., von Hoyningen-Huene, W., Istomina, L., de Leeuw, G., Burrows, J.P., Guang, J., Jing, Y., 2013b. Aerosol optical depth retrieval over snow using AATSR data. *Int. J. Remote Sens.* 34 (14), 5030–5041. <http://dx.doi.org/10.1080/01431161.2013.786197>.
- Mei, L., Xue, Y., Kokhanovsky, A.A., von Hoyningen-Huene, W., de Leeuw, G., Burrows, J.P., 2014. Retrieval of aerosol optical depth over land surfaces from AVHRR data. *Atmos. Meas. Tech.* 7, 2411–2420. <http://dx.doi.org/10.5194/amt-7-2411-2014>.
- Mie, G., 1908. Beiträge zur Optik trüber Medien, speziell kolloidaler Metallösungen. *Ann. Phys. Vierte Folge* 25 (3), 377–445.
- Mielonen, T., Levy, R.C., Aaltonen, V., Komppula, M., de Leeuw, G., Huttunen, J., Lihavainen, H., Kolmonen, P., Lehtinen, K.E.J., Arola, A., 2011. Evaluating the assumptions of

- surface reflectance and aerosol type selection within the MODIS aerosol retrieval over land: the problem of dust type selection. *Atmos. Meas. Tech.* 4, 201–214. <http://dx.doi.org/10.5194/amt-4-201-2011>.
- Mielonen, T., Aaltonen, V., Lihavainen, H., Hyvärinen, A.-P., Arola, A., Komppula, M., Kivi, R., 2013. Biomass burning aerosols observed in Northern Finland during the 2010 wildfires in Russia. *Atmosphere* 4, 17–34. <http://dx.doi.org/10.3390/atmos4010017>.
- Minikin, A., Legrand, M., Hall, J., Wagenbach, D., Kleefeld, C., Wolff, E., Pasteur, E.C., Ducroz, F., 1998. Sulfur-containing species (sulfate and MSA) in coastal Antarctic aerosol and precipitation. *J. Geophys. Res.* 103 (D9), 10975–10990. <http://dx.doi.org/10.1029/98JD00249>.
- Mishchenko, M.I., Liu, L., Geogdzhayev, I.V., Travis, L.D., Cairns, B., Lacis, A.A., 2010. Toward unified satellite climatology of aerosol properties. 3. MODIS versus MISR versus AERONET. *J. Quant. Spectrosc. Radiat. Transf.* 111 (4), 540–552. <http://dx.doi.org/10.1016/j.jqsrt.2009.11.003>.
- Mitchell, J.M., 1957. Visual range in the polar regions with particular reference to the Alaskan Arctic. *J. Atmos. Terr. Phys. Spec. Suppl.* 195–211.
- Moore, C.W., Obrist, D., Steffen, A., Staebler, R.M., Douglas, T.A., Richter, A., Nghiem, S.V., 2014. Convective forcing of mercury and ozone in the Arctic boundary layer induced by leads in sea ice. *Nature* 506 (7486), 81–84. <http://dx.doi.org/10.1038/nature12924>.
- Nakajima, T., Yoon, S.C., Ramanathan, V., Shi, G.Y., Takemura, T., Higurashi, A., Takamura, T., Aoki, K., Sohn, B.J., Kim, S.W., Tsuruta, H., Sugimoto, N., Shimizu, A., Tanimoto, H., Sawa, Y., Lin, N.H., Lee, C.T., Goto, D., Schutgens, N., 2007. Overview of the Atmospheric Brown Cloud East Asian Regional Experiment 2005 and a study of the aerosol direct radiative forcing in east Asia. *J. Geophys. Res.* 112, D24S91. <http://dx.doi.org/10.1029/2007JD009009>.
- Negi, H.S., Singh, S.K., Kulkarni, A.V., Semwal, B.S., 2010. Field-based spectral reflectance measurements of seasonal snow cover in the Indian Himalaya. *Int. J. Remote Sens.* 31 (9), 2393–2417. <http://dx.doi.org/10.1080/01431160903002417>.
- Nghiem, S.V., Rigor, I.G., Richter, A., Burrows, J.P., Shepson, P.B., Bottenheim, J., Barber, D.G., Steffen, A., Latonas, J., Wang, F., Stern, G., Clemente-Colón, P., Martin, S., Hall, D.K., Kaleschke, L., Tackett, P., Neumann, G., Asplin, M.G., 2012. Field and satellite observations of the formation and distribution of Arctic atmospheric bromine above a rejuvenated sea ice cover. *J. Geophys. Res.* 117, D17. <http://dx.doi.org/10.1029/2011JD016268>.
- Nordenskiöld, A.E., 1883. Nordenskiöld on the inland ice of Greenland. *Science* 2, 732–739.
- Nott, G.J., Duck, T.J., 2011. Lidar studies of the polar troposphere. *Meteorol. Appl.* 18 (3), 383–405. <http://dx.doi.org/10.1002/met.289>.
- Nyeki, S., Halios, C.H., Baum, W., Eleftheriadis, K., Flentje, H., Gröbner, J., Vuilleumier, L., Wehrli, C., 2012. Ground-based aerosol optical depth trends at three high-altitude sites in Switzerland and southern Germany from 1995 to 2010. *J. Geophys. Res.* 117, D18202. <http://dx.doi.org/10.1029/2012JD017493>.
- O'Neill, N.T., Dubovik, O., Eck, T.F., 2001a. Modified Ångström exponent for the characterization of submicrometer aerosol. *Appl. Opt.* 40 (15), 2368–2375. <http://dx.doi.org/10.1364/AO.40.002368>.
- O'Neill, N.T., Eck, T.F., Holben, B.N., Smirnov, A., Dubovik, O., Royer, A., 2001b. Bimodal size distribution influences on the variation of Ångström derivatives in spectral and optical depth space. *J. Geophys. Res.* 106 (D9), 9787–9806. <http://dx.doi.org/10.1029/2000JD900245>.
- O'Neill, N.T., Eck, T.F., Smirnov, A., Holben, B.N., Thulasiraman, S., 2003. Spectral discrimination of coarse and fine mode optical depth. *J. Geophys. Res.* 108 (D17), 4559. <http://dx.doi.org/10.1029/2002JD002975>.
- O'Neill, N.T., Perro, C., Saha, A., Lesins, G., Duck, T.J., Elooranta, E.W., Nott, G.J., Hoffmann, A., Karumudi, M.L., Ritter, C., Bourassa, A., Abboud, I., Carn, S.A., Savastiouk, V., 2012. Properties of Sarychev sulphate aerosols over the Arctic. *J. Geophys. Res.* 117, D04203. <http://dx.doi.org/10.1029/2011JD016838>.
- Ohno, T., 2005. Aerosol routine observation operated by the Japan Meteorological Agency. "WMO/GAW Experts Workshop on a Global Surface Based Network for Long Term Observations of Column Aerosol Optical Properties", GAW Rep. 162, WMO TD 1287. World Meteorological Organization, Geneva, Switzerland, pp. 70–71.
- O'Neill, N.T., Ignatov, A., Holben, B.N., Eck, T.F., 2000. The lognormal distribution as a reference for reporting aerosol optical depth statistics; Empirical tests using multi-year, multi-site AERONET Sunphotometer data. *Geophys. Res. Lett.* 27 (20), 3333–3336. <http://dx.doi.org/10.1029/2000GL011581>.
- Piel, C., Weller, R., Huke, M., Wagenbach, D., 2006. Atmospheric methane sulfonate and non-sea-salt sulfate records at the European Project for Ice Coring in Antarctica (EPICA) deep-drilling site in Dronning Maud Land, Antarctica. *J. Geophys. Res.* 111, D03304. <http://dx.doi.org/10.1029/2005JD006213>.
- Polissar, A.V., Hopke, P.K., Paatero, P., Malm, W.C., Sisler, J.F., 1998. Atmospheric aerosol over Alaska. 2. Elemental composition and sources. *J. Geophys. Res.* 103, 19045–19057. <http://dx.doi.org/10.1029/98JD01212>.
- Polissar, A.V., Hopke, P.K., Harris, J.M., 2001. Source regions for atmospheric aerosol measured at Barrow, Alaska. *Environ. Sci. Tech.* 35, 4214–4226. <http://dx.doi.org/10.1021/es0107529>.
- Posyniak, M., Markowicz, K., 2009. Measurement of aerosol optical thickness over the Atlantic Ocean and in West Antarctica, 2006–2007. *Acta Geophys.* 57 (2), 494–508. <http://dx.doi.org/10.2478/s11600-009-0002-0>.
- Quinn, P.K., Miller, T.L., Bates, T.S., Ogren, J.A., Andrews, E., Shaw, G.E., 2002. A 3-year record of simultaneously measured aerosol chemical and optical properties at Barrow, Alaska. *J. Geophys. Res.* 107. <http://dx.doi.org/10.1029/2001JD001248> (AAC8–1–AAC8–15).
- Quinn, P., Shaw, G., Andrews, E., Dutton, E.G., Ruoho-Airola, T., Gong, S.L., 2007. Arctic haze: current trends and knowledge gaps. *Tellus* 59B (1), 99–114. <http://dx.doi.org/10.1111/j.1600-0889.2006.00238.x>.
- Radionov, V.F., 2005. Temporal variability of the aerosol optical characteristics of the atmosphere in the Russian Arctic (Historical review). WMO/GAW Experts Workshop on a Global Surface Based Network for Long Term Observations of Column Aerosol Optical Properties, GAW Rep. 162, WMO TD 1287. World Meteorological Organization, Geneva, Switzerland, pp. 82–85.
- Radionov, V.F., Lamakin, M.V., Herber, A., 2002. Changes in the aerosol optical depth of the Antarctic atmosphere. *Izvestia Atmos. Ocean. Phys.* 38, 179–183.
- Rahn, K.A., Borys, R.D., Shaw, G.E., 1977. Asian source of Arctic haze bands. *Nature* 268, 713–715. <http://dx.doi.org/10.1038/268713a0>.
- Ramanathan, V., Crutzen, P.J., Kiehl, J.T., Rosenfeld, D., 2001. Aerosols, climate and the hydrological cycle. *Science* 294, 2119–2124. <http://dx.doi.org/10.1126/science.1064034>.
- Remer, L.A., Kaufman, Y.J., Tanré, D., Mattoo, S., Chu, D.A., Martins, J.V., Li, R.-R., Ichoku, C., Levy, R.C., Kleidman, R.G., Eck, T.F., Vermote, E., Holben, B.N., 2005. The MODIS aerosol algorithm, products, and validation. *J. Atmos. Sci.* 62 (4), 947–973. <http://dx.doi.org/10.1175/JAS3385.1>.
- Remer, L.A., Mattoo, S., Levy, R.C., Munchak, L.A., 2013. MODIS 3 km aerosol product: algorithm and global perspective. *Atmos. Meas. Tech.* 6, 1829–1844. <http://dx.doi.org/10.5194/amt-6-1829-2013>.
- Rogers, R.R., Hostetler, C.A., Hair, J.W., Ferrare, R.A., Liu, Z., Obland, M.D., Harper, D.B., Cook, A.L., Powell, K.A., Vaughan, M.A., Winker, D.M., 2011. Assessment of the CALIPSO Lidar 532 nm attenuated backscatter calibration using the NASA LaRC airborne High Spectral Resolution Lidar. *Atmos. Chem. Phys.* 11, 1295–1311. <http://dx.doi.org/10.5194/acp-11-1295-2011>.
- Rozwadowska, A., Sobolewski, P., 2010. Variability in aerosol optical properties at Hornsund, Spitsbergen. *Oceanologia* 52 (4), 599–620. <http://dx.doi.org/10.5697/oc.52-4.599>.
- Rozwadowska, A., Zielinski, T., Petelski, T., Sobolewski, P., 2010. Cluster analysis of the impact of air back-trajectories on aerosol optical properties at Hornsund, Spitsbergen. *Atmos. Chem. Phys.* 10 (3), 877–893. <http://dx.doi.org/10.5194/acp-10-877-2010>.
- Sakerin, S.M., Kabanov, D.M., Rostov, A.P., Turchinovich, S.A., 2009. Portable Solar Photometer. *Pribery i Tekhnika Eksperimenta (Instrum. Exp. Tech.)* 2, 181–182 (in Russian).
- Sakerin, S.M., Chernov, D.G., Kabanov, D.M., Kozlov, V.S., Panchenko, M.V., Polkin, V.V., Radionov, V.F., 2012. Preliminary results of studying the aerosol characteristics of the atmosphere in the region of Barentsburg, Spitsbergen. *Probl. Arct. Antarct.* 1 (91), 20–31 (in Russian).
- Sakerin, S.M., Andreev, S.Yu., Kabanov, D.M., Nikolashkin, S.V., Prakhov, A.N., Radionov, V.F., Turchinovich, Ju.S., Chernov, D.G., Holben, B.N., Smirnov, A., Sorokin, M.G., 2014. On results of studies of atmospheric aerosol optical depth in Arctic regions. *Atmos. Ocean. Opt.* 27 (5), 413–423 (in Russian).
- Satheesh, S.K., Ramanathan, V., 2000. Large differences in tropical aerosol forcing at the top of the atmosphere and Earth's surface. *Nature* 405, 60–63. <http://dx.doi.org/10.1038/35011039>.
- Saunders, R.W., Kriebel, K.T., 1988. An improved method for detecting clear sky and cloudy radiances from AVHRR data. *Int. J. Remote Sens.* 9 (1), 123–150. <http://dx.doi.org/10.1080/01431168808954841>.
- Sayer, A.M., Hsu, N.C., Bettenhausen, C., Jeong, M.-J., Holben, B.N., Zhang, J., 2012. Global and regional evaluation of over-land spectral aerosol optical depth retrievals from SeaWiFS. *Atmos. Meas. Tech.* 5, 1761–1778. <http://dx.doi.org/10.5194/amt-5-1761-2012>.
- Schlundt, C., Kokhanovsky, A.A., von Hoyningen-Huene, W., Dinter, T., Istomina, L., Burrows, J.P., 2011. Synergetic cloud fraction determination for SCIAMACHY using MERIS. *Atmos. Meas. Tech.* 4 (2), 319–337. <http://dx.doi.org/10.5194/amt-4-319-2011>.
- Schutgens, N.A.J., Nakata, M., Nakajima, T., 2013. Validation and empirical correction of MODIS AOT and AE over ocean. *Atmos. Meas. Tech.* 6, 2455–2475. <http://dx.doi.org/10.5194/amt-6-2455-2013>.
- Schwartz, S.E., Andreae, M.O., 1996. Uncertainty in climate change caused by aerosols. *Science* 272 (5265), 1121–1122. <http://dx.doi.org/10.1126/science.272.5265.1121>.
- Sharma, S., Andrews, E., Barrie, L.A., Ogren, J.A., Lavoué, D., 2006. Variations and sources of equivalent black carbon in the high Arctic revealed by long-term observations at Alert and Barrow: 1989–2003. *J. Geophys. Res.* 111, D14208. <http://dx.doi.org/10.1029/2005JD006581>.
- Shaw, G. E., 1976. Error analysis of multi-wavelength sun photometry 114, 1, 1–14, doi:10.1007/BF00875487
- Shaw, G.E., 1988. Antarctic aerosols: A review. *Rev. Geophys.* 26 (1), 89–112. <http://dx.doi.org/10.1029/RG026i001p00089>.
- Shaw, G.E., 1995. The arctic haze phenomenon. *Bull. Am. Meteorol. Soc.* 76 (12), 2403–2413. [http://dx.doi.org/10.1175/1520-0477\(1995\)076<2403:TAHP>2.0.CO;2](http://dx.doi.org/10.1175/1520-0477(1995)076<2403:TAHP>2.0.CO;2).
- Shi, T., Yu, B., Braverman, A.J., 2002. MISR Cloud Detection over Ice/Snow Using Linear Correlation Matching. Technical Report 630. University of California, Department of Statistics, Berkeley, CA.
- Shi, T., Clothiaux, E.E., Yu, B., Braverman, A.J., Groff, D.N., 2007. Detection of daytime arctic clouds using MISR and MODIS data. *Remote Sens. Environ.* 107 (1–2), 172–184. <http://dx.doi.org/10.1016/j.rse.2006.10.015>.
- Sinyuk, A., Holben, B.N., Smirnov, A., Eck, T.F., Slutsker, I., Schafer, J.S., Giles, D.M., Sorokin, M., 2012. Assessment of error in aerosol optical depth measured by AERONET due to aerosol forward scattering. *Geophys. Res. Lett.* 39, L23806. <http://dx.doi.org/10.1029/2012GL053894>.
- Six, D., Fily, M., Blarel, L., Goloub, P., 2005. First aerosol optical thickness measurements at Dome C (East Antarctica), summer season 2003–2004. *Atmos. Environ.* 39 (28), 5041–5050. <http://dx.doi.org/10.1016/j.atmosenv.2005.05.010>.
- Smirnov, A., Holben, B.N., Eck, T.F., Dubovik, O., Slutsker, I., 2000. Cloud-screening and quality control algorithms for the AERONET database. *Remote Sens. Environ.* 73 (3), 337–349. [http://dx.doi.org/10.1016/S0034-4257\(00\)00109-7](http://dx.doi.org/10.1016/S0034-4257(00)00109-7).



- Smirnov, A., Holben, B.N., Slutsker, I., Giles, D.M., McClain, C.R., Eck, T.F., Sakerin, S.M., Macke, A., Croot, P., Zibordi, G., Quinn, P.K., Sciare, J., Kinne, S., Harvey, M., Smyth, T.J., Piketh, S., Zielinski, T., Proshutinsky, A., Goes, J.L., Nelson, N.B., Larouche, P., Radionov, V.F., Goloub, P., Moorthy, K.K., Matarrese, R., Robertson, E.J., Jourdain, F., 2009. Maritime Aerosol Network as a component of Aerosol Robotic Network. *J. Geophys. Res.* 114, D06204. <http://dx.doi.org/10.1029/2008JD011257>.
- Smirnov, A., Holben, B.N., Giles, D.M., Slutsker, I., O'Neill, N.T., Eck, T.F., Macke, A., Croot, P., Courcoux, Y., Sakerin, S.M., Smyth, T.J., Zielinski, T., Zibordi, G., Goes, J.L., Harvey, M.J., Quinn, P.K., Nelson, N.B., Radionov, V.F., Duarte, C.M., Losno, R., Sciare, J., Voss, K.J., Kinne, S., Nalli, N.R., Joseph, E., Krishna Moorthy, K., Covert, D.S., Gulev, S.K., Milinevsky, G., Larouche, P., Belanger, S., Horne, E., Chin, M., Remer, L.A., Kahn, R.A., Reid, J.S., Schulz, M., Heald, C.L., Zhang, J., Lapina, K., Kleidman, R.G., Griesfeller, J., Gaitley, B.J., Tan, Q., Diehl, T.L., 2011. Maritime aerosol network as a component of AERONET – first results and comparison with global aerosol models and satellite retrievals. *Atmos. Meas. Tech.* 4, 583–597. <http://dx.doi.org/10.5194/amt-4-583-2011>.
- Spangenberg, D.A., Chakrapani, V., Doelling, D.R., Minnis, P., Arduini, R.F., 2001. Development of an automated Arctic cloud mask using clear sky satellite observations taken over the SHEBA and ARM NSA sites. Proceedings of the AMS 6th Conference on Polar Meteorology and Oceanography, San Diego, CA, May 14–18, 2001, pp. 246–249.
- Stamnes, K., Li, W., Spurr, R., Eide, H.A., Stamnes, J.J., 2004. Simultaneous retrieval of aerosol and surface properties over bright targets including snow and ice using multi- and hyperspectral data. *Proc. SPIE* 5569, 56–67. <http://dx.doi.org/10.1117/12.565453>.
- Stock, M., Ritter, C., Herber, A., von Hoyningen-Huene, W., Baibakov, K., Gräser, J., Orgis, T., Treffeisen, R., Zinoviev, N., Makshtas, A., Dethloff, K., 2012. Springtime Arctic aerosol: Smoke versus haze, a case study for March 2008. *Atmos. Environ.* 52C, 48–55. <http://dx.doi.org/10.1016/j.atmosenv.2011.06.051>.
- Stohl, A., 2006. Characteristics of atmospheric transport into the Arctic troposphere. *J. Geophys. Res.* 111, D11306. <http://dx.doi.org/10.1029/2005JD006888>.
- Stohl, A., Sodemann, H., 2010. Characteristics of atmospheric transport into the Antarctic troposphere. *J. Geophys. Res.* 115, D02305. <http://dx.doi.org/10.1029/2009JD012536>.
- Stohl, A., Andrews, E., Burkhardt, J.F., Forster, C., Herber, A., Hoch, S.W., Kowal, D., Lunder, C., Mefford, T., Ogren, J.A., Sharma, S., Spichtinger, N., Stebel, K., Stone, R., Ström, J., Tørseth, K., Wehrli, C., Yttri, K.E., 2006. Pan-Arctic enhancements of light absorbing aerosol concentrations due to North American boreal forest fires during summer 2004. *J. Geophys. Res.* 111, D22214. <http://dx.doi.org/10.1029/2006JD007216>.
- Stone, R.S., 2002. Monitoring aerosol optical depth at Barrow, Alaska, and South Pole: historical overview, recent results and future goals. *SIF Conf. Proc.* 80, 123–144.
- Stone, R.S., Key, J.R., Dutton, E.G., 1993. Properties and decay of stratospheric aerosols in the Arctic following the 1991 eruptions of Mount Pinatubo. *Geophys. Res. Lett.* 20 (21), 2359–2362. <http://dx.doi.org/10.1029/93GL02684>.
- Stone, R.S., Anderson, G.P., Andrews, E., Dutton, E.G., Shettle, E.P., Berk, A., 2007. Incursions and radiative impact of Asian dust in northern Alaska. *Geophys. Res. Lett.* 34, L14815. <http://dx.doi.org/10.1029/2007GL029878>.
- Stone, R.S., Anderson, G.P., Shettle, E.P., Andrews, E., Loukachine, K., Dutton, E.G., Schaaf, C., Roman III, M.O., 2008. Radiative impact of boreal smoke in the Arctic: Observed and modeled. *J. Geophys. Res.* 113, D14516. <http://dx.doi.org/10.1029/2007JD009657>.
- Stone, R.S., Herber, A., Vitale, V., Mazzola, M., Lupi, A., Schnell, R.C., Dutton, E.G., Liu, P.S.K., Li, S.-M., Dethloff, K., Lampert, A., Ritter, C., Stock, M., Neuber, R., Maturilli, M., 2010. A three-dimensional characterization of Arctic aerosols from airborne Sun photometer observations: PAM-ARCMIP, April 2009. *J. Geophys. Res.* 115, D13203. <http://dx.doi.org/10.1029/2009JD013605>.
- Stone, R.S., Sharma, S., Herber, A., Eleftheriadis, K., Nelson, D.W., 2014. A characterization of Arctic aerosols on the basis of aerosol optical depth and black carbon measurements. *Elem.: Sci. Anthropocene* 2. <http://dx.doi.org/10.12952/journal.elementa.000027> (22 pp).
- Ström, J., Umegård, J., Tørseth, K., Tunved, P., Hansson, H.-C., Holmén, K., Wismann, V., Herber, A., König-Langlo, G., 2003. One year of particle size distribution and aerosol chemical composition measurements at the Zeppelin station, Svalbard, March 2000–March 2001. *Phys. Chem. Earth* 28, 1181–1190. <http://dx.doi.org/10.1016/j.pce.2003.08.058>.
- Strunin, M.A., Postnov, A.A., Mezrin, M.Y., 1997. Meteorological potential for contamination of Arctic troposphere: Boundary layer structure and turbulent diffusion characteristics. *Atmos. Res.* 44, 37–51. [http://dx.doi.org/10.1016/S0169-8095\(97\)00008-2](http://dx.doi.org/10.1016/S0169-8095(97)00008-2).
- Tang, J., Xue, Y., Yu, T., Guan, Y., 2005. Aerosol optical thickness determination by exploiting the synergy of TERRA and AQUA MODIS. *Remote Sens. Environ.* 94 (3), 327–334. <http://dx.doi.org/10.1016/j.rse.2004.09.013>.
- Tanré, D., Kaufman, Y.J., Herman, M., Mattoo, S., 1997. Remote sensing of aerosol properties over oceans using the MODIS/EOS spectral radiances. *J. Geophys. Res.* 102, 16971–16988. <http://dx.doi.org/10.1029/96JD03437>.
- Teinilä, K., Kerminen, V.-M., Hillamo, R., 2000. A study of size-segregated aerosol chemistry in the Antarctic atmosphere. *J. Geophys. Res.* 105 (D3), 3893–3904. <http://dx.doi.org/10.1029/1999JD01033>.
- Assessment of stratospheric aerosol properties (ASAP). In: Thomason, L.W., Peter, T. (Eds.), SPARC Report N°4 (Stratospheric Aerosol Properties and their Role in Climate), WCRP-124, WMO/TD-No. 1295.
- Thomason, L.W., Herman, B.M., Reagan, J.A., 1983. The effect of atmospheric attenuators with structured vertical distributions on air mass determinations and Langley plot analyses. *J. Atmos. Sci.* 40 (7), 1851–1854. [http://dx.doi.org/10.1175/1520-0469\(1983\)040<1851:TEOAAW>2.0.CO;2](http://dx.doi.org/10.1175/1520-0469(1983)040<1851:TEOAAW>2.0.CO;2).
- Thomason, L.W., Burton, S.P., Luo, B.-P., Peter, T., 2008. SAGE II measurements of stratospheric aerosol properties at non-volcanic levels. *Atmos. Chem. Phys.* 8 (4), 983–995. <http://dx.doi.org/10.5194/acp-8-983-2008>.
- Toledano, C., Cachorro, V.E., Gausa, M., Stebel, K., Aaltonen, V., Berjón, A., Ortiz de Galisteo, J.P., De Frutos, A.M., Bennouna, Y., Blindheim, S., Myhre, C.L., Zibordi, G., Wehrli, C., Kratzer, S., Hakansson, B., Carlund, T., de Leeuw, G., Herber, A., Torres, B., 2012. Overview of sun photometer measurements of aerosol properties in Scandinavia and Svalbard. *Atmos. Environ.* 52C, 18–28. <http://dx.doi.org/10.1016/j.atmosenv.2011.10.022>.
- Tomasi, C., Petkov, B.H., 2014. Calculations of relative optical air masses for various aerosol types and minor gases in Arctic and Antarctic atmospheres. *J. Geophys. Res.: Atmos.* 119 (3), 1363–1385. <http://dx.doi.org/10.1002/2013JD020600>.
- Tomasi, C., Vitale, V., Lupi, A., Di Carmine, C., Campanelli, M., Herber, A., Treffeisen, R., Stone, R.S., Andrews, E., Sharma, S., Radionov, V., von Hoyningen-Huene, W., Stebel, K., Hansen, G.H., Myhre, C.L., Wehrli, C., Aaltonen, V., Lihavainen, H., Virkkula, A., Hillamo, R., Ström, J., Toledano, C., Cachorro, V.E., Ortiz, P., de Frutos, A.M., Blindheim, S., Frioud, M., Gausa, M., Zielinski, T., Petelski, T., Yamanouchi, T., 2007. Aerosols in polar regions: a historical overview based on optical depth and in situ observations. *J. Geophys. Res.* 112, D16205. <http://dx.doi.org/10.1029/2007JD008432>.
- Tomasi, C., Petkov, B.H., Stone, R.S., Benedetti, E., Vitale, V., Lupi, A., Mazzola, M., Lanconelli, C., Herber, A., von Hoyningen-Huene, W., 2010. Characterizing polar atmospheres and their effect on Rayleigh-scattering optical depth. *J. Geophys. Res.* 115, D02205. <http://dx.doi.org/10.1029/2009JD012852>.
- Tomasi, C., Lupi, A., Mazzola, M., Stone, R.S., Dutton, E.G., Herber, A., Radionov, V.F., Holben, B.N., Sorokin, M.G., Sakerin, S.M., Terpugova, S.A., Sobolewski, P.S., Lanconelli, C., Petkov, B.H., Busetto, M., Vitale, V., 2012. An update on polar aerosol optical properties using POLAR-AOD and other measurements performed during the International Polar Year. *Atmos. Environ.* 52C, 29–47. <http://dx.doi.org/10.1016/j.atmosenv.2012.02.055>.
- Tomasi, C., Lanconelli, C., Lupi, A., Mazzola, M., 2013. Dependence of direct aerosol radiative forcing on the optical properties of atmospheric aerosol and underlying surface. Chapter 11 In: Kokhanovsky, A.A., Kokhanovsky, A.A. (Eds.), *Light Scattering Reviews 8*. Springer-Praxis Books in Environmental Sciences, Heidelberg, Germany, pp. 505–626. <http://dx.doi.org/10.1007/978-3-642-32106-1>.
- Tomasi, C., Lanconelli, C., Lupi, A., Mazzola, M., 2014. Diurnally averaged direct aerosol-induced radiative forcing from cloud-free field measurements performed during seven regional experiments. Chapter 8 In: Kokhanovsky, A.A. (Ed.), *Light Scattering Reviews 9*. Springer-Praxis Books in Environmental Sciences, Heidelberg, Germany, pp. 297–425. <http://dx.doi.org/10.1007/978-3-642-37985-7>.
- Treffeisen, R., Tunved, P., Ström, J., Herber, A., Bareiss, J., Helbig, A., Stone, R.S., von Hoyningen-Huene, W., Krejci, R., Stohl, A., Neuber, R., 2007. Arctic smoke – aerosol characteristics during a record smoke event in the European Arctic and its radiative impact. *Atmos. Chem. Phys.* 7, 3035–3053. <http://dx.doi.org/10.5194/acp-7-3035-2007>.
- Trepte, Q., Arduini, R.F., Chen, Y., Sun-Mack, S., Minnis, P., Spangenberg, D.A., Doelling, D.R., 2001. Development of a daytime polar cloud mask using theoretical models of near-infrared bidirectional reflectance for ARM and CERES. Proceedings of the AMS 6th Conference on Polar Meteorology and Oceanography, San Diego, CA, May 14–18, 2001, pp. 242–245.
- Tuncel, G., Aras, N.K., Zoller, W.H., 1989. Temporal variations and sources of elements in the South Pole atmosphere. 1. Non enriched and moderately enriched elements. *J. Geophys. Res.* 94, 13025–13038. <http://dx.doi.org/10.1029/JD094iD10p13025>.
- Vermote, E.F., Tanré, D., Deuze, J.L., Herman, M., Morcrette, J.-J., 1997a. Second simulation of the satellite signal in the solar spectrum (6S): An overview. *IEEE Trans. Geosci. Remote Sens.* 35 (3), 675–686. <http://dx.doi.org/10.1109/36.581987>.
- Vermote, E., Tanré, D., Deuze, J.L., Herman, M., Morcrette, J.J., 1997b. Second Simulation of the Satellite Signal in the Solar Spectrum (6S), 6S User Guide Version 2, July 1997. Université de Lille, France (218 pp).
- Virkkula, A., Teinilä, K., Hillamo, R., Kerminen, V.-M., Saarikoski, S., Aurela, M., Koponen, I.K., Kulmala, M., 2006a. Chemical size distributions of boundary layer aerosol over the Atlantic Ocean and at an Antarctic site. *J. Geophys. Res.* 111, D05306. <http://dx.doi.org/10.1029/2004JD004958>.
- Virkkula, A., Koponen, I.K., Teinilä, K., Hillamo, R., Kerminen, V.-M., Kulmala, M., 2006b. Effective real refractive index of dry aerosols in the Antarctic boundary layer. *Geophys. Res. Lett.* 33, L06805. <http://dx.doi.org/10.1029/2005GL024602>.
- von Hoyningen-Huene, W., Freitag, M., Burrows, J.P., 2003. Retrieval of aerosol optical thickness over land surface from top-of-atmosphere radiance. *J. Geophys. Res.* 108, D9. <http://dx.doi.org/10.1029/2001JD002018>.
- von Hoyningen-Huene, W., Yoon, J., Vountas, M., Istomina, L.G., Rohen, G., Dinter, T., Kokhanovsky, A.A., Burrows, J.P., 2011. Retrieval of spectral aerosol optical thickness over land using ocean color sensors MERIS and SeaWiFS. *Atmos. Meas. Tech.* 4, 151–171. <http://dx.doi.org/10.5194/amt-4-151-2011>.
- Wang, Y., Xue, Y., Li, Y., Guang, J., Mei, L., Xu, H., Ai, J., 2012. Prior knowledge-supported aerosol optical depth retrieval over land surface at 500 m spatial resolution with MODIS data. *Int. J. Remote Sens.* 33 (3), 674–691. <http://dx.doi.org/10.1080/01431161.2011.577832>.
- Warneke, C., Froyd, K.D., Brioude, J., Bahreini, R., Brock, C.A., Cozic, J., de Gouw, J.A., Fahey, D.W., Ferrare, R., Holloway, J.S., Middlebrook, A.M., Miller, L., Montzka, S., Schwarz, J.P., Sodemann, H., Spackman, J.R., Stohl, A., 2010. An important contribution to springtime Arctic aerosol from biomass burning in Russia. *Geophys. Res. Lett.* 37, L01801. <http://dx.doi.org/10.1029/2009GL041816>.
- Warren, S.G., Wiscombe, W.J., 1980. A model for the spectral albedo of snow. II: Snow containing atmospheric aerosols. *J. Atmos. Sci.* 37 (12), 2734–2745. [http://dx.doi.org/10.1175/1520-0469\(1980\)037<2734:AMFTSA>2.0.CO;2](http://dx.doi.org/10.1175/1520-0469(1980)037<2734:AMFTSA>2.0.CO;2).
- Wehrli, C., 2000. Calibrations of filter radiometers for determination of atmospheric optical depths. *Metrologia* 37, 419–422.
- Weitkamp, C., 2005. Lidar: Range-Resolved Optical Remote Sensing of the Atmosphere. Series in Optical Sciences vol. 102. Springer. ISBN: 978-0-387-40075-4 (455 pp.).
- Weller, R., Lampert, A., 2008. Optical properties and sulfate scattering efficiency of boundary layer aerosol at coastal Neumayer Station, Antarctica. *J. Geophys. Res.* 113, D16208. <http://dx.doi.org/10.1029/2008JD009962>.



- Weller, R., Wagenbach, D., 2007. Year-round chemical aerosol records in continental Antarctica obtained by automatic samplings. *Tellus* 59C, 755–765. <http://dx.doi.org/10.1111/j.1600-0889.2007.00293.x>.
- Weller, R., Wöltjen, J., Piel, C., Resenberg, R., Wagenbach, D., König-Langlo, G., Kriews, M., 2008. Seasonal variability of crustal and marine trace elements in the aerosol at Neumayer Station, Antarctica. *Tellus* 60B, 742–752. <http://dx.doi.org/10.1111/j.1600-0889.2008.00372.x>.
- Whitt, D.B., Jacobson, M.Z., Wilerson, J.T., Naiman, A.D., Lele, S.K., 2011. Vertical mixing of commercial aviation emissions from cruise altitude to the surface. *J. Geophys. Res.* 116, D14109. <http://dx.doi.org/10.1029/2010JD015532>.
- Wilson, D.I., Piketh, S.J., Smirnov, A., Holben, B.N., Kuyper, B., 2010. Aerosol optical properties over the South Atlantic and Southern Ocean during the 140th cruise of the M/V S.A. Agulhas. *Atmos. Res.* 98 (2–4), 285–296. <http://dx.doi.org/10.1016/j.atmosres.2010.07.007>.
- Winker, D.M., Vaughan, M.A., Omar, A., Hu, Y., Powell, K.A., 2009. Overview of the CALIPSO mission and CALIOP data processing algorithms. *J. Atmos. Ocean. Technol.* 26 (11), 2310–2323. <http://dx.doi.org/10.1175/2009JTECHA1281.1>.
- Winker, D.M., Pelon, J., Coakley Jr., J.A., Ackerman, S.A., Charlson, R.J., Colarco, P.R., Flamant, P., Fu, Q., Hoff, R.M., Kittaka, C., Kubar, T.L., Le Treut, H., McCormick, M.P., Mégie, G., Poole, L., Powell, K., Trepte, C., Vaughan, M.A., Wielicki, B.A., 2010. The CALIPSO mission: A global 3D view of aerosols and clouds. *Bull. Am. Meteorol. Soc.* 91 (9), 1211–1229. <http://dx.doi.org/10.1175/2010BAMS3009.1>.
- Winker, D.M., Tackett, J.L., Getzewich, B.J., Liu, Z., Vaughan, M.A., Rogers, R.R., 2013. The global 3-D distribution of tropospheric aerosols as characterized by CALIOP. *Atmos. Chem. Phys.* 13 (9), 3345–3361. <http://dx.doi.org/10.5194/acp-13-3345-2013>.
- Wolff, E.W., Cachier, H., 1998. Concentrations and seasonal cycle of black carbon in aerosol at a coastal Antarctic station. *J. Geophys. Res.* 103 (D9), 11033–11041. <http://dx.doi.org/10.1029/97JD01363>.
- Xue, Y., Cracknell, A.P., 1995. Operational bi-angle approach to retrieve the Earth surface albedo from AVHRR data in the visible band. *Int. J. Remote Sens.* 16 (3), 417–429. <http://dx.doi.org/10.1080/01431169508954410>.
- Xue, Y., He, X., Xu, H., Guang, J., Guo, J., Mei, L., 2014. China Collection 2.0: The aerosol optical depth dataset from the synergetic retrieval of aerosol properties algorithm. *Atmos. Environ.* 95, 45–58. <http://dx.doi.org/10.1016/j.atmosenv.2014.06.019>.
- Yamanouchi, T., Treffeisen, R., Herber, A., Shiobara, M., Yamagata, S., Hara, K., Sato, K., Yabuki, M., Tomikawa, Y., Rinke, A., Neuber, R., Schumacher, R., Kriews, M., Ström, J., Schrems, O., Gernandt, H., 2005. Arctic Study of Tropospheric Aerosol and Radiation (ASTAR) 2000: Arctic haze case study. *Tellus B* 57 (2), 141–152. <http://dx.doi.org/10.1111/j.1600-0889.2005.00140.x>.
- Yoon, J., von Hoyningen-Huene, W., Kokhanovsky, A.A., Vountas, M., Burrows, J.P., 2012. Trend analysis of aerosol optical thickness and Ångström exponent derived from the global AERONET spectral observations. *Atmos. Meas. Tech.* 5 (6), 1271–1299. <http://dx.doi.org/10.5194/amt-5-1271-2012>.